Measurement of $\mathcal{CP}$ violation in B_d^0 mixing using $B_d^0 \to D^{*-}\mu^+(\nu_\mu)X$ decays

Anthony Ross

MPhys. Physics with Astrophysics and Cosmology

September 10, 2012

This thesis is submitted in partial fulfilment of the requirements for the degree of Doctor of Philosophy. No part of this thesis has been previously submitted for the award of a higher degree.

Abstract

This thesis describes the measurement of the time-integrated semileptonic charge asymmetry in B_d^0 mixing, a_{sl}^d, using the decay chain of $B_d^0 \to D^{*-}\mu^+(\nu_\mu)$, $D^{*-} \to D^0\pi^-$, $D^0 \to K^+\pi^-$. Decay candidates are reconstructed from 10.4 fb^{-1} of data recorded by the DØ detector at Fermilab's Tevatron $p\overline{p}$ collder during the 2002-2011 'RunII' data taking period. Yields are extracted using a χ^2 minimising simultaneous binned fit where 490k D^* candidates are reconstructed. Factoring in the probability of a candidate B_d^0 mixing using simulated data, the corresponding semileptonic charge asymmetry value was found to be,

$$a_{sl}^d = [1.10 \pm 0.62\ (\text{stat}) \pm 0.08\ (\text{syst})]\%$$

This result is 1.8 standard deviations from zero and the Standard Model predicted value, and 1.4 standard deviations from the 2011 world average. This value is more precise than any single result which is used in the 2011 HFAG world average for a_{sl}^d. If this value were to be included in the world average, then the approximate value would become -0.08 ± 0.37 %.

The measurements presented in this thesis was made possible due to sophisticated online and offline reconstruction software, precise tracking systems, and the first-order background asymmetry negating magnet polarity reversal of the DØ detector.

Acknowledgements

This is far from a complete list of the thanks, there have been countless people who have aided me, leant an ear, or made an impact in my life during my years as a student. Thank you all, especially for being so understanding. Grumpy students can require a lot of patience. Such is the cost of science!

Thanks go to all the staff and fellow students in Lancaster's HEP group, for their guidance and academic support. Additionally, I am grateful to all the members of Fermilab's B-physics group, and to the people of DØ as a whole. To my colleagues and mentors:

I hugely appreciate the assistence rendered to me by Dr. Mark Williams during and after my time spent in at Fermilab. There has not been a single mathematical, physical, computational, or furniture moving problem that this gentleman was unable to assist me with. I am deeply apologetic for causing much more hassle to his working life than he may have been expecting, but I am much obliged that he took the time to get me up to speed on most of the topics involved in my analyses.

Dr. Guennadi Borissov, who wrote many of the software libraries that the DØ B-physics group uses. He is deeply knowledgeable in all matters to do with B physics phenomenology and experimentation, and I hope that the groundbreaking studies he undertakes afford him the world renown he deserves.

Dr. Iain A. Bertram was my supervisor, and as such has had to sift through hundreds of my questions, draft talks, appraisals, and meeting requests over the last four years. I thank him for his advice, for steering me through my difficulties, and for the amusing barrages of creative swearing when any computer misbehaves.

Dr. Rob Henderson taught my first postgraduate course in quantum field theory. His explanations and derivations were thorough and clear, but he deserves further acknowledgement for being both a theory and Linux guru. Similarly, Dr. Alex Finch should be thanked for starting me down the path of software engineering.

Mr. Rob Lewsey and Mrs. Christine Harmer battled on my behalf to manage the long term attachment funds and reimbursement during my time in North America. The process was not straight forward in the least, so these two deserve recognition for their patience and help.

For my friends in and outside of academia: Alex Robson, a steadfast friend since my undergraduate years, has continued his role as entertainer, welcome distraction provider, and coffee drinker during this studentship. An ear for many of my rants and provider of a social life outside of work, he deserves my thanks.

Sa Bom Nim Mark W. Wituk, 5^{th} Dan Tang Soo Do, was my martial arts master and a friend during my time in the United States. He is responsible for me staying in a working physical condition whilst I spent my working life at a computer desk. His guidance saw me competing in the 37^{th} National All Martial Arts Championship, in a ranked grappling tournament, and in my first obstacle race.

Last, but certainly not least, my deepest thanks go to my mentor and friend, 'Grandma' Jean Willacy, who sadly passed away during my studentship. Her tenacity, plain speaking manner, and honesty are greatly missed. She'd have argued against being included in these acknowledgements, but she was one of the biggest influences in my life.

Lancaster University - April 2012

Contents

List of Figures

List of Tables

Chapter 1

Introduction

There are many 'standard models' that have arisen in science and mathematics over the last century; one each for astrophysics, cosmology, cryptography, intended interpretation of syntactical systems, and for set theory. However, 'the Standard Model', capitalised in glory, refers to the mathematical framework that has been constructed to describe our physical Universe down to the smallest scales of matter, energy, and interaction (apart from gravity, they're still working on that one). Although it began coalescing since the 1960s, it is not immutable; hundreds of experimental particle physics analyses are conducted every year to poke, probe, and prod the framework - searching for unpredicted behaviour which hints at 'New Physics', or to narrow down the range of the experimentally found values. Likewise, particle physics did not suddenly manifest itself at the time of The Beatles; moving from the ancient Greek notion on an indivisible portion of matter named the '*atom*', to Antoine Lavoisier's law of the convservation of mass in chemical reactions in 1789, to the discovery of the electron in J. J. Thomson's cathode ray experiments and the discovery of the nucleus in 1909 by Rutherford, the invention of the cloud chamber in 1911, and to the inception of quantum theory in the 1920s - modern particle physics has been two and a half millennia in the making.

Modern experiments often take the form of collider-detector combinations. The collider facilitates the acceleration of subatomic particles to very high energies then makes them smash into each other. The detector then records what happens

by measuring signals produced in electronic systems by the resulting daughter particles leaving the interaction point. This is akin to crashing two cars together at high speed with the aim of finding out how engines work by noting what kind of bits fly out of the carnage... but with a little more finesse.

The analyses contained in this thesis contribute to the study of charge-parity violation manifested in oscillated B_d^0 decays, which is a condidate for an observable source of the asymmetry in production rates of matter and antimatter in our Universe. The principle of this matter-antimatter asymmetry shall be discussed in Chapter 2, along with the bare bones of the Standard Model, the basic physical symmetries encountered in particle physics, and the motivation for the analyses. Chapter 3 details the workings of the Tevatron accelerator chain, the particle collider system that was operated at the Fermi National Accelerator Laboratory, Illinois, USA, and the DØ particle detector. This detector was used to collect the data used in the analyses in this thesis. Chapter 4 describes the analysis and statistical methods used on this data. Finally, Chapter 5 discusses the results of the analyses and their impact on the Standard Model.

Chapter 2

Theoretical Overview

This chapter will outline some inherent physical symmetries (Section 2.1), describe the current 'Standard Model' of particle physics (Section 2.2), and explain how those symmetries can be violated within the Standard Model framework (Sections 2.2.2, 2.3). A short discussion on the need for this symmetry violation is covered in Section 2.5, and the chapter will conclude with the current theoretical and experimental results for $\mathcal{CP}$ violation in the B_d^0 mixing system, and how the DØ detector at Fermilab can compete with them (Sections 2.6, 2.7).

2.1 Symmetry and Transformations

2.1.1 $\mathcal{C}$, $\mathcal{P}$, $\mathcal{T}$ Transformations

Symmetries are very useful in physics, in that a physical symmetry means that a value is conserved within a transformation between the two symmetric states [1]. Conversely, a conserved quantity exposes an underlying physics symmetry. Three important symmetries to particle physics shall be briefly described [2]:

$\mathcal{P}$ - Parity Operation Parity translation is a spatial reflection. When considering the four vector of a particle, $x^\mu = (t, x^1, x^2, x^3)$, and using the convention of the metric $g_{\mu\nu} = \text{diag}(1, -1, -1, -1)$ so that $x_\mu = g_{\mu\nu}x^\nu$, transforming under $\mathcal{P}$ changes the sign of the spatial coordinates only; $x^\mu \xrightarrow{\mathcal{P}} x_\mu$. Angular momentum,

l, remains unchanged ($\mathbf{l} \equiv \mathbf{x} \times p \xrightarrow{\mathcal{P}} \mathbf{l}$), but the behaviour of vectors and scalars differs; polar vectors and pseudoscalars change sign ($\mathbf{V} \xrightarrow{\mathcal{P}}$ -$\mathbf{V}$, P $\xrightarrow{\mathcal{P}}$ -P), axial vectors and proper scalars remain unchanged ($\mathbf{A} \xrightarrow{\mathcal{P}} \mathbf{A}$, S$\xrightarrow{\mathcal{P}}$ S).

$\mathcal{T}$ - Time Reversal Here, the arrow of time is reversed: $t \rightarrow -t$. Four vectors are transformed as $x^{\mu} \xrightarrow{\mathcal{T}} -x_{\mu}$, momenta and angular momenta undergo sign reversal ($p \xrightarrow{\mathcal{T}} -p$, $\mathbf{l} \xrightarrow{\mathcal{T}}$ -$\mathbf{l}$).

$\mathcal{C}$ - Charge Conjugation This changes a particle into its antiparticle. The concept of antiparticles arose historically from predicted negative energy levels in relativistic quantum mechanics. In more modern terms, an antiparticle has the same invariant mass as the particle, but all internal quantum numbers are reversed. The most apparent change under this transformation is that the sign of the particle's electric charge reverses ($q \xrightarrow{\mathcal{C}} -q$).

Invariance It has been experimentally shown that electromagnetic and strong interactions are invariant under any single $\mathcal{C}$, $\mathcal{P}$, or $\mathcal{T}$ transformation [3]. However, weak interactions are not invariant, apart from during a combination of all three, $\mathcal{CPT}$. It is impossible to form a Lorentz-invariant quantum field theory with a Hermitian Hamiltonian that violates $\mathcal{CPT}$ invariance [4]. The $\mathcal{CPT}$ theorem states [5] that this field theory must:

- describe a field that is invariant under $\mathcal{CPT}$ transformation;
- allow the existence of unique vacuum states;
- make fields either commute or anti-commute for spacelike separations.

The spin relationships follow on, giving half-integer spin for fermions and integer spin for bosons.

2.2 Standard Model

A very brief overview of the fundamental model of particle physics, the Standard Model (SM), shall be discussed in this section.

2.2.1 Overview of SM

The SM is a framework, which was finalised in the 1970s with the confirmation of the quark model, aims to describe the fundamental constituents of the Universe and their interactions. However, only the electromagnetic, weak nuclear, and strong nuclear forces are included. Gravitation and dark energy do not form part of the SM, although the source of mass, the Higgs boson, is predicted by it. The fundamental constituents of matter are fermionic (with half-interger spin), and can be divided into leptons (Table 2.1) and quarks (Table 2.2). Bosons are the fundamental force-carrying particles (Table 2.3).

Photons carry the electromagnetic force, so are only involved in interactions between charged particles. Weak interactions are mediated by the flavour changing $W^{\pm}$ and the neutral Z bosons. The strong force is mediated by gluons, which couple to particles that have a 'colour' charge. 'Colour' is a quantum number that comes in three state-antistate pairs; 'red', 'green', 'blue', with their respective 'anti-colours'. Gluons also carry colour charge, making them interact with themselves and other gluons as well as with colour-charged fermions.

The gauge bosons form a symmetry group, $\mathrm{SU(3)_C \otimes SU(2)_L \otimes U(1)_Y}$, where U is a unitary group ($\mathrm{U^{\dagger} = U^{-1}}$), and SU indicates a special unitary group ($\mathrm{det(U)} = 1$). $\mathrm{SU(3)}_C$ describes the strong interaction via gluons, and forms the structure of Quantum Chromodynamics (QCD). $\mathrm{SU(2)_L \otimes U(1)_Y}$ is the electroweak interaction term, which gives a unified description of Quantum Electrodynamics (QED) and weak interactions. The last remaining particle predicted by the SM that has yet to be observed is the Higgs boson, which would exist to accomodate spontaneous symmetry breaking of the electroweak symmetry group where the photon remains massless, but the Z and $W^{\pm}$ acquire mass. Results from ATLAS and CMS in

December of 2011 indicate that the mass of the SM Higgs boson (if it exists) should lie within the range of 115 - 130 GeV/c^2, with all other regions excluded from previous results [6][7].

Name	Symbol	Electric Charge ($\|e\|$)	Mass (MeV/c^2)
Electron	e	-1	0.511
Electron neutrino	ν_e	0	$< 2 \times 10^{-3}$ †
Muon	μ	-1	105.7
Muon neutrino	ν_μ	0	< 0.19 †
Tau	τ	-1	1777
Tau neutrino	ν_τ	0	< 18.2 †

Table 2.1: Basic properties of leptons, arranged in order of generation [8].
† The flavour eigenstates of neutrinos don't have fixed masses. They are mixtures of the mass eigenstates.

Name	Symbol	Electric Charge ($\|e\|$)	Mass (MeV/c^2)
up	u	$+\frac{2}{3}$	1.7 - 3.1
down	d	$-\frac{1}{3}$	4.1 - 5.7
charm	c	$+\frac{2}{3}$	1290^{+50}_{-110}
strange	s	$-\frac{1}{3}$	80 - 130
top	t	$+\frac{2}{3}$	172900 ± 1100
bottom	b	$-\frac{1}{3}$	4190^{+180}_{-60}

Table 2.2: Basic properties of quarks, arranged in order of generation [8]

Force	Gauge Boson	Symbol	Electric Charge ($\|e\|$)	Spin	Mass (GeV/c^2)
Electromagnetic	Photon	γ	$< 10^{-35}$	1	$< 10^{-27}$
Neutral Weak	Z	Z	0	1	91.2
Charged Weak	$W^\pm$	$W^\pm$	± 1	1	80.4
Strong	Gluon	g	0	1	0
Gravity	graviton†	H	0	2	0

Table 2.3: Basic properties of fundamental bosons [8].
† The graviton is a hypothetical boson to mediate the force of gravitation. The Higgs boson gives particles mass when interacting with them, which then allows them to be subject to gravitation.

2.2.2 History

Quark Hypothesis (1964) Gell-Man and Zweig [9] postulated that the known baryons and mesons could be constructed from a series of three subparticles, quarks

(q), and their corresponding antiparticles, antiquarks ($\overline{q}$). The mesons would be bound $q\overline{q}$ states, and baryons would be qqq states. Pseudoscalars, such as pions and kaons, would be described by ^{1}S orbital states and vector mesons, such as ρ or J/Ψ, by ^{3}S orbital states.

Glashow-Illipoulos-Maiani (GIM) Mechanism (1970) From the three known quark flavours of the time, up, down, and strange (see Table. 2.2), it was noticed that semileptonic decay rates showed particular patterns [10]. First, for composite particles with strangeness, it was noticed that $\Delta S = 1$ transitions were suppressed relative to $\Delta S = 0$ by a factor of around 20. It was also noticed that the Fermi constant, G, deduced from nuclear β decays such as $n \rightarrow p + e^- + \overline{\nu}_e$ was smaller than what was deduced from muonic decay $\mu \rightarrow e\nu_e\overline{\nu}_\mu$. This was explained in Cabibbo theory by describing the known down type quarks as a doublet, which predicted the existence of a strangeness-changing neutral current. However, such a process proved to be absent [11],

$$\frac{BR(K^0 \rightarrow \mu^+\mu^-)}{BR(K^+ \rightarrow \mu^+\nu_\mu)} \approx 10^{-8}. \tag{2.1}$$

GIM introduced a fourth quark flavour, charm, which produced a second quark doublet. The requirement for strangeness-changing neutral current was removed with this new theory, the up-type quarks couples to down-type rotated in flavour space by the Cabibbo angle, θ_c:

$$\begin{pmatrix} d' \\ s' \end{pmatrix} = \begin{pmatrix} \cos\theta_c & \sin\theta_c \\ -\sin\theta_c & \cos\theta_c \end{pmatrix} \begin{pmatrix} d \\ s \end{pmatrix} \tag{2.2}$$

Experimental results were consistent with a single angle of $\sin\theta_c \approx 0.22$. In 1974, the discovery of J/Ψ confirmed the existence of this fourth quark flavour. The theory was later expanded by a further generation of two quark flavours to preserve the possibility of $\mathcal{CP}$ violation. That shall be discussed later in this section.

$\mathcal{P}$ & $\mathcal{C}$ Violation $\mathcal{P}$ and $\mathcal{C}$ violation were discovered in the nuclear β decay of ^{60}Co in 1957 [12]. Subsequent nuclear and particle decay analyses showed that a Lorentz-invariant weak transition amplitude, $\mathcal{A}$, should contain both vector and axial vectors to describe beta-decays, and scalar and pseudoscalars to allow for $\mathcal{P}$ and $\mathcal{C}$ violation:

$$\begin{aligned}\mathcal{A} &= G \sum_{i=V,\,A} (\overline{U}\mathrm{V}_C O_i D)[\bar{l}(c_i + c_i'\gamma^5 O_i)\nu] \\ &\sim V\cdot V + V\cdot A + A\cdot V + A\cdot A \end{aligned} \tag{2.3}$$

G is the Fermi coupling constant, $\overline{U} = (\overline{u},\overline{c})$, $D = (d, s)^T$, $\bar{l} = (\overline{e}, \overline{\mu})$, $\nu = (\nu_e, \nu_\mu)^T$, V_C is the Cabibbo rotation matrix seen in Eqn 2.2, $O_V = \gamma^\mu$ and $O_A = i\gamma^\mu\gamma^5$ are vector and axial vector operators respectively, and c_i are coefficients which accommodate the maximal parity violation by neutrinos in $c_i = c_i'$. $V\cdot V$ and $A\cdot A$ are scalars, $V\cdot A$ and $A\cdot V$ are pseudoscalars. $\mathcal{C}$ and $\mathcal{P}$ violation had now been observed and accommodated in theory, but it was still believed that the combination of $\mathcal{CP}$ transformations were still symmetric [13].

$\mathcal{CP}$ Violation It was assumed that the kaon eigenstates, K_S^0 and K_L^0, were pure $\mathcal{CP}$-even and $\mathcal{CP}$-odd eigenstates respectively. In the early 1960s it was demonstrated that a pure K_L beam could show K_S regeneration when interacting with matter [14]. However, it was shown that there seemed to be an excess of K_S regeneration in the forward direction [15]. Cronin, Fitch, Christenson, and Turlay investigated this, but could not find any evidence of anomalous K_S regeneration [16]. As $\mathcal{C}$ and $\mathcal{P}$ violation were found to be possible, they steered the investigation into improving the upper limit on the $\mathcal{CP}$-violating decay channel, $K_L \to \pi\pi$. However, they instead observed this decay, thus discovering $\mathcal{CP}$ violation [16],

$$\frac{\Gamma(K_L \to \pi^+\pi^-)}{\Gamma(K_S \to \pi^+\pi^-)} = [(4.0 \pm 0.6) \times 10^{-6}]. \tag{2.4}$$

The observation can be summarised by describing the quantum mechanical $K_{L/S}$ state as containing an admixture of $\mathcal{CP}$ odd and even components,

$$|K_L\rangle = \frac{1}{\sqrt{1+|\overline{\epsilon}|^2}}(|K_2\rangle + \overline{\epsilon}\,|K_1\rangle) \tag{2.5}$$

$$|K_S\rangle = \frac{1}{\sqrt{1+|\overline{\epsilon}|^2}}(|K_1\rangle + \overline{\epsilon}\,|K_2\rangle) \tag{2.6}$$

$\mathcal{CP}$ violation could be incorporated into weak transition amplitudes by adding a complex phase to the quark mixing matrix. However, it was realised that in a four quark system (2×2 mixing matrix), any complex phase could be rotated away [17]. In 1973, Kobayashi and Maskawa surmised that the mixing matrix should be 3×3 to conserve the complex mixing phases [18]. This required an entire extra generation of quarks, which was a remarkable prediction considering that the c quark from the second generation was still theoretical at the time. The theory successfully described the $\mathcal{CP}$ violation seen in the kaon system, and the required quark flavours were all discovered over the next 22 years, concluding with the discovery of the top quark at Fermilab in 1995 [19].

Modifying the model of weak decays, the weak amplitude, $\mathcal{A}$, became

$$\mathcal{A} = G \sum_{i=V,\,A} (\overline{U}\mathrm{V}_C O_i D)[\bar{l}(1+\gamma^5 O_i)\nu], \tag{2.7}$$

where $\overline{U} = (\overline{u}, \overline{c}, \overline{t})$, $D = (d, s, b)^T$, $\bar{l} = (\overline{e}, \overline{\mu}, \overline{\tau})$, and $\nu = (\nu_e, \nu_\mu, \nu_\tau)^T$. The quark mixing matrix, now the Cabibbo-Kobayashi-Maskawa (CKM) matrix, is described with the following indices,

$$V = \begin{pmatrix} \mathrm{V}_{ud} & \mathrm{V}_{us} & \mathrm{V}_{ub} \\ \mathrm{V}_{cd} & \mathrm{V}_{cs} & \mathrm{V}_{cb} \\ \mathrm{V}_{td} & \mathrm{V}_{ts} & \mathrm{V}_{tb} \end{pmatrix} \tag{2.8}$$

The Particle Data Group (PDG) [8] shows the following a parametrisation of the

CKM matrix,

$$V = \begin{pmatrix} c_{12}c_{13} & s_{12}c_{13} & s_{13}e^{-i\delta_{13}} \\ -s_{12}c_{23} - c_{12}s_{23}s_{13}e^{i\delta_{13}} & c_{12}c_{23} - s_{12}s_{23}s_{13}e^{i\delta_{13}} & s_{23}c_{13} \\ s_{12}c_{23} - c_{12}c_{23}s_{13}e^{i\delta_{13}} & -c_{12}s_{23} - s_{12}c_{23}s_{13}e^{i\delta_{13}} & c_{23}c_{13} \end{pmatrix} \tag{2.9}$$

$c_{ij} = \cos\theta_{ij}$ and $s_{ij} = \sin\theta_{ij}$, where θ are Euler angles which represent a rotation in three-dimensional flavour space, and i and j are family indices. $\mathcal{CP}$ violation is described by a non-zero complex phase, δ_{13}.

2.3 CKM Matrix

For the quark mixing matrix to be unitary, the following conditions must be satisfied:

$$\sum_{i=1}^{3} \mathrm{V}_{ji}\mathrm{V}_{ki}^{*} = \sum_{i=1}^{3} \mathrm{V}_{ij}\mathrm{V}_{ik}^{*} = 0,\ j,k = 1...3, j \neq k; \tag{2.10}$$

$$\sum_{i=1}^{3} |\mathrm{V}_{ij}|^2 = 1,\ j = 1...3, \tag{2.11}$$

where i, j, and k are quark types. From experimental results, a hierarchy was soon noticed. For example, b preferably decays to c over u, and c to s, rather than d. The following relationship could be deduced,

$$|\mathrm{V}_{ub}|^2 \ll |\mathrm{V}_{cb}|^2 \ll |\mathrm{V}_{us}|^2 \ll 1 \tag{2.12}$$

This allows the following to be inferred of the flavour rotation angles from Eqn 2.9,

$$s_{13} \ll s_{23} \ll s_{12} \ll 1 \tag{2.13}$$

In 1983, Wolfenstein expressed the CKM in terms of powers of $\sin\theta_C = \lambda$, taking into account the unitary constraints [20]. Expanding up to the order of λ^4, the

following was produced,

$$\mathrm{V} = \begin{pmatrix} 1-\frac{1}{2}\lambda^2 & \lambda & A\lambda^3(\rho - i\eta + \frac{1}{2}\eta\lambda^2) \\ -\lambda & 1-\frac{1}{2}\lambda^2 - i\eta A^2\lambda^4 & A\lambda^2(1+i\eta\lambda^2) \\ A\lambda^3(1-\rho-i\eta) & -A\lambda^2 & 1 \end{pmatrix} \tag{2.14}$$

Now the three Euler angles and the $\mathcal{CP}$ violating phase can be described by the four real quantities; A, λ, ρ, and η. $|A|$, $|\rho|$, and $|\eta|$ should be of the order of unity for the expansion to be self-consistent. Only the elements corresponding to V_{ts} and V_{ub} display a complex phase in this expansion. The transition between adjacent flavours as described in the 2×2 submatrices within the Wolfenstein parametrisation are thus approximately real. The pattern is also almost diagonal and symmetric, with elements decreasing in magnitude with increasing distance from the diagonal.

The relationship in Eqn 2.10 can be represented as a series of sums of three complex numbers which, when translated to a complex plane, form triangles [21] as they sum to zero:

$$\begin{matrix} \mathrm{V}^*_{ud}\mathrm{V}_{us} + \mathrm{V}^*_{cd}\mathrm{V}_{cs} + \mathrm{V}^*_{td}\mathrm{V}_{ts} = 0 \\ \mathcal{O}(\lambda) \qquad \mathcal{O}(\lambda) \qquad \mathcal{O}(\lambda^5) \end{matrix} \tag{2.15}$$

$$\begin{matrix} \mathrm{V}^*_{ud}\mathrm{V}_{cd} + \mathrm{V}^*_{us}\mathrm{V}_{cs} + \mathrm{V}^*_{ub}\mathrm{V}_{cb} = 0 \\ \mathcal{O}(\lambda) \qquad \mathcal{O}(\lambda) \qquad \mathcal{O}(\lambda^5) \end{matrix} \tag{2.16}$$

$$\begin{matrix} \mathrm{V}^*_{ud}\mathrm{V}_{ub} + \mathrm{V}^*_{cs}\mathrm{V}_{cb} + \mathrm{V}^*_{ts}\mathrm{V}_{tb} = 0 \\ \mathcal{O}(\lambda^4) \qquad \mathcal{O}(\lambda^2) \qquad \mathcal{O}(\lambda^2) \end{matrix} \tag{2.17}$$

$$\mathrm{V}_{td}^{*}\mathrm{V}_{cd} + \mathrm{V}_{ts}^{*}\mathrm{V}_{cs} + \mathrm{V}_{tb}^{*}\mathrm{V}_{cb} = 0 \tag{2.18}$$
$$\mathcal{O}(\lambda^4) \quad \mathcal{O}(\lambda^2) \quad \mathcal{O}(\lambda^2)$$

$$\mathrm{V}_{td}^{*}\mathrm{V}_{ud} + \mathrm{V}_{ts}^{*}\mathrm{V}_{us} + \mathrm{V}_{tb}^{*}\mathrm{V}_{ub} = 0 \tag{2.19}$$
$$\mathcal{O}(\lambda^3) \quad \mathcal{O}(\lambda^3) \quad \mathcal{O}(\lambda^3)$$

$$\mathrm{V}_{ud}^{*}\mathrm{V}_{ub} + \mathrm{V}_{cd}^{*}\mathrm{V}_{cb} + \mathrm{V}_{td}^{*}\mathrm{V}_{tb} = 0 \tag{2.20}$$
$$\mathcal{O}(\lambda^3) \quad \mathcal{O}(\lambda^3) \quad \mathcal{O}(\lambda^3)$$

The magnitude of each section is akin to the length of the side of the triangle on the complex plane, each a 'unitarity triangle'. A graphical representation of the six triangles can be seen in Fig. 2.1. The areas of the triangles are of identical magnitude, and this value is a measure of the amount of $\mathcal{CP}$ violation in the Standard Model.

Eqns 2.15 and 2.16 produce triangles that are very narrow; the ratio of the sides is of the order λ^4. Recent fits place the value of λ at $\lambda = 0.22535 \pm 0.00065$ [22], leading to λ^4 being of order 2^{-3}. The elements $\mathrm{V}_{td}^{*}\mathrm{V}_{ts}$ and $\mathrm{V}_{us}^{*}\mathrm{V}_{cs}$ govern the mixing (see Section 2.4) of K^0 and D^0. The effective weak phases for these are consequently expected to be very small in the SM.

The triangles described in Eqns 2.17 and 2.18 are also 'squashed', though less severely. The contained element, $\mathrm{V}_{ts}^{*}\mathrm{V}_{tb}$, controls B_s^0 mixing.

The last two triangles, described in Eqns 2.19 and 2.20, have large angles as the sides are roughly the same length. This suggests that the manifestation of $\mathcal{CP}$ violation in the interactions governed by these triangles could be more apparent than those governed by the previous examples. The latter triangle corresponds to B decay, and is generally known as 'the Unitarity Triangle'. The $\mathrm{V}_{td}^{*}\mathrm{V}_{tb}$ side controls B_d^0 mixing. By convention, the triangle is scaled by $1/\mathrm{V}_{cd}^{*}\mathrm{V}_{cb}$, making the base of unit length. Various measurements constraint the co-ordinates of the

the Unitarity Triangle apex in the complex plane, ρ, η. This can be seen in Fig. 2.3. The Unitarity Triangle has been subject to many experimental tests, with the current fit as of 2011 presented in Fig. 2.3. The measurements behind the ρ, η constraints can be found via the CKM Fitter group [23]. Although the observables found in the CKM framework represent different dynamical processes across different time-scales, all results point to a single apex. This in turn implies a single complex CKM phase, so the $\mathcal{CP}$ violation observed in particle interactions seems to fit the space left for it in the SM. Though the lengths of the triangle sides in Fig. 2.1 may differ, their areas are equal,

$$\frac{1}{2}J = \frac{1}{2}|\mathrm{Im}\mathrm{V}^*_{mk}\mathrm{V}_{ml}\mathrm{V}_{nk}\mathrm{V}^*_{nl}| = \frac{1}{2}c^2_{13}s_{13}c_{12}s_{12}c_{23}s_{23}\sin\delta_{13}, \tag{2.21}$$

where k, l, m, and n are family indices. When appropriately normalised, the phase invariant Jarlskog J is a measure of the $\mathcal{CP}$ violation effects predicted by the SM [25]. For non-zero $\mathcal{CP}$ violation, the following is required:

$$\theta_{12},\, \theta_{13},\, \theta_{23} \neq 0,\, \frac{\pi}{2} \tag{2.22}$$

$$\delta_{13} \neq 0,\, \frac{\pi}{2} \tag{2.23}$$

$$m_u \neq m_c \neq m_t \neq m_u, \text{ and } m_d \neq m_s \neq m_b \neq m_d \tag{2.24}$$

The last condition comes as a result of the ability to 'rotate away' the $\mathcal{CP}$ violating phase if any two of the up or down-type quarks are degenerate. All three conditions can be combined into one mathematical description,

$$d_{\mathcal{CP}} = 2J(m_t^2 - m_c^2)(m_c^2 - m_u^2)(m_u^2 - m_t^2) \tag{2.25}$$

$$\cdot\,(m_b^2 - m_s^2)(m_s^2 - m_d^2)(m_d^2 - m_b^2) \neq 0 \tag{2.26}$$

By using the hierarchy as described in Eqn 2.13, the value of J in the SM can be approximated to be $J \approx 2 \times 10^{-3}\sin\delta_{13}$ [26]. However, if Eqn 2.21 is considered, the maximal $\mathcal{CP}$ violation allowed in the SM model would be seen if $\theta_{12} \approx \theta_{13} \approx$

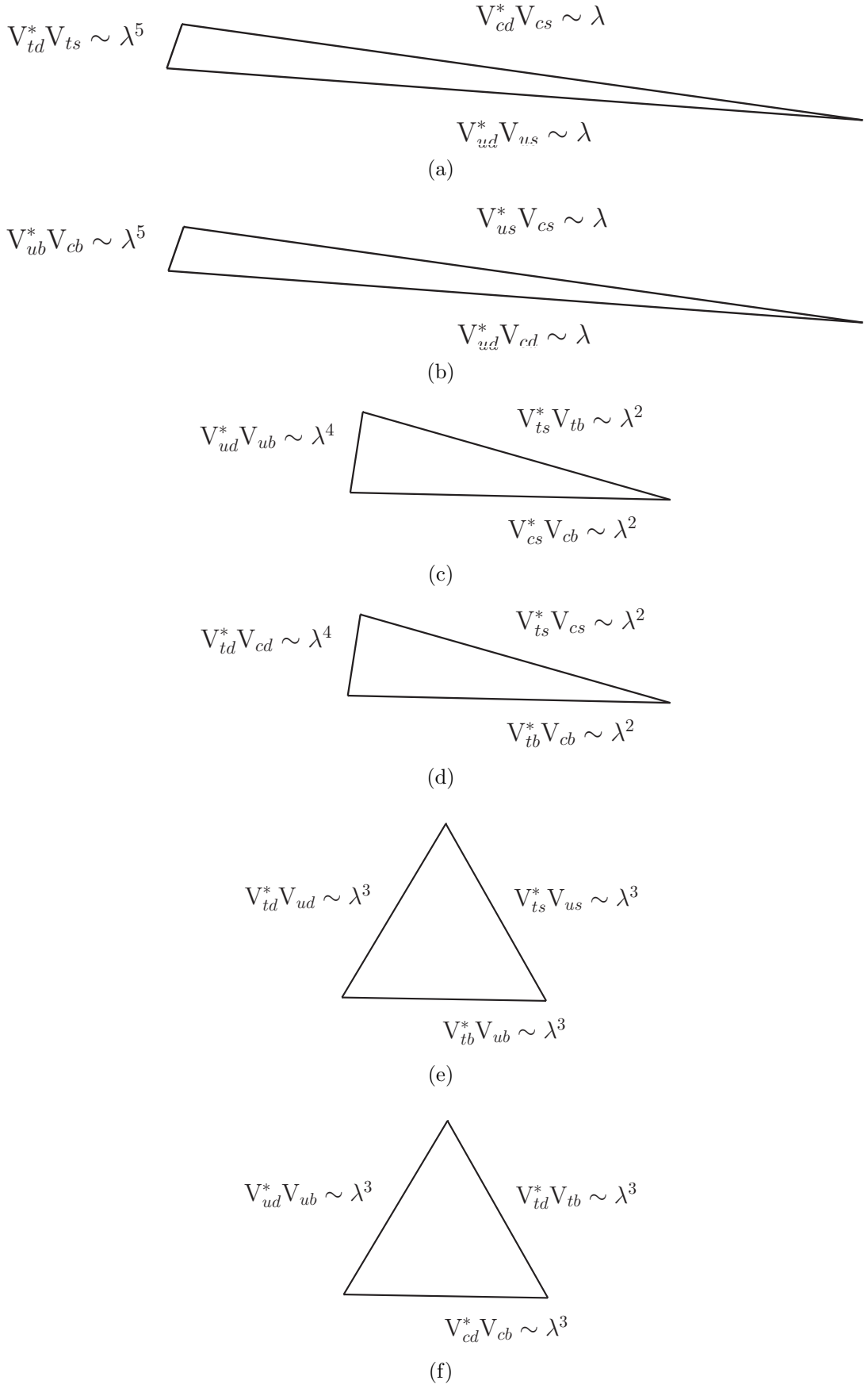

Figure 2.1: The six unitarity triangles which correspond to Eqns 2.15-2.20, respectively.

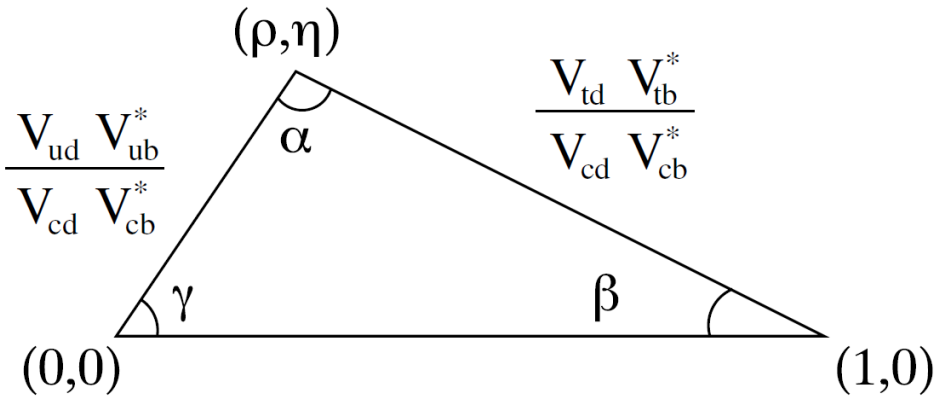

$$\alpha = \arg\left(\frac{V_{td}^* V_{tb}}{-V_{ud}^* V_{ub}}\right) = \arg\left(\frac{V_{ud}^* V_{ub}}{V_{td}^* V_{tb}}\right)$$
$$\beta = \pi - \arg\left(-\frac{V_{td}^* V_{tb}}{-V_{cd}^* V_{cb}}\right) = \arg\left(-\frac{V_{cd}^* V_{cb}}{V_{td}^* V_{tb}}\right)$$
$$\gamma = \arg\left(\frac{V_{ud}^* V_{ub}}{-V_{cd}^* V_{cb}}\right)$$

Figure 2.2: The Unitarity Triangle which is related to decays of $B_{u,d}$ mesons, whose angles are related to the phases of the CKM matrix. The anticlockwise direction is positive [24].

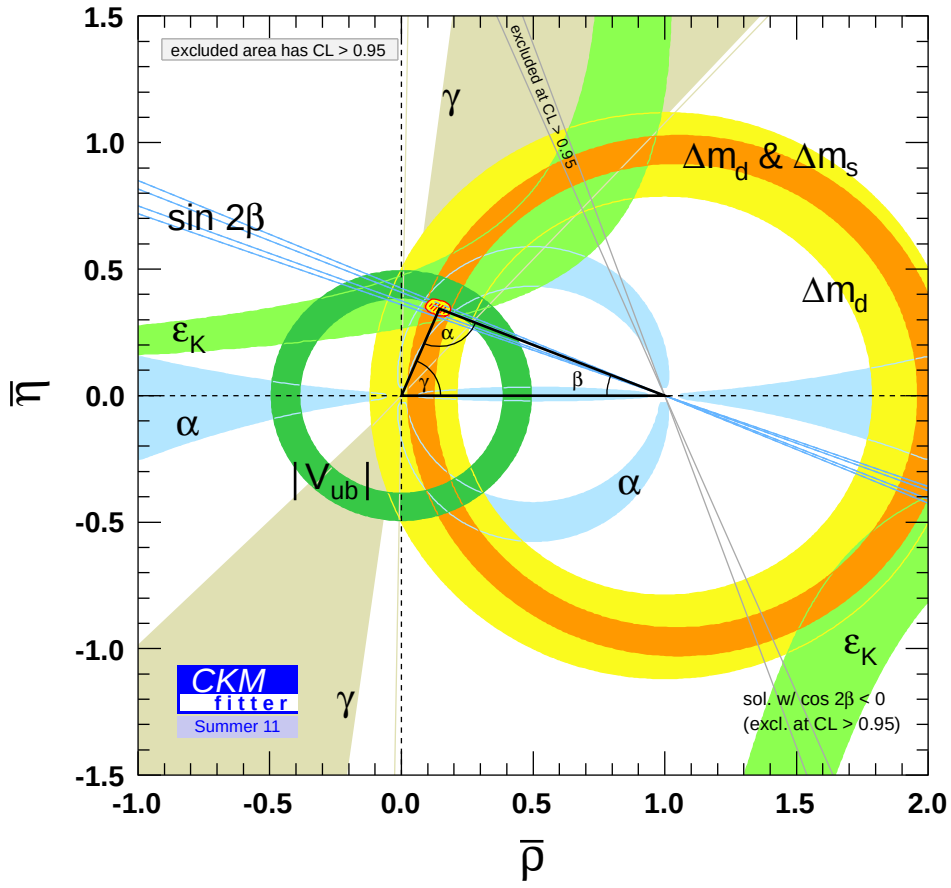

Figure 2.3: The CKMFitter Group's [23] Unitarity Triangle fit as of 2011. The analyses which measure the angles are described and linked on their webpage.

$\theta_{23} \approx \frac{\pi}{4}$ and $\sim \delta_{13} = 1$, giving $J_{\max} \approx 8 \times 10^{-2}$. Thus, maximal $\mathcal{CP}$ violation is not seen in nature; the invariant J is roughly an order of magnitude less than its maximal value.

2.4 CP Violation and Mixing

This section will cover the mixing phenomenon in charge-neutral mesons and the implications for $\mathcal{CP}$ violation. Such topics are discussed in great length across chapters 6, 9-12 of [13] and in [27].

One manifestation of charge asymmetry occurs due to differences in 'mixing' and decay rates between two particles that can 'mix' with each other and have exclusive decay products. Mixing is when a neutral particle becomes its own antiparticle or vice versa. This topic shall be covered in terms of a general neutral meson, P^0, as the basics apply for any neutral meson. The specific cases of K^0, D^0, or B^0 can be found in various literary examples [8] [10]. Mixing is the process of a neutral meson becoming its own anti-particle via two exchanges of W bosons between the constituent quarks, and is characterised by the change of quantum flavour by two units ($\Delta F = 2$). This can come as a two-step transition across an intermediate state, f, ($P^0 \xleftrightarrow{\Delta F=1} f \xleftrightarrow{\Delta F=1} \overline{P}^0$), which can be either on or off-shell. Mixing can also occur in a one-step transition ($P^0 \xleftrightarrow{\Delta F=2} \overline{P}^0$) for the K^0, D^0, and B^0 systems. The latter is shown in the form of Feynman diagrams in Fig. 2.4. The time-dependent $P^0 - \overline{P}^0$ wavefunction, $\Psi(t)$, can be described as an admixture between pure P^0 and $\overline{P}^0$ states with time dependent amplitudes,

$$|\Psi(t)\rangle = a(t)\left|P^0\right\rangle + b(t)\left|\overline{P}^0\right\rangle, \tag{2.27}$$

where $\Psi(t)$ obeys the Schrödinger equation,

$$i\hbar\frac{\partial}{\partial t}\Psi(t) = H\Psi(t), \tag{2.28}$$

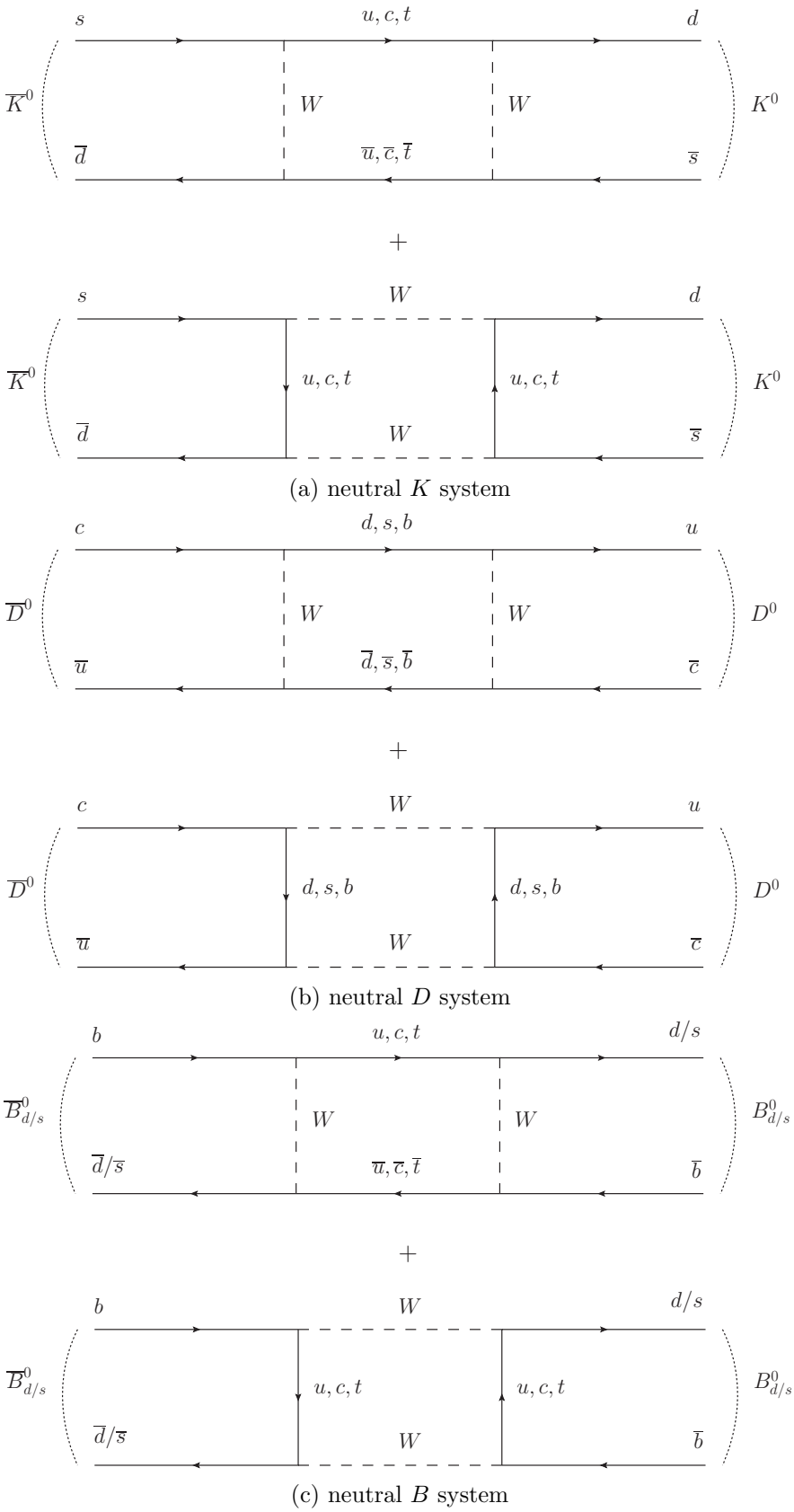

(a) neutral K system

(b) neutral D system

(c) neutral B system

Figure 2.4: The box diagrams describing $\Delta F = 2$ transitions in neutral meson mixing.

where H is the Hamiltonian. In matrix notation, $\Psi(t)$ can be written as,

$$\Psi(t) = \begin{pmatrix} a(t) \\ b(t) \end{pmatrix}. \tag{2.29}$$

This produces a Hamiltonian matrix in terms of the propagation, M, and decay, Γ, of the system,

$$H = M - \frac{i}{2}\Gamma = \begin{pmatrix} M_{11} - \frac{i}{2}\Gamma_{11} & M_{12} - \frac{i}{2}\Gamma_{12} \\ M_{21} - \frac{i}{2}\Gamma_{21} & M_{22} - \frac{i}{2}\Gamma_{22} \end{pmatrix}. \tag{2.30}$$

For $\mathcal{CPT}$ invariance to be obeyed, the following constraints are placed upon this Hamiltonian [28]:

$$\mathcal{CPT} \text{ invariance} \leftrightarrow \begin{matrix} M_{11} = M_{22}, & \Gamma_{11} = \Gamma_{22}, \\ M_{21} = M_{12}^*, & \Gamma_{21} = \Gamma_{12}^* \end{matrix} \tag{2.31}$$

The mixing is described by the off-diagonal components of the Hamiltonian, i.e. for $M_{12} - \frac{i}{2}\Gamma_{12} \neq 0$. From this mixing, the mass eigenstates of a correlated meson-antimeson pair can be described in terms of an admixture of the particle-antiparticle states, normalised by the mixing terms of the Hamiltonian,

$$|P_1\rangle = p\left|P^0\right\rangle + q\left|\overline{P}^0\right\rangle \tag{2.32}$$

$$|P_2\rangle = p\left|P^0\right\rangle - q\left|\overline{P}^0\right\rangle \tag{2.33}$$

where,

$$\left(\frac{q}{p}\right)^2 = \frac{M_{12}^* - \frac{i}{2}\Gamma_{12}^*}{M_{12} - \frac{i}{2}\Gamma_{12}} \tag{2.34}$$

By convention, the positive square root is taken when describing the non-squared p and q values. If there was no $\mathcal{CP}$ violation, P^0 and $\overline{P}^0$ would be given equal preference by nature. This would be described by $q = p$ and an orthogonal pair of

mass eigenstates; $\langle P_1|P_2\rangle = 0$.

As mentioned in Section 2.2.2, the $\mathcal{CP}$ violation as discovered by Cronin and Fitch can be written down by describing the quantum mechanical state of the K_L as an admixture of a small amount of $\mathcal{CP}$-even K_1 amongst the dominant $\mathcal{CP}$-odd K_2. Likewise, K_S would have to be an equal but opposite admixture to conserve $\mathcal{CPT}$ invariance. This is reflected in Eqns. 2.5 and 2.6. In terms of Eqns 2.32, 2.33 and 2.34, $\mathcal{CP}$ violation requires $\langle K_L|K_S\rangle \neq 0$, or $(q/p)_K \neq 1$. This implies that the off-diagonal amplitudes of their mixing Hamiltonian (Eqn 2.30) have a complex phase.

Conventional classification gives us the following terms;

$$\Delta M \equiv M_2 - M_1, \tag{2.35}$$

$$\Delta\Gamma \equiv \Gamma_1 - \Gamma_2, \tag{2.36}$$

$$\Gamma \equiv \frac{1}{2}\left(\Gamma_1 + \Gamma_2\right), \tag{2.37}$$

$$x \equiv \frac{\Delta M}{\Gamma}, \tag{2.38}$$

$$y \equiv \frac{\Delta\Gamma}{2\Gamma}. \tag{2.39}$$

It has been experimentally shown that for the B_d^0 system, $x_d = 0.771 \pm 0.008$ [8] and $y_d < 0.09(95\ \%\text{CL})$ [29], meaning that $\Delta\Gamma_d \ll \Delta M_d$, hence $|\Gamma_{12}^d| \ll |M_{12}^d|$. This inequality is even stronger in the B_s system, where $\Delta\Gamma_s \ll \Gamma_s \ll \Delta M_s$. This means that for both B_d^0 and B_s^0 systems, the eigenvalues and q/p term can be expanded in terms of a small parameter, a,

$$a = \left|\frac{\Gamma_{12}}{M_{12}}\right| \sin\phi, \tag{2.40}$$

Where ϕ is the relative phase between Γ_{12} and M_{12},

$$\frac{M_{12}}{\Gamma_{12}} = -\left|\frac{M_{12}}{\Gamma_{12}}\right| e^{i\phi}. \tag{2.41}$$

If only terms of order $\mathcal{O}(a)$ are kept, Eqns. 2.35, 2.36, and 2.34 are simplified to,

$$\Delta M = 2|M_{12}|,\ \Delta\Gamma = 2|\Gamma_{12}|\cos\phi,\ \frac{q}{p} \approx -e^{-i\phi_M}\left[1 - \frac{a}{2}\right], \tag{2.42}$$

where ϕ_M is the relative phase between q and p. This is known as the mixing phase,

$$\phi_M = \arg\left(\frac{q}{p}\right). \tag{2.43}$$

The SM predicts the following for both B_d^0 and B_s^0 systems ($q = d,\ s$),

$$\phi^q \approx 0,\ \phi_M^q \approx \arg\left(\sqrt{\frac{M_{12}^q}{M_{12}^{q*}}}\right) = \arg(M_{12}^q). \tag{2.44}$$

The only source for a complex phase is the SM is the CKM matrix, which holds only enough degrees of freedom for one complex phase. The SM prediction for M_{12}^q is dominated by the heavy quark in the mixing diagrams in Fig. 2.4c, so the value can be written approximately as

$$M_{12}^q \sim (\mathrm{V}_{tq}\mathrm{V}_{tb}^*)^2. \tag{2.45}$$

Using the Wolfenstein-parametrised CKM matrix (Eqn 2.14) up to the degree of λ^4, the mixing phase for the B_d^0 and B_s^0 systems can be expressed as

$$\phi_M^d = \arg[(\mathrm{V}_{td}\mathrm{V}_{tb}^*)^2] \approx 2\arg(\mathrm{V}_{td}),\ \phi_M^s = \arg(\mathrm{V}_{ts}\mathrm{V}_{tb}^*) \approx 0. \tag{2.46}$$

The state of the neutral meson that started as P^0 or $\overline{P}^0$ can be obtained by extrapolating the time evolution of the mass eigenstates,

$$|P_1(t)\rangle = e^{i(M_1 - \frac{i}{2}\Gamma_1)t}\,|P_1(0)\rangle\,, \tag{2.47}$$

$$|P_2(t)\rangle = e^{i(M_2 - \frac{i}{2}\Gamma_2)t}\,|P_2(0)\rangle\,. \tag{2.48}$$

Rearranging Eqns. 2.32 and 2.33 in these in terms gives,

$$\left|P^0(t)\right\rangle = f_+(t)\left|P^0\right\rangle + \frac{q}{p} f_-(t)\left|\overline{P}^0\right\rangle, \tag{2.49}$$

$$\left|\overline{P}^0(t)\right\rangle = f_+(t)\left|\overline{P}^0\right\rangle + \frac{p}{q} f_-(t)\left|P^0\right\rangle, \tag{2.50}$$

where

$$f_\pm = \frac{1}{2} e^{-iM_1 t} e^{-\frac{1}{2}\Gamma_1 t}[1 \pm e^{i\Delta M t} e^{\frac{1}{2}\Delta\Gamma t}]. \tag{2.51}$$

The decay rate alters with time due to mixing. As a whole, this system is rather complex. There are three simpler, complementary, cases which can be examined. These are outlined in Fig. 2.5.

No oscillation: The final state particles in a reconstructed decay are of the correct charge-correlation, and the mixing parameters can be defined as $\Delta M = \Delta\Gamma = 0$. The time evolutions of P^0 and $\overline{P}^0$ only have an exponential component, which would be identical between particle and anti-particle unless direct $\mathcal{CP}$ violation occurs. If $\mathcal{A}(f)$ is the transition rate of $P^0 \to f$, and $\overline{\mathcal{A}}(\overline{f})$ the rate of the charge conjugate decay, $P^0 \to f$, then direct $\mathcal{CP}$ violation is described as $|\mathcal{A}(f)| \neq |\overline{\mathcal{A}}(\overline{f})|$. This could be observable as a decay rate asymmetry,

$$A_f^{\text{dir}} = \frac{\Gamma(P \to f) - \Gamma(\overline{P} \to \overline{f})}{\Gamma(P \to f) + \Gamma(\overline{P} \to \overline{f})} = \frac{|\mathcal{A}_f|^2 - |\overline{\mathcal{A}}_{\overline{f}}|^2}{|\mathcal{A}_f|^2 + |\overline{\mathcal{A}}_{\overline{f}}|^2}. \tag{2.52}$$

This is illustrated in Fig. 2.5a, and has been observed in $B^0 \to \pi^+\pi^-$ decays [30].

Flavour-specific decays: This covers decay products that come from either P^0 or $\overline{P}^0$, but not from both,

$$P^0 \to f \not\leftarrow \overline{P}^0, \;\; P^0 \not\to \overline{f} \leftarrow \overline{P}^0, \tag{2.53}$$

or alternatively written in terms of transition rates as,

$$|\mathcal{A}_{\overline{f}}| = |\overline{\mathcal{A}}_f| = 0, \;\; |\mathcal{A}_f| = |\overline{\mathcal{A}}_{\overline{f}}| \equiv \mathcal{A}. \tag{2.54}$$

The latter equality states the absence of direct $\mathcal{CP}$ violation in this case. See Fig. 2.5b for an illustration of the process. Semileptonic decays are often chosen so that the lepton charge can be used to tag the neutral meson-antimeson state at the time of decay, i.e. $f = l^+X$, $\overline{f} = l^-X$. Also, a weak decay will be clean from any QCD effects in the first level decay products which might demonstrate direct $\mathcal{CP}$ violation. Thus, let $\mathcal{A}_{SL}$ be defined as $\mathcal{A}_{SL} \equiv |\mathcal{A}(l^+X)| = |\overline{\mathcal{A}}(l^-X)|$ It can be shown [31] that the flavour-specific semileptonic decay rates evolve as

$$\Gamma(P^0(t) \to l^+X) \propto e^{-\Gamma_1 t} C_+(t) |\mathcal{A}_{SL}|^2, \tag{2.55}$$

$$\Gamma(P^0(t) \to l^-X) \propto e^{-\Gamma_1 t} C_-(t) \left|\frac{q}{p}\right|^2 |\mathcal{A}_{SL}|^2, \tag{2.56}$$

$$\Gamma(\overline{P}^0(t) \to l^-X) \propto e^{-\Gamma_1 t} C_+(t) |\mathcal{A}_{SL}|^2, \tag{2.57}$$

$$\Gamma(P^0(t) \to l^+X) \propto e^{-\Gamma_1 t} C_-(t) \left|\frac{p}{q}\right|^2 |\mathcal{A}_{SL}|^2, \tag{2.58}$$

where $C_\pm = 1 + e^{\Delta\Gamma t} \pm 2e^{\frac{1}{2}\Delta\Gamma t} \cos \Delta M t$. From Eqns 2.55 - 2.58, it can be seen that $\mathcal{CP}$ violation due to $|q/p| \neq 1$ arises if there is a decay rate asymmetry between the mixed chains $P^0 \to \overline{P}^0 \to l^-X$ and $\overline{P}^0 \to P^0 \to l^+X$. This is seen as a wrong-sign semileptonic asymmetry, a_{sl},

$$\begin{aligned} a_{sl} &= \frac{\Gamma(P^0(t) \to l^-X) - \Gamma(\overline{P}^0(t) \to l^+X)}{\Gamma(P^0(t) \to l^-X) + \Gamma(\overline{P}^0(t) \to l^+X)} = \frac{|p/q|^2 - |q/p|^2}{|p/q|^2 + |q/p|^2} \\ &= \frac{1 - |q/p|^4}{1 + |q/p|^4}. \end{aligned} \tag{2.59}$$

Although the probability of having come from a mixed meson changes with meson lifetime, the value a_{sl} is actually time-independent. Using Eqns. 2.40 and 2.42, a_{sl}

can be written as

$$a_{sl} = a + \mathcal{O}(a^2) = \left|\frac{\Gamma_{12}}{M_{12}}\right| \sin\phi = \frac{\Delta\Gamma}{\Delta M}\tan\phi. \tag{2.60}$$

If $\Delta\Gamma$ and ΔM can be constrained by other measurements, such as lifetime studies, then the wrong-sign semileptonic asymmetry allows access to the phase, ϕ.

Flavour-nonspecific decays: If both P^0 and $\overline{P}^0$ can decay to state f ($P^0 \to f \leftarrow \overline{P}^0$), the mixing phase ϕ_M becomes observable from the interference between the direct decay to f and the mixing of P^0 before decay. This is illustrated in Fig. 2.5c. Using Eqn 2.42, the difference in decay widths in the B_q system can be derived as [32]

$$\begin{aligned}\Gamma(B_q(t) \to f) &= \mathcal{N}_f |A_f|^2 \frac{1+|\lambda_f|^2}{2} e^{-\Gamma t} \\ &\cdot \left[\cosh\frac{\Delta\Gamma t}{2} + \mathcal{A}^{\rm dir}_{{\rm CP}_f}\cos(\Delta M t) + \mathcal{A}_{\Delta\Gamma_f}\sinh\frac{\Delta\Gamma t}{2} + \mathcal{A}^{\rm mix}_{{\rm CP}_f}\sin(\Delta M t)\right],\end{aligned} \tag{2.61}$$

$$\begin{aligned}\Gamma(\overline{B_q}(t) \to f) &= \mathcal{N}_f |A_f|^2 \frac{1+|\lambda_f|^2}{2} (1+a) e^{-\Gamma t} \\ &\cdot \left[\cosh\frac{\Delta\Gamma t}{2} - \mathcal{A}^{\rm dir}_{{\rm CP}_f}\cos(\Delta M t) + \mathcal{A}_{\Delta\Gamma_f}\sinh\frac{\Delta\Gamma t}{2} - \mathcal{A}^{\rm mix}_{{\rm CP}_f}\sin(\Delta M t)\right],\end{aligned} \tag{2.62}$$

where

$$\lambda_f \equiv \frac{q}{p}\frac{\overline{A}_f}{A_f}, \tag{2.63}$$

$$\mathcal{A}^{\rm dir}_{{\rm CP}_f} \equiv \frac{1-|\lambda_f|^2}{1+|\lambda_f|^2} = \frac{|A_f|^2 - |\overline{A}_f|^2}{|A_f|^2 + |\overline{A}_f|^2}, \tag{2.64}$$

$$\mathcal{A}_{\Delta\Gamma_f} \equiv -\frac{\mathrm{Re}\,\lambda_f}{1+|\lambda_f|^2}, \tag{2.65}$$

$$\mathcal{A}^{\rm mix}_{{\rm CP}_f} \equiv \frac{2\,\mathrm{Im}\,\lambda_f}{1+|\lambda_f|^2}, \tag{2.66}$$

and $q = d, s$. $\mathcal{N}_f$ is the time-independent normalisation factor. $\mathcal{A}_{\Delta\Gamma_f}$ only contributes if $\Delta\Gamma$ is large, which it is not in the B system. Thus, the time-dependent

asymmetry can be written as the difference in decay widths over the sum,

$$a_f(t) = \frac{\Gamma(\overline{B}_q(t) \to f) - \Gamma(B_q(t) \to f)}{\Gamma(\overline{B}_q(t) \to f) + \Gamma(B_q(t) \to f)} \tag{2.67}$$

$$\sim \mathcal{A}^{\text{mix}}_{\text{CP}_f} \sin \Delta M t - \mathcal{A}^{\text{dir}}_{\text{CP}_f} \cos \Delta M t. \tag{2.68}$$

This time dependent asymmetry can be a probe into several $\mathcal{CP}$ violating cases. Assuming that $\phi = 0$, direct $\mathcal{CP}$ violation ($|A_f| \neq |\overline{A}_f|$) is manifested as $\mathcal{A}^{\text{dir}}_{\text{CP}_f} \neq 0$. Likewise, $\mathcal{CP}$ violation due to interference where $\phi_M = \arg(q/p) \neq 0$ is seen as $\mathcal{A}^{\text{mix}}_{\text{CP}_f} \neq 0$. Hence, $\mathcal{CP}$ violation in interference allows a measure of both direct asymmetry and asymmetry due to the mixing phase angle if the lifetime dependence of the asymmetry from Eqn 2.67 is fitted.

This concludes the overview on the three types of $\mathcal{CP}$ violation. It should be noted that if a time-integrated study is being conducted, the decay rate Γ can be replaced by a yield count N. This means that if the flavour of the neutral meson can be identified at decay, the direct $\mathcal{CP}$ violation induced asymmetry (Eqn 2.52) becomes

$$A^{\text{dir}}_f = \frac{N(\overline{P}^0 \to f) - N(P \to \overline{f})}{N(\overline{P}^0 \to f) + N(P \to \overline{f})}, \tag{2.69}$$

and the asymmetry due to mixing becomes

$$\begin{aligned} a_{sl} &= \frac{N(P^0 \to \overline{P}^0 \to l^+X) - N(\overline{P}^0 \to P^0 \to l^-X)}{N(P^0 \to \overline{P}^0 \to l^+X) + N(\overline{P}^0 \to P^0 \to l^-X)} \\ &= \frac{1}{f_{\text{osc}}} \frac{N(l^+) - N(l^-)}{N(l^+) + N(l^-)}, \end{aligned} \tag{2.70}$$

where the sign of the lepton tags the flavour of the neutral meson at decay and f_{osc} is the fraction of the sample which has truly shown oscillation. Candidates which have not oscillated reduce the measured asymmetry if included in the sample, so dividing by this fraction accounts for the dilution. Thus, $\mathcal{CP}$ violation searches can become simple counting experiments.

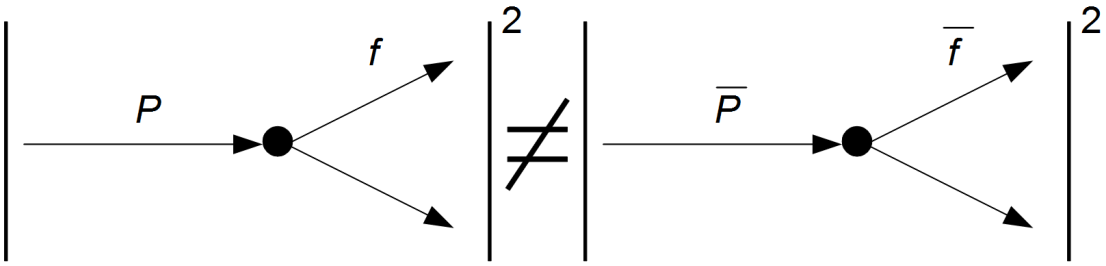

(a) No oscillation - **direct** CP violation

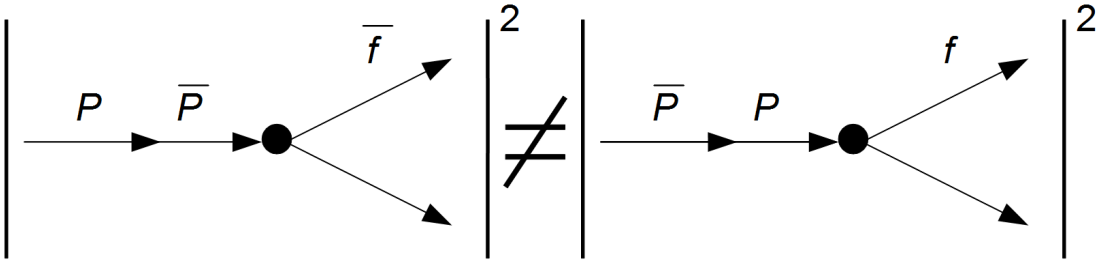

(b) Oscillation - CP violation in **mixing**

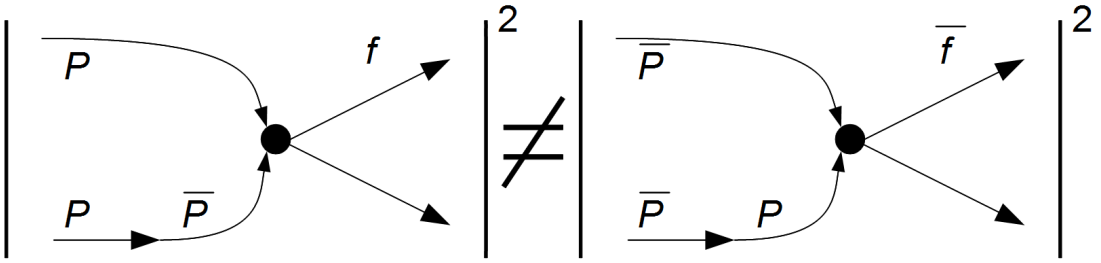

(c) Flavour unspecific - CP violation from **interference** between decay and mixing

Figure 2.5: The three cases where flavour-specific $\mathcal{CP}$ violation manifests; direct, in mixing, and in interference.

2.5 Why Search for $\mathcal{CP}$ Violation?

Although the CKM matrix has been greatly successful, predicting three generations of quarks and introducing a degree of freedom to allow for $\mathcal{CP}$ violation, the story is not finished. There are some discrepancies between cosmological predictions and observations with respect to matter-antimatter asymmetry, ongoing searches for physics beyond the SM, and evidence for charge asymmetries that are inconsistent with SM predictions.

2.5.1 Cosmological Grounds

As matter and antimatter annihilate at low energies, and as the early Universe was in a state of near-homogeneous matter-antimatter plasma, there must have been an imbalance between the two for the Universe to have evolved allowing large scale objects to form. In nature, the only antimatter that is seen comes from cosmic rays (e.g. $\overline{p}$), which have a flux relative to protons of $\overline{p}/p \sim 10^{-4}$ [33]. This is consistent with the absence of ambient antiprotons, so natural antimatter seems only to occur via high energy collisions between matter. In cosmological terms, the imbalance between matter and antimatter can be expressed in the ratio of baryons to photons, η,

$$\eta \equiv \frac{n_B - n_{\overline{B}}}{n_\gamma} = (6.14 \pm 0.25) \times 10^{-10}, \tag{2.71}$$

where $n_{B/\overline{B}/\gamma}$ is the number density of baryons/antibaryons/photons, all of which can be deduced from the Cosmic Microwave Background (CMB) radiation, giving the result above [34].

In 1967, Sakharov defined three conditions for baryosynthesis, the process of baryon production in the early Universe that allows for such an asymmetry [35](original paper at [36]):

$\Delta B \neq 0$ reactions: These are baryon number violating transitions, which is required for an overall positive baryon number excess in the Universe but is not sufficient in itself. This is because for every baryon number changing transition ($N \to f$), there would exist a $\mathcal{CP}$ conjugate process that would reverse the change with equal likelihood ($\overline{N} \to \overline{f}$), unless two other conditions are fulfilled;

$\mathcal{C}$ & $\mathcal{CP}$ violation: A difference in rate of the two transitions above ($\Gamma(N \to f) \neq \Gamma(\overline{N} \to \overline{f})$) would constitute an overall drift of the overall baryon number in one direction. However, this will not be sufficient for baryon-antibaryon asymmetry, as a state of thermal-equilibrium negates arrow-of-time. This means that the $\mathcal{T}$ conjugate transitions of $f \to N$ and $\overline{f} \to \overline{N}$ reverse any baryon number change. This is an issue of $\mathcal{CPT}$ invariance; it is impossible to produce $\mathcal{CP}$ violation with $\mathcal{CPT}$ invariance unless $\mathcal{T}$ can be individually violated. This is realised in the last required condition;

Non-equilibrium conditions: The system must not be in thermal equilibrium, giving a defined direction for the arrow-of-time. In essence, the required physical result comes from the ability for reactions to freeze out.

This branch of Big Bang cosmology and the SM seem to offer the correct environment for this asymmetry to occur; Baryon number violation is believed to have taken place through non-perturbative weak interaction processes in the hot plasma of the early Universe [38]. However, the asymmetry provided by the CKM phase would be proportional to $d_{\mathcal{CP}}$, seen in Eqn 2.25. To conserve dimensionality (or lack thereof), $d_{\mathcal{CP}}$ should be divided by a factor with dimension (mass)^{12}. The natural candidate for this factor would be the temperature of the electroweak phase transition, $T_{EW} \sim 100$ GeV. This is the energy reqiured for baryon number violation due to a chiral anomaly, and also for thermal equilibrium to be absent during the phase transition between unbroken electroweak symmetry at high energy and broken electroweak symmetry at low energy [37]. This would make the

asymmetry provided by the CKM matrix at most

$$\eta \lesssim \frac{d_{\mathcal{CP}}}{T_{EW}^{12}} \sim 10^{-20}, \tag{2.72}$$

or if maximal $\mathcal{CP}$ violation was realised in the SM, an order of magnitude more. This prediction is roughly ten orders of magnitude lower than the required asymmetry seen in Eqn 2.71. This means that the SM with a single $\mathcal{CP}$ violating phase in the CKM matrix would be unable to produce the Universe that is observed today. New sources of $\mathcal{CP}$ violation need to be found to address this shortcoming. For example, many theories beyond the SM predict extra $\mathcal{CP}$ violating phases beyond the standard model.

2.5.2 Probing Physics Beyond SM

Despite being largely successful, the SM still has some methodological issues. The lack of 'naturalness' in the hierarchy of coupling constants is an issue; as the gauge couplings converge at high energies, it does not seem like they will all converge at the same energy to form a grand-unified gauge coupling [39]. A family of new physics theories, Supersymmetry (SUSY) [40], seek to address these issues by introducing a partner to each fundamental particle with a half-spin difference, called a 'sparticle', introducing a symmetry between bosons and fermions. This would double the pool of available particles, introduce new couplings and virtual transitions, and generally introduce degrees of freedom to overcome the methodological issues with the SM.

Additional complex couplings are described in these theories which are suppressed in the Standard Model, which would give extra opportunities for $\mathcal{CP}$ violation to be manifested. As such, anomalous $\mathcal{CP}$ violation beyond the standard model becomes a measurable probe for these new theories. However, with increasing testing of the SM, various flavours of SUSY are becoming less likely to come to fruition. For example, recent results from the detectors at the Large Hadron Col-

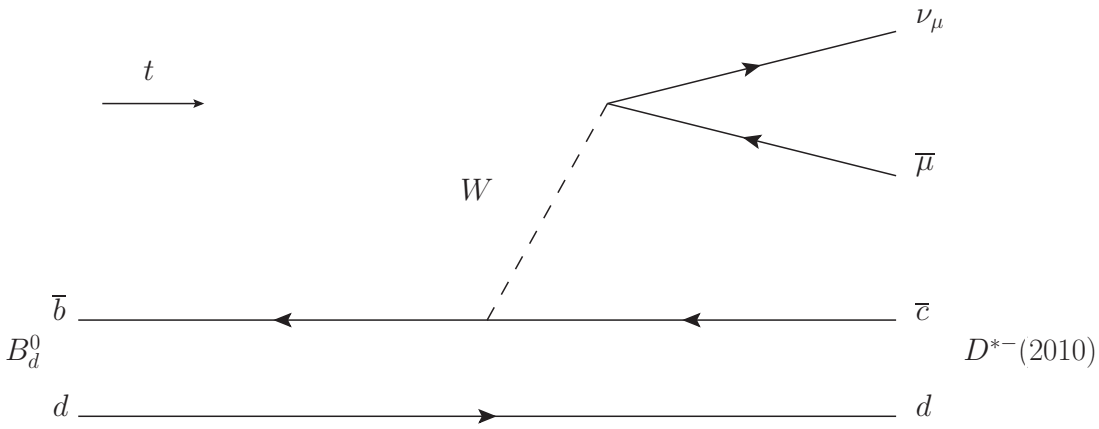

Figure 2.6: Tree level decay of $B_d^0 \to D^{*-}\mu^+\nu$. This is a weak process; there is no QCD contribution that may induce direct $\mathcal{CP}$ violation in this B decay.

lider considerably constrain the parameter space for the Minimal Supersymmetric Standard Model (MSSM) [41].

2.6 $\mathcal{CP}$ Violation from Mixing in $B_d^0 \to D^{*-}\mu^+\nu_\mu$ Decays

As discussed in the **Flavour-specific decays** portion of Section 2.4, semileptonic neutral B decays can be a probe of the semileptonic flavour specific charge asymmetry, a_{sl}^d

$$\begin{aligned} a_{sl}^d &= A_{\mathcal{CP}}(B_d^0 \to D^{*-}\mu^+\nu_\mu) \equiv A_{D^{*-}\mu^+}^{\text{mix}} \\ &= \frac{\Gamma(\overline{B}_d^0 \to B_d^0 \to D^{*-}\mu^+) - \Gamma(B_d^0 \to \overline{B}_d^0 \to D^{*+}\mu^-)}{\Gamma(\overline{B}_d^0 \to B_d^0 \to D^{*-}\mu^+) + \Gamma(B_d^0 \to \overline{B}_d^0 \to D^{*+}\mu^-)} \\ &= \frac{N(\overline{B}_d^0 \to B_d^0 \to D^{*-}\mu^+) - N(B_d^0 \to \overline{B}_d^0 \to D^{*+}\mu^-)}{N(\overline{B}_d^0 \to B_d^0 \to D^{*-}\mu^+) + N(B_d^0 \to \overline{B}_d^0 \to D^{*+}\mu^-)} = \frac{\Delta\Gamma_d}{\Delta M_d}\tan\phi, \end{aligned} \quad (2.73)$$

where $N(X)$ is the yield of events with decay type X. By performing this counting experiment and by using the decay width and mass differences between the B_d^0 eigenstates from other analyses, access is gained to the complex phase, ϕ_d. A tree level Feynman diagram of the $B_d^0 \to D^{*-}\mu^+\nu$ decay can be seen in Fig. 2.6.

2.6.1 Theoretical Value

In the SM, the $\mathcal{CP}$ asymmetry in the flavour-specific B_d system is [42],

$$a_{fs}^d = \mathrm{Im}\,\frac{\Gamma_{12}}{M_{12}} = \left[a\,\mathrm{Im}\,\frac{\lambda_u}{\lambda_t} + b\,\mathrm{Im}\,\frac{\lambda_u^2}{\lambda_t^2}\right] \times 10^{-4}, \tag{2.74}$$

where a and b are numerical parameters determined from analysing the contributions to Γ_{12} up to next to leading order (NLO) perturbations in bq interactions [44].

$$a = 2 \times 10^4 \frac{\Gamma_{12}^{uc} - \Gamma_{12}^{cc}}{M_{12}^d/\lambda_t^{d2}}, \;\; b = 10^4 \times \frac{2\Gamma_{12}^{uc} - \Gamma_{12}^{cc} - \Gamma_{12}^{uu}}{M_{12}^d/\lambda_t^{d2}} \tag{2.75}$$

and λ_u/λ_t can be given in terms of the Wolfenstein parameters from Eqn 2.14,

$$\frac{\lambda_u}{\lambda_t} = \frac{1-\overline{\rho}-i\overline{\eta}}{(1-\overline{\rho})^2+\overline{\eta}^2} - 1 = \frac{\cos\beta - i\sin\beta}{R_t} - 1, \tag{2.76}$$

$$\mathrm{Im}\,\frac{\lambda_u}{\lambda_t} = -\frac{sin\beta}{R_t},\; \mathrm{Im}\left(\frac{\lambda_u}{\lambda_t}\right)^2 = \frac{2\sin\beta}{R_t} - \frac{\sin 2\beta}{R_t^2} \tag{2.77}$$

where

$$R_t \equiv \sqrt{(1-\overline{\rho})^2+\overline{\eta}^2},\; \beta = \arg\left(\frac{-\lambda_t}{\lambda_c}\right). \tag{2.78}$$

As of 2007, the prediction for charge asymmetry calculated in this fashion is [44]

$$a_{sl}^d = \left(-0.048^{+0.010}_{-0.012}\right)\,\%, \;\; \text{with} \;\; \frac{\Delta\Gamma_d}{\Delta M_d} = \left(52.6^{+11.5}_{-12.8}\right) \times 10^{-4}. \tag{2.79}$$

This implies a $\mathcal{CP}$ violating phase of

$$\phi_d = \arg\left(-\frac{M_{12}^d}{\Gamma_{12}^d}\right) = -0.091^{+0.026}_{-0.038} = (-5.2^{+1.5}_{-2.1})^\circ. \tag{2.80}$$

The predicted asymmetry is very small. This is due to a_{sl}^d being doubly suppressed [42]; first by $|\Gamma_{12}/M_{12}| = \mathcal{O}(m_b^2/M_W^2)$ suppressing a_{sl}^d to the percent level, and also by the GIM suppression factor m_c^2/m_b^2, reducing it by a further order of magnitude. Any large deviation from this could be evidence of physics beyond the

standard model.

2.6.2 Previous Measurements

The Heavy Flavor Averaging Group (HFAG) produces a world average of a_{sl}^d based on the results of various analyses across multiple particle physics experiments. The current results as of 2011 are reproduced in Table 2.4. The current world average, $a_{sl}^d(\text{W.A}) = (-0.58 \pm 0.34)$ %, has a central value of roughly an order of magnitude greater than the SM prediction, but the uncertainties are too large to make a discernable non-zero conclusion. This value includes contributions from analyses where the contributions to total B semileptonic charge asymmetry, A_{sl}^b, from a_{sl}^d and a_{sl}^s could not be separated. This was handled by either assuming $a_{sl}^s = 0$ or by using the highly correlated results. The B factory only average, which is not subject to this issue, is $a_{sl}^d(\text{W.A. B Factory}) = (-0.47 \pm 0.46)$ %, which is also consistent with zero. The value for asymmetry in $B_d^0/\overline{B}_d^0$ mixing as listed in the PDG [8] is a BABAR analysis using inclusive dilepton events [45]. An asymmetry of $a_{sl}^d = [0.5 \pm 1.2\ (\text{stat}) \pm 1.4\ (\text{syst})]$ % was reported; again consistent with zero.

A DØ study into like-sign dimuon events in the $B_{d/s}$ system has found evidence for anomalous asymmetry [46]. This is a measurement of charge asymmetry in B mixing, with contributions from both a_{sl}^d and a_{sl}^s,

$$A_{sl}^b = C_d a_{sl}^d + C_s a_{sl}^s, \tag{2.81}$$

where $C_{d/s}$ is the fractional contribution from $B_{d/s}$ system. By varying the impact parameter range of the sample, the $C_{d/s}$ values change, meaning that a_{sl}^d and a_{sl}^s can also be extracted. The analysis assumes that the entirety of the charge asymmetry is from B mixing. See Fig. 2.8 for an illustration. This yielded a value of $a_{sl}^d = (-0.12 \pm 0.52)$ %. This analysis also suggests the anomalous charge asymmetry may originate in the B_s system, so the average a_{sl}^d value from the B factory experiments, $a_{sl}^d(\text{W.A. B Factory}) = -0.47 \pm 0.46$ %, is used in this thesis.

Experiment	Method	Measured, a^d_{sl}, (%)
CLEO [47]	partial hadronic reco.	+1.7 ± 7.0 (stat) ± 1.4 (syst)
CLEO [48]	dileptons	+1.3 ± 5.0 (stat) ± 0.5 (syst)
CLEO [48]	average of above	+1.4 ± 4.1 (stat) ± 0.6 (syst)
BaBar [49]	$\|q/p\|_d$ from hadronic	-5.71 ± 2.52 (stat) ± 2.13 (syst)
BaBar [50]	$\|q/p\|_d$ from dileptons	0.16 ± 0.52 (stat) ± 0.37 (syst)
BaBar [51]	partial rec. $D^* l\nu$	-1.30 ± 0.68 (stat) ± 0.40 (syst)
Belle [52]	dileptons	-0.11 ± 0.79 (stat) ± 0.85 (syst)
	Average of above	-0.47 ± 0.46 (tot.)
OPAL [53]	leptons	+0.8 ± 2.8 (stat) ± 1.2 (syst)
OPAL [54]	inclusive (no tags)	+0.5 ± 5.5 (stat) ± 1.3 (syst)
ALEPH [55]	leptons	-3.7 ± 3.2 (stat) ± 0.7 (syst)
ALEPH [55]	inclusive (no tags)	+1.6 ± 3.4 (stat) ± 0.9 (syst)
ALEPH [55]	average of above two	-1.3 ± 2.6 (tot.)
DØ[56]	dimuons	-0.92 ± 0.44 (stat) ± 0.32 (syst)
CDF [57]	dimuons	+1.36 ± 1.51 (stat) ± 1.15 (syst)
	Average of all	-0.58 ± 0.34 (tot.)

Table 2.4: The measurements of $\mathcal{CP}$ violation in B^0 mixing for various experiments and the world average value. Details on the measurements can be found in references in the HFAG paper [43]. The bottom seven measurements could not separate contributions from B^0_d and B^0_s, and so either assume $\mathcal{CP}$ violation from mixing B^0_s to be zero or give correlated a^q_{sl} results. These measurements can be seen in Fig. 2.7.

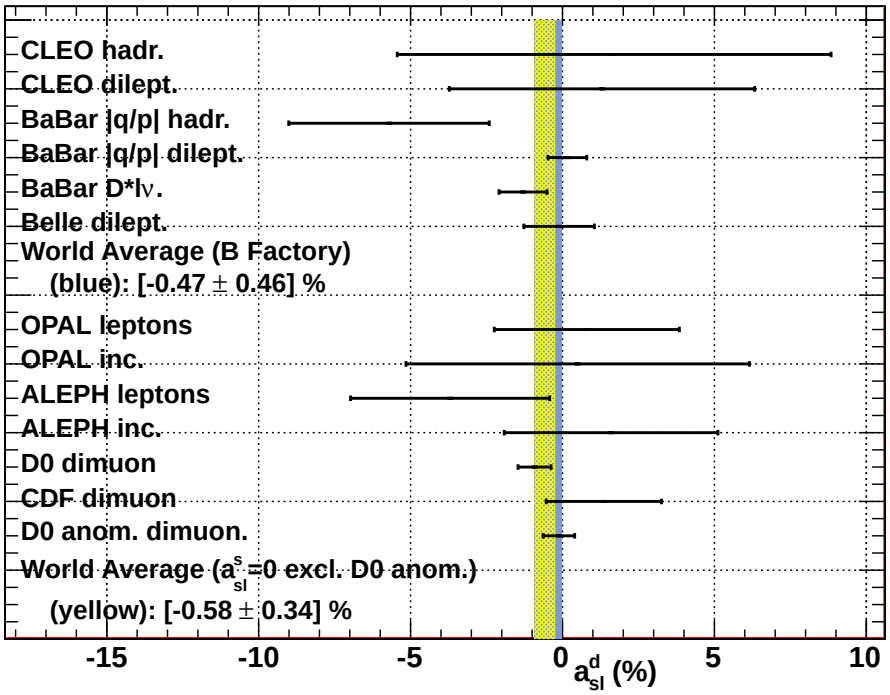

Figure 2.7: A graphical representation of the information in Table 2.4. Included is the anomalous dimuon asymmetry measurement. The solid blue bar is the B factory world average. The yellow mesh is the world average taking into account the hadron collider A_{sl}^b results.

This value does not use the a^q_{sl} correlated hadron collider results as seen in the bottom half of Table 2.4.

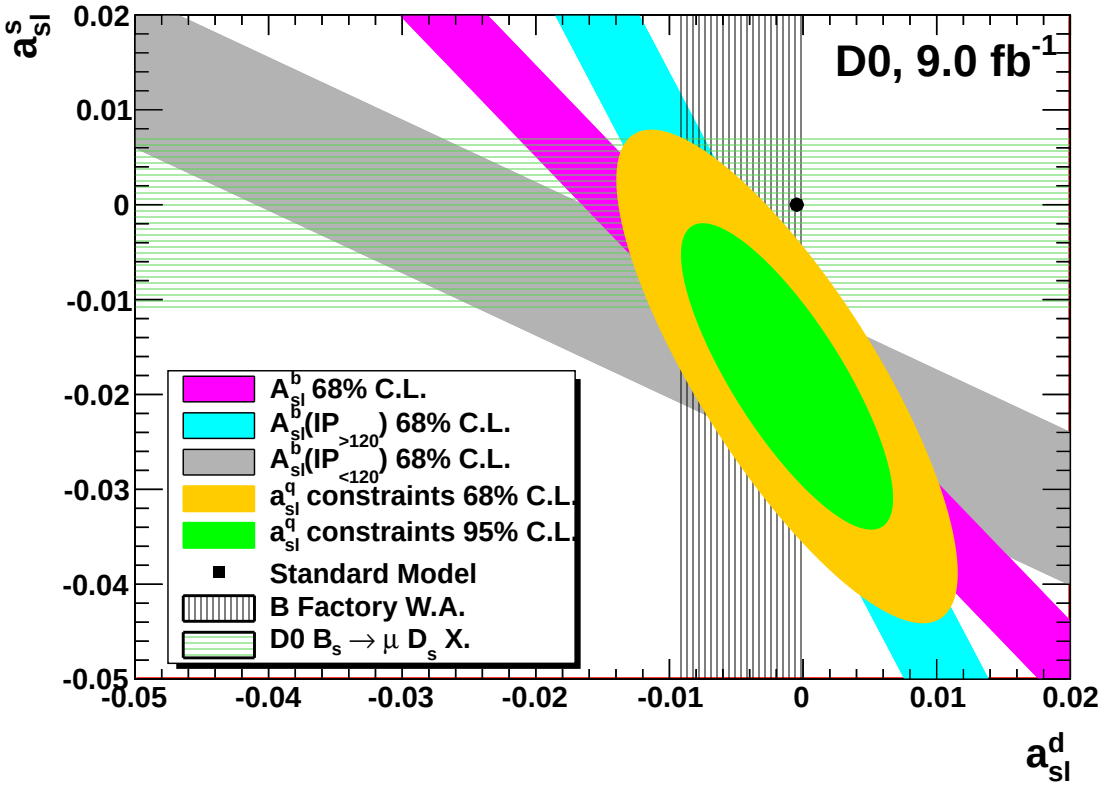

Figure 2.8: The asymmetry plots from the DØ like-sign dimuon asymmetry study [46] shown with the previous DØ a^s_{sl} result (horizontal line) and the B factory world average of a^d_{sl} (vertical line). The magenta line shows the central A^b_{sl} asymmetry result. The blue and grey lines represent impact parameter regions of the A^b_{sl} study, and the ovals show the combination of these two measurements to 68 % and 95 % confidence levels. From this combination, values for a^s_{sl} and a^d_{sl} can be extracted.

2.7 Perspectives for Tevatron

As seen in Eqn 2.73, the search for $\mathcal{CP}$ violation from B^0 mixing can be performed by finding the charge asymmetry, a^d_{sl}, which in turn can become a counting experiment. The Tevatron accelerator and DØ detector (see chapter 3) compliment each other for this measurement.

Firstly, hadronic collisions result in a much higher production rate of $b\bar{b}$ pairs

compared to electron-positron collisions. This is of the order of

$$\sigma_{b\bar{b}}(\text{hadronic})/\sigma_{b\bar{b}}(e^+e^-) = (\alpha_S/\alpha_{EM})^2 \sim 100. \tag{2.82}$$

This results in a faster accumulation of $B\overline{B}$ events.

The Tevatron collided $p\overline{p}$ bunches, which has an advantage over pp colliders as pp interactions result in a surplus of u valence quarks in the initial interaction and hadronisation. This introduces a production asymmetry in $B/\overline{B}$ meson flavours. $p\overline{p}$ colliders are not affected by this issue.

The DØ detector magnet systems had their polarities regularly reversed during data-taking, exposing each section of the detector to the same flux of particles and antiparticles. This feature allows the negation of various first-order systematic effects which arise from differing reconstruction efficiencies for particles and antiparticles. This will be discussed in Section 4.2.

Another advantage of hadronic colliders is the ability to fully account for specific track reconstruction efficiency asymmetries using dedicated channels. For example, the negative kaons have a lower reconstruction efficiency compared to positive kaons due to additional interaction possibilities with the detector material. This will be discussed in Chapter 4. B factories typically dealt with these systematic biases in different ways, either through estimating the ratio of track reconstruction efficiencies or by assigning a systematic uncertainty per track. Hadron colliders, however, produce a larger number of c quarks which hadronise into D^0 mesons, which in turn can decay semileptonically. This can provide clean channels for extracting various track asymmetries, as long as $\mathcal{CP}$ violation in D^0 mixing is strongly suppressed. This was assumed because semileptonic D^0 decays are purely tree level, governed by a single weak phase. This means that no direct $\mathcal{CP}$ violation is expected. By requiring a veto on wrong-sign daughter particles, mixed D^0 candidates should also be excluded from the samples.

There were two further arguments for the suppression of $\mathcal{CP}$ violation in mixing in the charm sector when the analyses started, but recent results have discounted

them. First, The box diagram for D^0 mixing, as seen in Fig. 2.4b, is suppressed by the small CKM matrix elements factor $V^*_{ub}V_{cb} = \mathcal{O}(\lambda^4)$. Light quarks dominate this box diagram, so the mixing was thought to be suppressed. This was supported by a 2010 BaBar measurement which found $x_D = \Delta M_D/\Gamma_D = [1.6 \pm 2.3$ (stat) $\pm$ 1.2 (syst) $\pm$ 0.8 (model)$]\times 10^{-3}$ [58]. However, this has since been superceeded, and the updated world average value gives $x_D = 0.63^{+0.19}_{-0.20}$ % if charm $\mathcal{CP}$ violation is non-zero ($x_D = 0.65^{+0.18}_{-0.19}$ % if it is zero) [43]. This means that it has been experimentally shown that mixing is allowed in the charm sector. Second, $\mathcal{CP}$ violation in D^0 mixing was theoretically expected to be suppressed even in the case of physics beyond the Standard Model [59]. This was due to $\Delta\Gamma_D$ being calculated to remain at the SM level despite enhancements to ΓM_D, so $\Delta\Gamma_D/\Delta M_D \ll 1$. However, it has been experimentally shown that this is not the case, with y_D being of similar magnitude to x_D [43]. As such, $\mathcal{CP}$ violation in the D^0 system will be an interesting avenue of research in the near future.

Assuming the absense of direct $\mathcal{CP}$ violation in D^0 sources, the kaon asymmetry within the DØ detector can be measured using a sample of approximately 3.45M $D^* \to D^0(\mu K\nu_\mu)\pi$ decays. No $\mathcal{CP}$ violation was expected from D^0 production or decay, so the entirety of the extracted asymmetry should be due to positive/negative kaon reconstruction efficiency differences, contaminated with any muon/pion reconstruction asymmetries. However, if it was to be found that D^0 decays manifest $\mathcal{CP}$ violating properties, then this search could be turned to extracting that value instead by utilising an alternative method of kaon asymmetry extraction. The muon and track asymmetries are being investigated independently, and so can be subtracted from the measured kaon reconstruction asymmetry and from a^d_{sl} as required. The statistical uncertainty on the kaon asymmetry measurement would be of the order $1/\sqrt{3.45\text{ M}} \sim 0.05$ %, which is much lower than the expected uncertainty of the measured a^d_{sl}. Thus, the statistical uncertainty of a^d_{sl} should not be significantly increased by background asymmetries.

The measurement of a^d_{sl} in this document is based on roughly half a million

$B_d^0 \to D^{*-}\mu^+X$ decays. If the sample was entirely pure and entirely from oscillated B_d^0 mesons then the expected statistical uncertainty would be of the order of 0.15 %. However, the dilution of the useful events is not known until the conclusion of the analysis. Despite this, it still seemed likely that a single measurement could be performed to rival the current world average.

Chapter 3

Experimental Setup

First, a note about tense. At the time of writing, the Tevatron particle accelerator and DØ detector are physically intact, but are no longer in use. As such, when referring to the physical setup of the experiment, the present tense is used. When referring to the act of colliding particles and collecting data, the past tense is used. The Fermi National Accelerator Laboratory (Fermilab), in Batavia, IL, USA, is the site of the Tevatron accelerator, which collided $p\bar{p}$ bunches from 1992 to 2011. It is the site of two multi-purpose detectors; the DØ detector, named after its location on the main ring, and the 'Collider Detector at Fermilab' (CDF). There were two discrete data taking periods; RunI which took place between 1992 and 1995, and RunII which began in 2002 and concluded with the end of Tevatron operations in September 2011. During RunI, the centre of mass energy achieved was 1.8 TeV, recording 115 pb^{-1} of integrated luminosity [60]. The absense of a magnetic field in the inner tracking systems in this era meant that accurate particle momentum measurements could not be performed, limitating the prospect of performing b-physics at DØ. Between RunI and RunII, major upgrades were performed to both the Tevatron and the DØ detector, the latter allowing tracking fine enough to allow competitive b-physics measurements. A higher centre of mass energy of 1.96 TeV with increased instantaneous luminosities, peaking at 4.31×10^{32} $\text{cm}^{-2}\text{sec}^{-1}$ [61], resulted in a much larger recorded dataset for RunII of 10.4 fb^{-1} of recorded integrated luminosity. For future reference, it should be noted that RunII was

itself split into sub-eras, with relatively small downtimes between each. These are outlined in Table 3.1.

Era	Time Period
RunIIa	April 2002 - March 2006
RunIIb1	- Summer 2007
RunIIb2	- Summer 2009
RunIIb3	- Summer 2010
RunIIb4	- September 2011

Table 3.1: Outline of RunII eras.

3.1 The Accelerator Chain

Fig. 3.1 shows a simplified view of the Tevatron accelerator complex. The chain starts with a Cockroft-Walton chamber [62]. Hydrogen atoms were ionised to produce H^- ions and accelerated to an energy of around 750 keV. They were then fed into Linac, a linear accelerator, where the energy of the beam was increased to 400 MeV. The electrons were stripped from the ions by passing the beam through carbon foil, leaving a beam of protons. These then entered a synchrotron accelerator, the 'Booster', and were accelerated to 8 GeV before entering the Main Injector.

The Main Injector is a three kilometer circumference synchrotron which performed three major functions; to accept 8 GeV protons from the Booster and 8 GeV antiprotons from the antiproton Accumulator, to accelerate the protons to 120 GeV and deliver them to the antiproton production target, and to accelerate antiprotons to 150 GeV before injecting them into the Tevatron. With respect to the first two points, antiprotons were produced by sending the 120 GeV protons to a nickel target. Negatively charged particles with energies of approximately 8 GeV were extracted and sent to a debuncher, which reduced the spread of their momenta. From there, antiprotons were transferred to the Accumulator, where the antiproton beam emittance was reduced via stochastic cooling [63]. After cooling, the 8 GeV antiprotons were sent to the Main Injector, where they were

pre-accelerated to 150 GeV before being injected into the Tevatron.

The final acceleration to both proton and anti-proton beams occurred in the Tevatron, where the energy of each was raised to 980 GeV. Once this energy was reached, the beams were focused to collide at two points on the ring; one at DØ and the other at CDF. The beams were bunched, with crossings occurring every 396 ns. The beams would continue to collide at these two points for a number of hours. Eventually, the interaction of particles with the residual gas in the beampipe vacuum and the long range interactions of bunches would increase the emittances of the beams and reduce the instantaneous luminosities. Consequently, the beams would be dumped. The lifetime of two interacting beams before being dumped is called a 'store'. Typically a new store would start within a few hours after the end of the last one. The parameters of the beams are shown in Table 3.2.

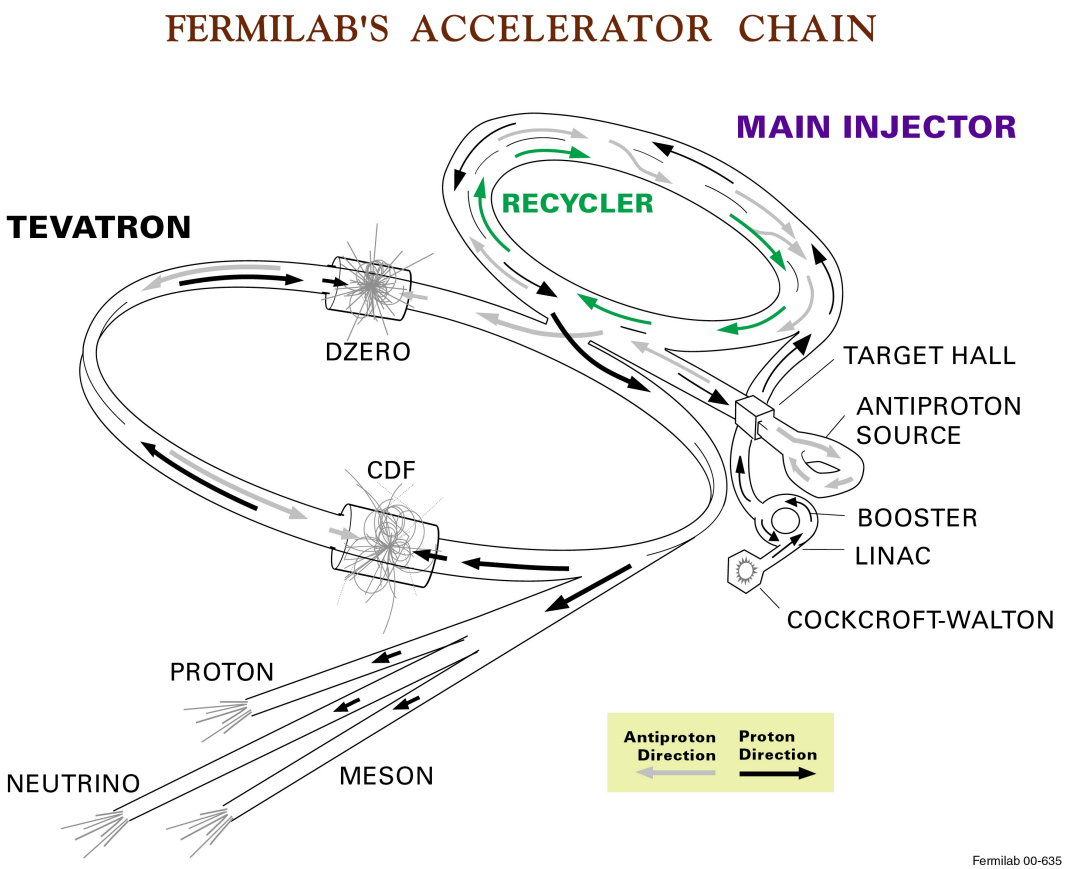

Figure 3.1: Fermilab's accelerator complex [65].

Parameter	RunI (1993-1995)	RunII (2002 - 2011)
Energy per beam (GeV)	900	980
Proton bunches	6	36
Antiproton bunches	6	36
Protons per bunch	2.3×10^{11}	2.7×10^{11}
Antiprotons per bunch	5.5×10^{10}	7.0×10^{10}
Proton emittance RMS(μm)		$\tilde{2}.8$ [66]
Antiproton emittance RMS(μm)		1.4 [66]
β^* (cm^{-1})		38.7 *pm* 1.6 [67]
Bunch length (m)	0.60	0.37
Bunch spacing (ns)	$\sim$ 3500	396
Interactions/crossing	2.5	2.3
Peak instantaneous luminosity (cm^{-2}s^{-1})	2.5×10^{-31}	4.31×10^{-32}
Peak delivered integrated luminosity (pb^{-1}/week)	5	73.47 [68]

Table 3.2: Tevatron parameters.

3.1.1 Tevatron Performance

Fig. 3.2 shows the peak luminosity for each store during Run II. The design luminosity was only reached towards the end of RunIIa, but further measures to overcome the limitations of the antiproton beam [64] meant that the performance could be increased year on year until the shutdown of the Tevatron. At that time, 11.9 fb^{-1} of integrated luminosity had been delivered, of which 10.7 fb^{-1} had been recorded by DØ. This is reduced to 10.4 fb^{-1} after removing any runs listed as 'bad' due to hardware faults. This gave an average efficiency of 87%, though in the last few eras the weekly efficiently was mostly over 90%. Fig. 3.3 shows the Tevatron delivered and DØ recorded integrated luminosity over RunII. The analyses in this thesis are based upon the 10.4 fb^{-1} of recorded luminosity in the RunII dataset.

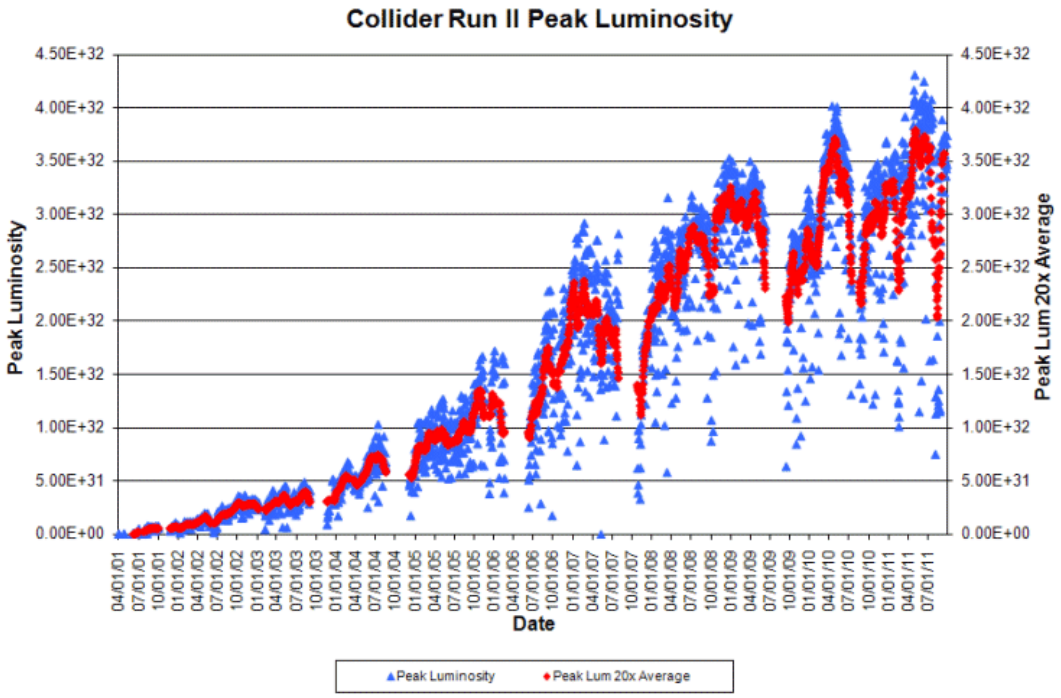

Figure 3.2: Peak instantaneous luminosities during RunII.

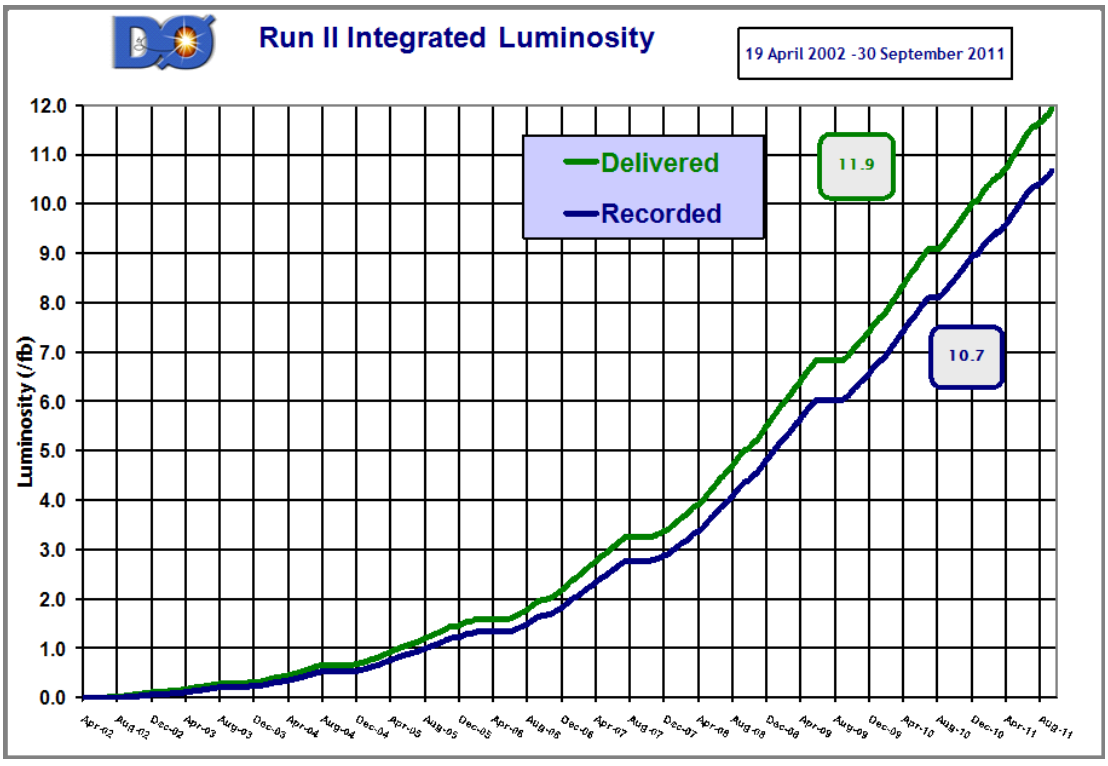

Figure 3.3: Integrated luminosity delivered by the Tevatron and integrated luminosity recorded by DØ.

3.2 The DØ Detector

A related and important property of the DØ detector is that both the solenoid and toroid magnets could have their polarities independently reversed. The polarity combination was changed roughly every two weeks, allowing the same regions of the detector to be exposed to a roughly equal flux of particles of both charges. This allows for the cancellation of many charge-dependent systematic effects that would pollute a charge asymmetry measurement. This shall be covered in Section 4.2.

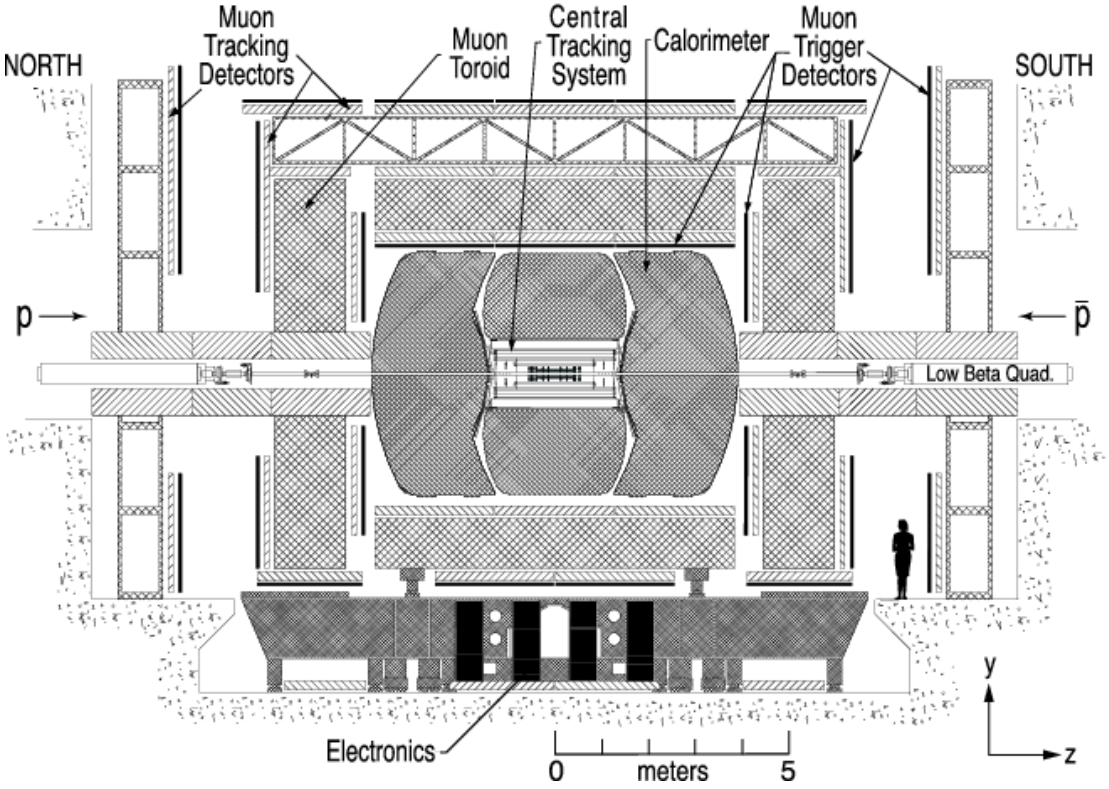

Figure 3.4: General view of the DØ detector [69].

3.2.1 DØ Co-ordinate System

A right handed Cartesian co-ordinate system is used to describe positions within the DØ detector. The origin is located at the centre, where the interaction point would be, the z-axis oriented along the beam axis and pointing in the direction of the proton beam, and the y-axis pointing vertically upward. Thus, the x-axis points radially away from the centre of the Tevatron ring. Polar co-ordinates are

also used where r points perpendicularly to the beam direction. The azimuthal angle is defined as $\phi = \arctan(y/z)$ and polar angle by $\theta = \arctan(r/z)$. As such, ϕ describes the transverse (xy) plane of the detector with $\phi = 0$ describing the positive direction of the x-axis. A value called 'pseudorapidity (η)', which is the ultra-relativistic limit of rapidity (y), is also useful. η can be used as a replacement for θ in describing the angle of particle flight with respect to the beam direction.

$$y \equiv \frac{1}{2} \ln \frac{E + p_z}{E - p_z} \tag{3.1}$$

$$\eta = -\ln \tan \frac{\theta}{2} \tag{3.2}$$

The choice of (r,η,ϕ) co-ordinates is appropriate as it reflects the symmetries of the experiment. Physical processes are invariant under rotation around the unpolarised beam and η is Lorentz-invariant under boosts along the z-axis. By convention, the term 'forward' refers to large η values.

3.2.2 Silicon Microstrip Tracker (SMT)

Precise tracking close to the interaction points is essential for b-physics studies. It follows that such a tracking detector would have to be resillient to the high-radiation environment. To date, SMT detectors are best suited to this task.

The following description is illustrated in Fig. 3.5. A single-sided microstrip detector consists of finely spaced strips of strongly doped p-type silicon (p) implanted on a lightly doped n-type silicon (n) substrate. A thin layer of strongly doped n-type is deposited on the opposite side of the detector (n^-). A positive voltage is applied to n^-, which depletes the n volume of free electrons and creates an electric field. When a charge particle passes through the substrate, the ionization that occurs leaves a trail of electron-hole pairs. Due to the electric field, the holes drift to the p strips, producing a localised signal. The signal is reported by a small cluster of strips, so the particle postion is extrapolated by weighting the strip positions by the amount of collected charge in that strip. Double sided

detectors can be made by forming the n^- side into read-out strips too. Tilting n^- strips relative to the p strips makes a 3D stereo measurement possible. The

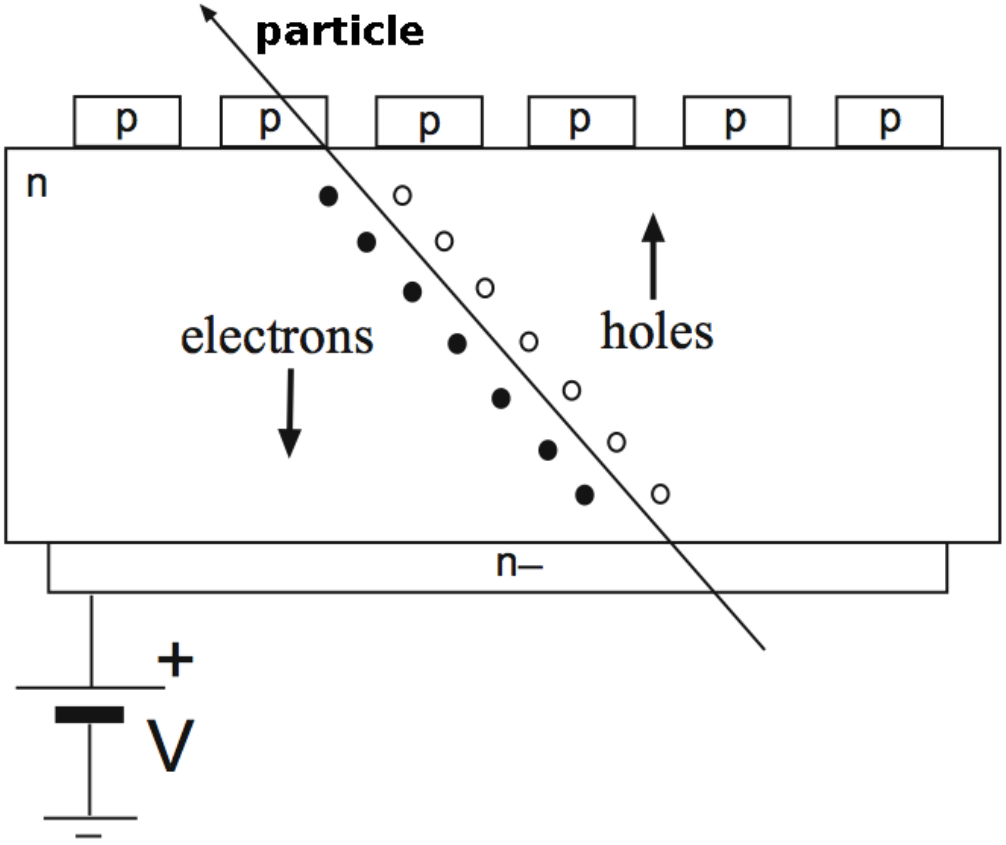

Figure 3.5: Generalisation of one of the silicon sensors in the SMT [70].

SMT at DØ is the inner most tracking system, directly surrounding the beryllium beam-pipe. The beam-pipe material and minimisation of the gap between the pipe and SMT help to reduce the effect of multiple-scattering, which is the deflection of the trajectory of a particle when traversing matter and density boundaries. Excessive multiple-scattering leads to imprecise interaction vertex determinations. The SMT is composed of horizontal barrels for low $|\eta|$ with interspersing vertical disks for high $|\eta|$. This design was used to increase the probability that a particle would traverse an SMT substrate perpendicularly, which would result in the best resolution. There are six barrel sections in the central region, each containing eight silicon read-out layers. More layers leads to a more precise momentum measurement from a trajectory that is more completely reconstructed, but also increases

the effect of multiple scattering. The layers are referred to as 'ladders'. A cross-section of a barrel can be seen in Fig. 3.6. Each barrel section is capped at high $|z|$ by a disk containing twelve wedge-shaped detectors, called an 'F-disk'. The central section spans 25 cm, covering the possible change in position of interaction point. At each end of the central section lie three additional F-disks. In both forward sections were two larger disks, named 'H-disks', that were removed after the RunIIa era. These provided tracking at large $|\eta|$. The H-disks were located at $|z| = 100.4$ cm and 121.0 cm, whereas the furthest F-disks are at $|z| = 53.1$ cm. Each H-disk comprised of twenty-four wedges. The outer radius of an SMT barrel is roughly 9.4 cm. A cross-sectional view of this arrangement can be seen in Fig. 3.7.

Most of the ladders are double-sided sensors, with the p-strips oriented to be parallel to the beam direction and n^- strips at a stereo angle. That angle in layers 3, 4, 7, and 8 is 2°. In layers 1, 2, 5, and 6 they are at 90°, with the exception of the two outermost barrel sections. These contain single-sided axial detectors.The H-disk wedges each contain a pair of single-sided detectors mounted back-to-back, where the strips of each had a relative angle of 15°. The pitch of the strips is dependent on the particular sensor. They are listed in Table 3.3. Typically, the single-hit resolution for the SMT was found to be around 10 μm.

Between RunIIa and RunIIb, an additional layer to the silicon detector, Layer 0 (L0), was added. Its radial volume extends from 16.1 mm to 17.6 mm, containing 48 radiation hard single-sided sensors. This improved the vertex resolutions, improving the impact parameter resolutions for particles with low p_T. For $p_T < 2$ GeV/c, the improvement was greater than 20 % [71].

3.2.3 Central Fibre Tracker (CFT)

An overview of the SMT and CFT can be seen in Fig. 3.8. The benefit of using the CFT is that it has very fast read-outs, which means that hardware triggering can use this tracking information. The CFT consists of 76,800 scintillating fibres

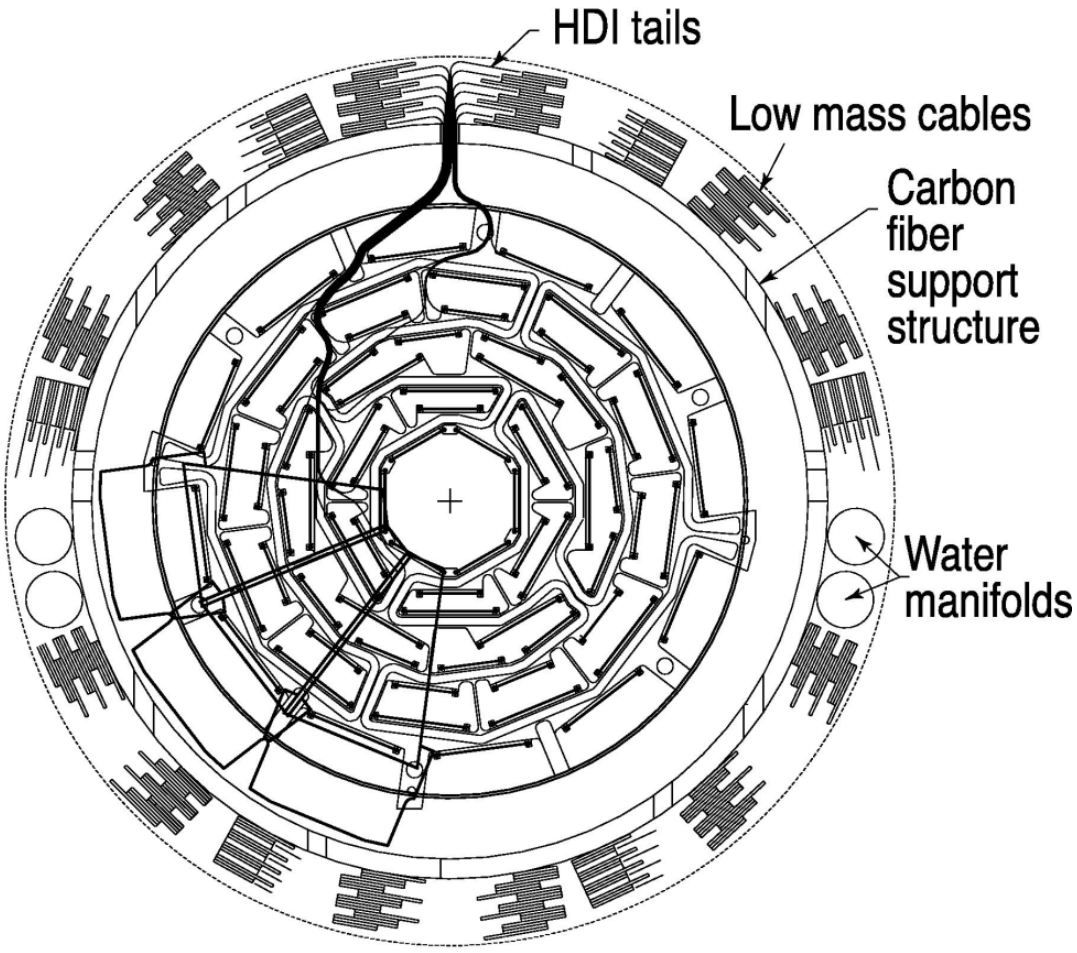

Figure 3.6: Cross-section of SMT barrel module [69].

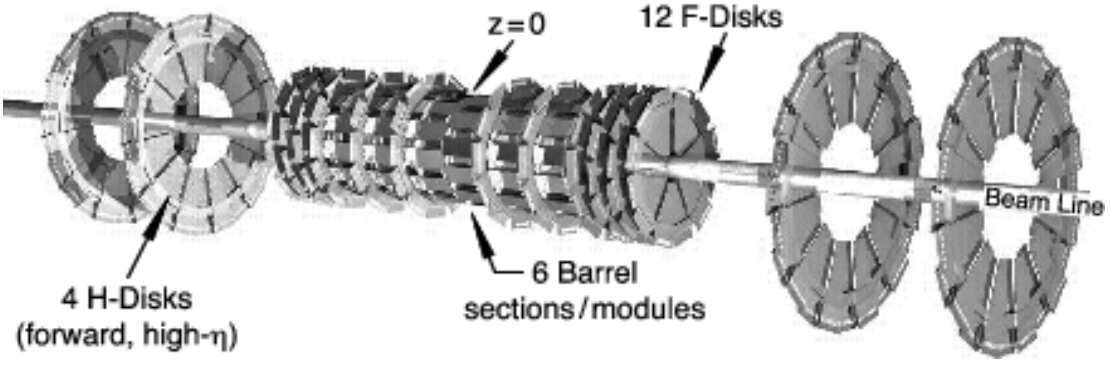

Figure 3.7: Diagram of the disk and barrel structure of the SMT [69]. The H-disks were only used in RunIIa.

Sensor	Pitch (μm)
Barrel axial	50
Barrel stereo 2°	62.5
Barrel stereo 90°	153.5
F-disk (p-side)	50
F-disk (n-side)	62.5
H-disk	80

Table 3.3: Pitches of the different silicon detectors in the DØ SMT.

contained within eight concentric cylinders. These fibres have a polystyrene base, but are doped 1 % by weight with an organic flourescent dye, paraterphenyl. When a charged particle excites the polystyrene, the dye emits photos of the approximate wavelength of 340 nm. Due to attenuation in the polystyrene, for this light to leave the module it is wave-shifted to 530 nm using a low concentration of 3-hydroxyflavone dye. The polystyrene is transparent to this longer wavelength, allowing the transmission of light along the fibre. The CFT covers a volume between a radius of 20 cm $< r <$ 52 cm from the beamline, with a length of 1.66 m for the inner layers to avoid the H-disks and 2.52 m for the other six layers. This means that the CFT offers tracking coverage for $|\eta| \lesssim 1.7$. Each cylinder contains a double layer of axial fibres and a double layer in the stereo direction, which is to say oriented in the z direction and at an angle of $\phi = \pm 3°$ respectively. The direction the positive angle points in is denoted $\hat{u}$ and the direction of the negative angle as $\hat{v}$. The stereo orientation alternates for each cylinder starting with $\hat{u}$ for the innermost cylinder.

The scintillation fibres are connected to clear fibre waveguides to transmit the wave-shifted light to the Visible Light Photon Counters (VLPC). These are silicon-impurity avalanche diodes requiring low temperatures to operate, typically ~ 9 K at DØ. The VLPC are capable of single photon detection with fast response times. These provide event triggering information from the axial doublet layers for tracks above a specified transverse momentum threshold. This information is passed on to further triggering layers which shall be described in Section 3.3. Typically, the

CFT offered a single-hit resolution of 150 μm.

Between RunIIa and RunIIb, the read-out electronics of the fibre tracker were upgraded to supply the time-of-flight information for every fibre.

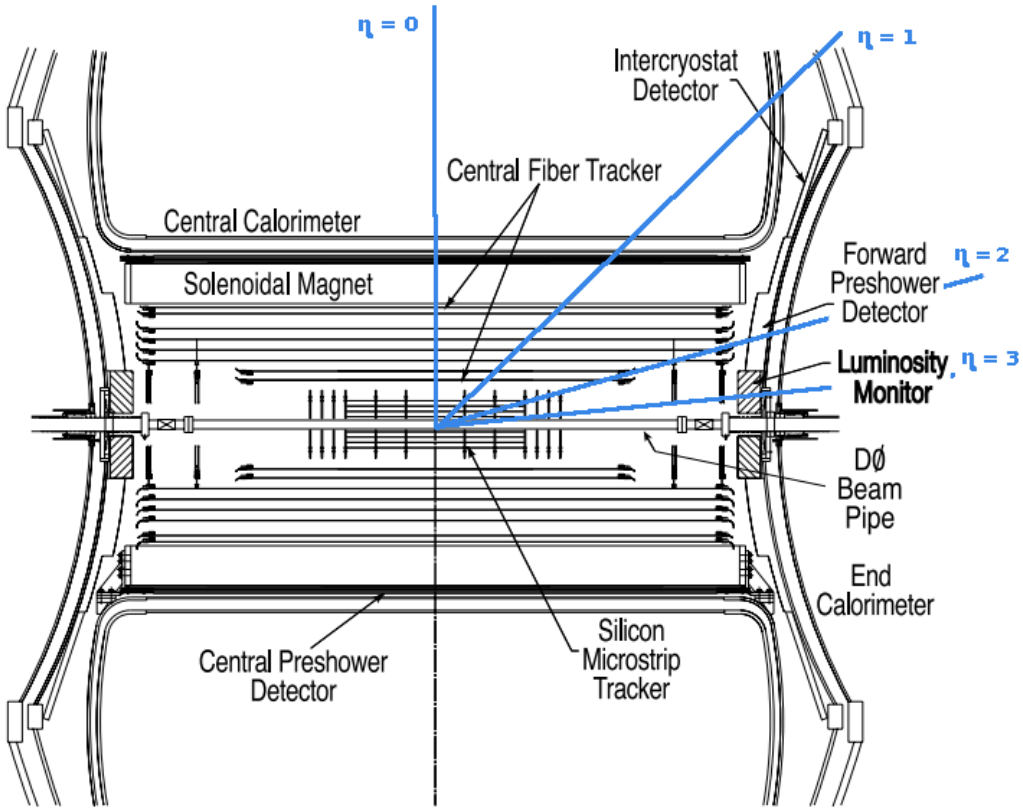

Figure 3.8: Cross-section in the xy plane of the central tracking system in relation to the outer components of the detector [69].

3.2.4 Solenoid

The superconducting solenoidal magnet surrounds the central tracking system, as can be seen in Fig. 3.8. The presence of a magnetic field curves the trajectory of moving charged particles. In doing so, momentum measurements can be performed on tracks. The solenoid was designed to fit within the RunI calorimeter and was fitted between RunI and RunIIa to optimise the momentum resolution of central tracking system, δ_{p_T}/p_T. It is 2.73 m long with a radius of 0.71 m and was operated with a current of 1500 A, which produced a magnetic field strength of 2 T. The solenoidal design was used as it produces a uniform magnetic field, homogeneous

to within 0.5 % [72]. This was in part achieved by using a larger density of coil with narrower windings at both ends of the coil. Thanks to this, the track trajctories were close to ideal helices. The thickness of the solenoid was designed to be approximately one radiation length to allow optimal performance by the central preshower detector, which resides directly outside of the magnet.

As mentioned previously, the regular reversal of the solenoid polarity is important for cancelling charge-dependent systematic effects within the tracking system. This polarity reversal was performed using a 5000 A DC mechanical motorised reversing switch and controller. This controller ensured that the polarity reversal occurred at zero load and with the power supply switched off.

3.2.5 Performance of the Central Tracking System

The combined SMT-CFT system could measure the position of the primary vertex in the z direction with a resolution of approximately 35 μm. For a track with low $p_T \approx 1$ GeV/c, the distance of closest approach perpendicular to the beam axis could be measured with a resolution of around 50 μm. This decreased to around 15 μm for tracks with $p_T > 10$ GeV/c. Taking into account the effect of the solenoidal magnet, the transverse momentum resolution was $\delta_{p_T}/p_T \approx 0.002 p_T$ [72].

3.2.6 Calorimeter

Between the central tracking system and the muon tracker system is a layered uranium and iron calorimeter system. This was used to measure the energy of photons, electrons, and hadrons by producing electron cascades from the incident particles and amplifying this electronic signal with photon multiplier tubes for recording. This system is not being discussed in detail because the analyses in this thesis do not use the calorimetry information. However, it is important to note that the calorimeter played the important role of blocking virtually all non-muonic particles from entering the muon tracking apparatus.

3.2.7 The Muon Tracker System

The identification and subsequent momentum measurements of muons was conducted via the muon detector system. High energy muons are an example of minimum ionising particles; the energy lost by muons created in $p\bar{p}$ collisions is primarily through ionising the detector material. As such, they are able to pass through all layers of the detector and so signals in the muon tracking system are most likely from muons. Muons couple directly to the weak force gauge bosons, W and Z, and so due to this form of particle identification the muon system was important in b-physics by allowing the identification of weak processes with heavy quarks, e.g. $b \rightarrow cW$.

The DØ detector has a system of muon drift chambers and scintillators. The drift tubes provided precise spatial measurements, while the scintillators provided fast signals for use in the triggering system. If a reconstructed track within the muon system is successfully paired with a track in the central tracking system, the two are combined and listed as a 'global muon'. There are three layers of the muon system, A, B, and C, where between the first and latter layers is a toroidal magnet. This allowed for a local measurement of the transverse momentum of a muon track. This could be combined with central tracking information to provide better matching for global muons, but was also used for a low p_T cut in the first level of the trigger system.

The position of the toroidal magnet can be seen in Fig. 3.4. Its central section is a 109 cm thick square annulus with the inner surface roughly 318 cm from the beamline, covering the region of $|\eta| < 1$. The end toroids cover the region of 454 cm $\leq |z| \leq$ 610 cm. During RunII the toroid coils were operated at 1500 A, producing a magnetic field strength of 1.8 T. Like in the case of the solenoidal magnet, the regular reversal of the toroid polarity allows the cancellation of many charge-dependent systematic effects introduced by the geometry of the muon chambers.

The muon system is split into two discrete sections; the Wide Angle Muon System (WAMUS) for $|\eta| \lesssim 2.0$, and the Forward Angle Muon Systems (FAMUS)

for $1.0 \lesssim |\eta| \lesssim 2.0$. Both have scintillation counters to provide the fast timing information, but different equipment for precision measurements differs between the two. WAMUS contains Proportional Drift Tubes (PDT), whilst FAMUS has Mini Drift Tubes (MDT). An exploded view of these components can be seen in Fig. 3.9. The PDTs in the WAMUS are made from rectangular drift tubes approximately 10 cm across and 6 cm long. They are filled with a mixture of gasses; 84 % argon, 8% methane, and 8% CF_4. An anode wire runs through the centre of each cell with cathode cells placed above and below it. The wires are paired up, sharing read-out electronics at the end of each PDT. PDTs facilitate the measurement of the drift time of electrons to the anode wire, giving the xy position of the hit to a resolution of 1 mm. The drift time to a cathode pad allows the measurement in the z direction to a resolution of 5 mm. Only the 'A' layer pads are fully instrumented with electronics, whereas only around 10 % of layers 'B' and 'C' are instrumented. There are multiple reasons for this; for tracks traversing all three layers, the pad co-ordinate of the outer layers does not significantly improve resolution or pattern recognition, the information from A-layer pads can be used for track matching and background rejection for any track reaching the muon system, the B- and C-layer pads would have sufficient electronics to monitor the signal gain to judge the aging in the PDTs, and because fully instrumenting the outer layer pads would be too expensive. For those pads without full electronic instrumentation, the z position is inferred from the difference between the arrival time of the signal pulse at the end of the cell's anode and the end of the signal read-out of the partner wire. The resulting resolution was of the order 10 - 50 cm. 'Aϕ' scintillator counters cover the A player PDTs. They provided fast read-out for triggering on muon and for rejecting out-of-time backscatter from the forward direction. The scintillator hits were matched with tracks in the first level triggering information for high p_T single muon and dimuon conditions. The Aϕ scintillator counters are uniformly distributed in ϕ and provided a timing resolution of 2 ns.

As mentioned, the FAMUS has MDTs, which are similar to PDTs but have

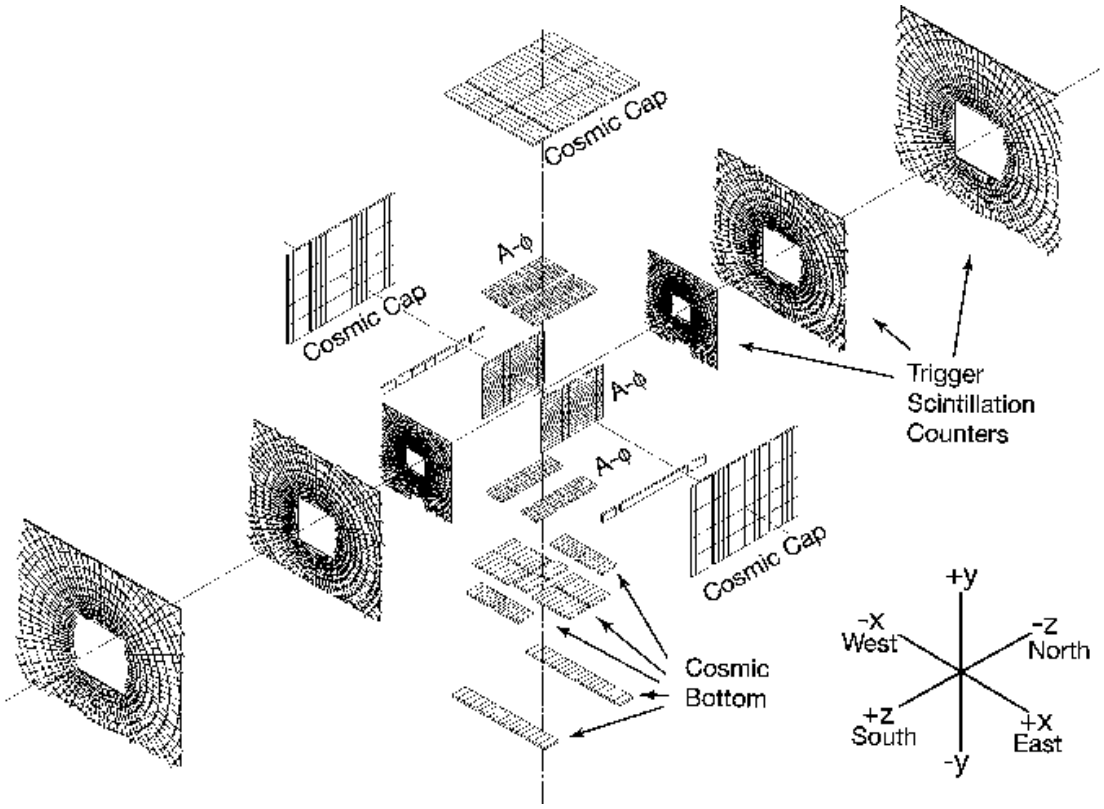

(a) Muon scintillation detectors

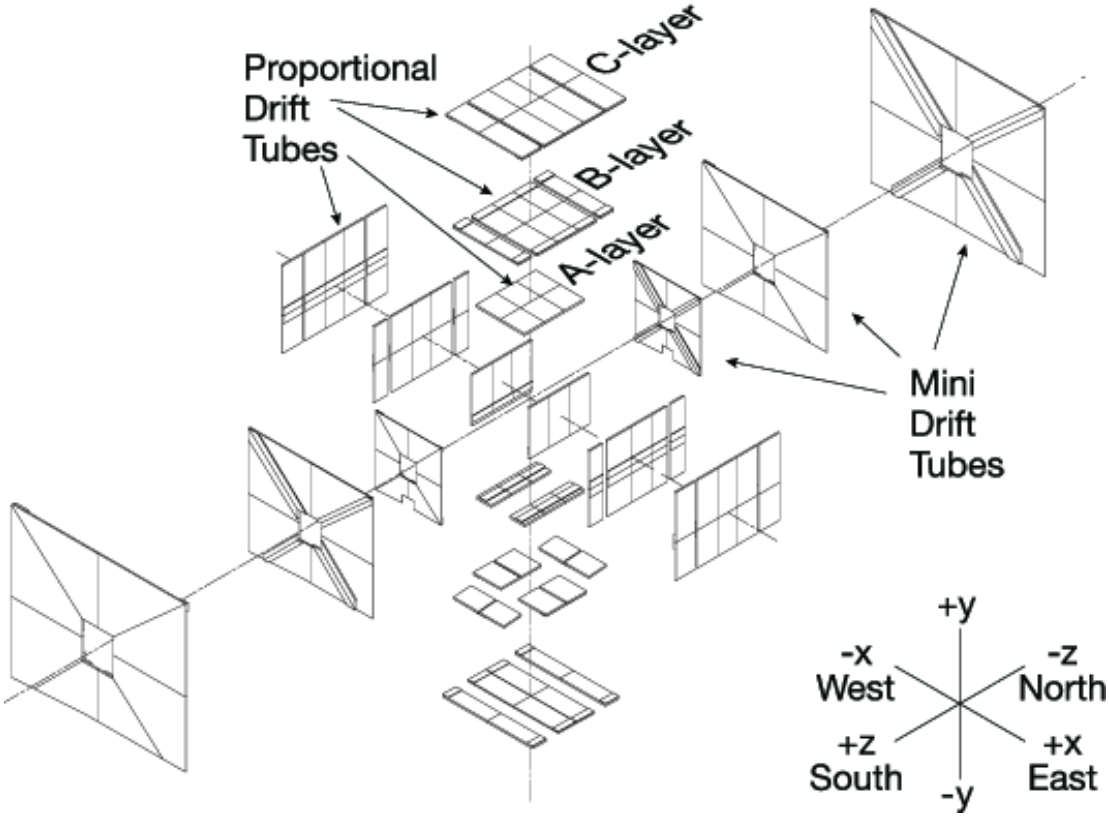

(b) Wire chambers of muon system

Figure 3.9: Exploded view of the muon system [69].

a cross-section of only 9.4 mm x 9.4 mm and have a gas mixture of 90 % CF_4 and 10 % CH_4. Like in the central region, layers 'A', 'B', and 'C' of the forward system each have arrangements of MDTs. Although the intrinsic resolution of the chamber is 350 μm, the hit resolution was only 0.7 mm due to digitising electronics. The signal arrival time is measured to a resolution of 18.8 ns. In FAMUS, the scintilators are present in all layers, uniformly segmented in ϕ and η. The timing resolution of these was better than 1 ns.

3.2.8 Luminosity Monitor

Luminosity Monitor (LM) detectors were placed at $|z| = 140$ cm, each consisting of an array of twenty-four scintillation counters and a photo-multiplier tube (PMT) read-out covering the region of $2.7 < |\eta| < 4.4$. The time-of-flight resolution for the counters was approximately 0.3 ns. The luminosity, $\mathcal{L}$, was determined from the average number of inelastic collisions per beam crossing detected by the LM, $\bar{N}_{\mathrm{LM}}$,

$$\mathcal{L} = \frac{f\bar{N}_{\mathrm{LM}}}{\sigma_{\mathrm{LM}}}, \tag{3.3}$$

where f is the Tevatron beam crossing frequency and σ_{LM} is the effective cross-section of the luminosity monitor, including acceptance and efficiency corrections. $\bar{N}_{\mathrm{LM}}$ is determined using Poisson statistics by considering the fraction of beam crossings with no interactions. The purpose of the LM was to determine the luminosity at DØ using inelastic $p\bar{p}$ collisions, though it also provided a fast method measuring the primary vertex position and beam halo rates.

Discrimination between beam halo backgrounds and $p\bar{p}$ interactions was performed using time-of-flight information to find the z co-ordinate of the interaction, $z_v = \frac{c}{2}(t_- - t_+)$. $t_\pm$ was the particle time-of-flight as measured at the corresponding LM. Events with $|z_v| < 100$ cm were considered to have originated from an interaction, whereas halos were characterised in the $\pm z$ direction by having an

interaction co-ordinate of $z_v \approx \mp 140$ cm.

3.3 The DØ Trigger System

During RunII, the Tevatron crossed proton and antiproton bunches every 396 ns. With the total $p\bar{p}$ cross-section being approximately 100 mb, there were of the order of a million $p\bar{p}$ interactions per second. This number was far beyond the recording capability of DØ so, considering that the interesting events only made up a cross-section of 10-100 μb or less, a system of event filtering was essential. A series of triggers performed 'on-the-fly' filtering so that only interesting events were written to tape for off-line analysis. Three layers of triggers were used by DØ, named 'Level 1', 'Level 2', and 'Level 3'. Level 1 was entirely hardware based, with interesting event signatures being sought after in each subdetector independently. This reduced the event rate by a factor of roughly a thousand, outputting at a rate of around 2 kHz. Level 2 took the Level 1 passing events and introduced individual object reconstruction; correlations performed using subdetector-based embedded microprocessors passed information to a global trigger processor, roughly halving the rate from Level 1. Only if the Level 2 trigger was passed did the whole detector read out. The resulting event was built by the Level 3 Data Acquisition System (L3DAQ) and sent to a processing farm for limited reconstruction. Level 3 triggers were based on complete physics objects and the relationship between them, such as rapidity separating the objects or their invariant masses. Events passing Level 3 triggers were written to tape, typically at a rate of around 50 Hz. Levels 1 and 2 had buffers where passing events were stored whilst waiting to be read out to the next trigger layer. This reduced the probability of losing a signal event due to speed limitations in computer read-outs.

The selection of triggers used was dependent on instantaneous luminosity, as the bandwidth required by the triggers increased with luminosity. To limit the event rate to the total bandwidth required, a series of prescale were used. Each prescaled governed a range of luminosities, rejecting a random fraction of passing

triggers to maintain a manageable write-out frequency. However, if an event passed more than that one rejected trigger it would still be recorded.

An overview of the trigger systems can be seen in Fig. 3.10.

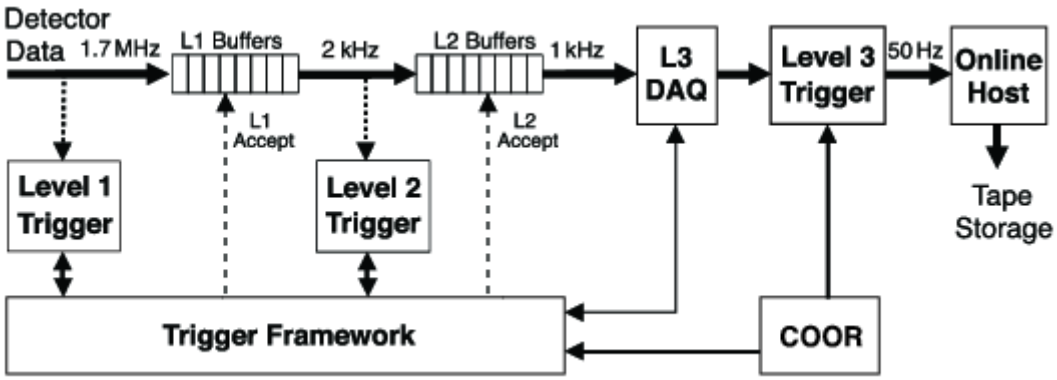

Figure 3.10: Schematic overview of the trigger system [69].

3.3.1 Level 1

Level 1 is a hardware based trigger that was designed to examine every event and make 'yes' or 'no' decisions based on threshold values. For example, the muon (L1Muon) and central track (L1CTT) triggers were examined, both combined and separately, for tracks that exceeded specific thresholds in transverse momentum. Due to the extreme event rate, minimising deadtime was essential at L1. Events were stored in pipelined buffers where a decision on whether to accept or reject it was required to be made within 3.5 μs. The accept rate of L1 acception rate was limited by the time taken to read-out the subsystems of the detector. L1 was designed to accept a beam crossing rate of 2.5 MHz and output events at a rate of 2 kHz.

3.3.2 Level 2

The Level 2 (L2) trigger was designed to reduce the rate from 2-10 kHz to approximately 1 kHz. A global processor (L2Global) using information from parallel subdetector preprocessing systems was used to test for physics signatures. For

example, it reconstructed charged particle tracks found in the CFT at L1 with the increased precision by including SMT preprocessor information. The L2 SMT Track Trigger (L2STT) performed on-the-fly pattern recognition from this data, and also measured the impact parameter of tracks precisely enough to tag the decays of long-lived particles. Specifically, B hadron triggers could be used this way. If an event was passed by L1/L2 triggers, a full read-out of the detector would be requested for further analysis by Level 3 (L3). An unbiased sampling mode could be set which passed all L1 accepted events to L3 without rejection. However, the results that L2 would have produced were still recorded. A diagram of the relationships between L1, L2, and the subdetectors can be seen in Fig. 3.11.

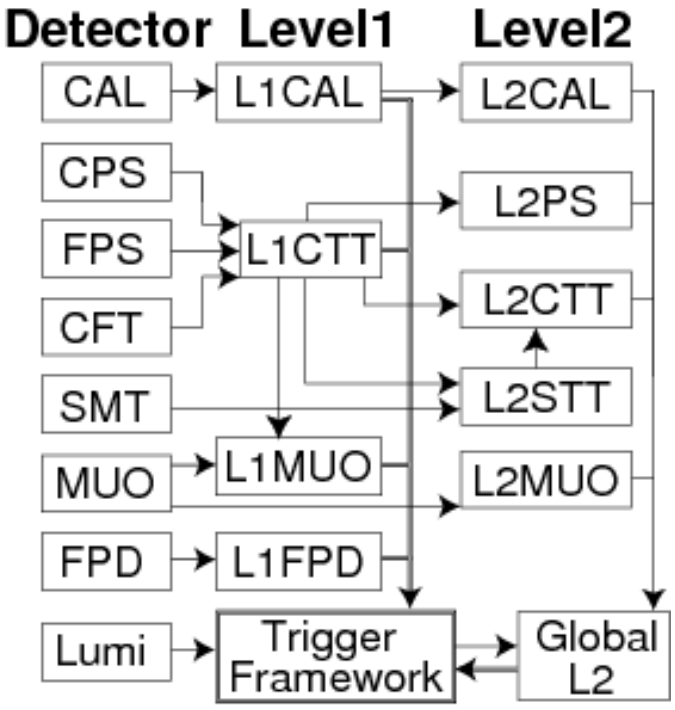

Figure 3.11: Block diagram of the L1 and L2 trigger systems [69].

3.3.3 Level 3

The L3 trigger was a fully programmable software trigger which performed all the basic elements of an offline reconstruction with simpler reconstruction algorithms.

Complete physics objects and the relationships between them could be analysed and cut upon. The software unpacked the raw data of the full detector read-out, located hits, formed clusters, applied calibration corrections and reconstructed objects such as vertices, tracks, leptons, jets and missing transverse energy. Online monitoring kept note of the beamspot information, such as mean position, transverse spread and tilts. This information was used to calculate the position of the primary vertex for each event in 3-dimensional space. As such, impact parameter triggering could be used to perform b-tagging with the tracking, jet and vertex information.

If an event was accepted at L3, then it was recorded to tape for full offline reconstruction. The average output rate was approximately 50 Hz.

3.3.4 b-Physics Specific Triggering

The datasets created for the b-physics analyses at DØ were all dependent on muon identification. There were three methods of muon triggering used [74]:

- dimuon triggers – J/Ψ decays, rare $B_s \rightarrow \mu\mu$ searches, and single inclusive muon decays where the second muon is used to identify the flavour of the B meson at decay.

- lifetime-unbiased single-muon trigger – Track-matched muons with a momentum threshold of 3, 4 or 5 GeV/c.

- impact-parameter biased single-muon triggers – The flavour of the B meson can be inferred by selecting muons with a large impact parameter.

The trigger rates used in b-physics were in direct competition with other physics analysis groups for bandwidth. As the other analyses tended to require high p_T triggers, the b-physics triggers could utilise the more available bandwidth at lower luminosities. As such, the b-physics triggers began to dominate all others for instantaneous luminosities below $\sim 22 \times 10^{30}$ cm^{-2}s^{-1} [74].

3.3.5 Tracking

Charged particles passing through the SMT and CFT components were registered as hits, which formed clusters to be used by tracking algorithms. Within the SMT, a number of strips could register the same track. Analogue-to-Digital Counts (ADC) were performed on each registering adjacent strip, allowing the central position of the hit cluster to be determined by the pulse height weighted average, $\bar{n}$,

$$\bar{n} = \frac{\sum_i^N n_i w_i}{\sum_i^N w_i}, \tag{3.4}$$

where n_i is the strip number, w_i the ADC value for the i^{th} adjacent strip, assuming the count is above a preset threshold. The centroid of the cluster, u, was calculated as $u = u_1 + (\bar{n} - 1)p$, where u_1 was the position of the first strip and p was the pitch of the strip. These local co-ordinates would then be converted to the global system.

Similarly, in the CFT the light yield was converted to an ADC value using individual calibrations for offset and gain in each fibre. Adjacent hits above the preset threshold are included into the CFT hit cluster and the centroid defined as the mid-point between cluster edges.

As previously mentioned, muon candidates required the identification of hits within the muon detectors and in the central tracking detector to be considered global. The hits within the muon system must also have form straight line sections. The hits in the muon scintillator were determined from the drift time and add to the precision of the reconstructed track. Once all the hits had been reconstructed, links between them were formed for those with spatial separation less than 20 cm. Those links were combined to identify straight-line track segments. If two segments could form a new segment, and those segments could be extrapolated to match scintillator hits, the track was refitted. Fits were formed across the two outer layers of the muon system, 'B' and 'C', as there was no magnetic field between

them. From all identified segments, the best were selected by minimising the χ^2/ndf against a track hypothesis. In the case of only two hits being detected, the segment that could be extrapolated closest to the primary vertex was selected. A 'local' muon track was formed using hits from the 'A' and 'BC' layers, including the effects of the toroidal magnetic field, energy deposition and multiple scattering.

3.4 Software

Most of the software for RunII operations was written in C++. RunI legacy software and older algorithms that were written in FORTRAN were made available via a C++ wrapper. This section will describe the computing and software involved in translating the raw detector information to a usable database of physics objects.

3.4.1 Offline Event Reconstruction

The DØ Offline Reconstruction Program (DØReco) [75] reconstructs the physics objects used in DØ physics analyses. It has the ability to process both simulated events, produced by the DØ Monte Carlo (MC) program, and collider events recorded after passing L3. DØReco is designed to be run on offline production computer farms, where the results are saved to a central data storage system for later analysis. Two output formats can be produced; 'Data Summary Tapes' (DST) contains the completely reconstructed physics object along with intermediate subdetector information, and 'Thumbnails' (TMB) the contain a summary of the physics objects and detector status in the DST. The former has a typical size of 150 kB/event, whereas the latter is only 15 kB/event. As such, physics analyses tend to use the TMB format to reduce processing time and disk space requirements.

DØReco uses several steps to reconstruct events; these are outlined in Fig. 3.12. The first step covers subdetector-specific processing. The raw subdector in-

formation is unpacked, decoded, and has calibration constants applied according to the individual electronics channel. This information is used in the second step, where calorimeter signal clusters and tracking hits are determined. Alignment information is used to associate the hits within subdetector sections to physical space. Step three focuses on the tracking detectors. SMT and CFT hits are combined to reconstruct global tracks using CPU intensive algorithms that will be discussed in Section 3.4.2. The resulting track chunk information is sent on to step four, vertexing. Firstly, the primary vertex ($p\bar{p}$ interaction point) candidates are found, which are used for kinematic calculations such as total transverse energy. Afterwards, secondary vertex candidates are identified, which are associated with the decay of long-lived particles. The resulting vertex candidate information is sent to the final stage, particle identification. This is the step which assigns physical object types to the information from the preceding four steps. Electron, photon, muon, jet, and missing transverse energy (neutrino) candidates are found. Afterwards, heavy-quark and tau decays are identified.

However, b-physics analyses rely almost exclusively on the tracking and muon information. To this end, a modified DØReco package was developed, 'BANA'. Central track and global muon candidates exported from DØReco stage three are used to perform vertex searches that are optimised for b-physics studies. Smaller datasets can be created as a result, allowing for an increased b-physics processing speed. BANA will be covered in more detail in Section 3.4.5.

3.4.2 Track Reconstruction at DØ

The tracking procedure at DØ uses three algorithms, as outlined in Fig. 3.13; Histogram Track Finding (HTF) [77], the Alternative Algorithm (AA) [76], and the Global Track Finder (GTR) [78]. HTF uses a combination of Hough transform to reduce the combinatorial backgrounds from axial-stereo hit association, followed by the slower Kalman filtering technique. AA also uses the Kalman filtering with a simplified track propagator to perform track finding, leaving the accurate prop-

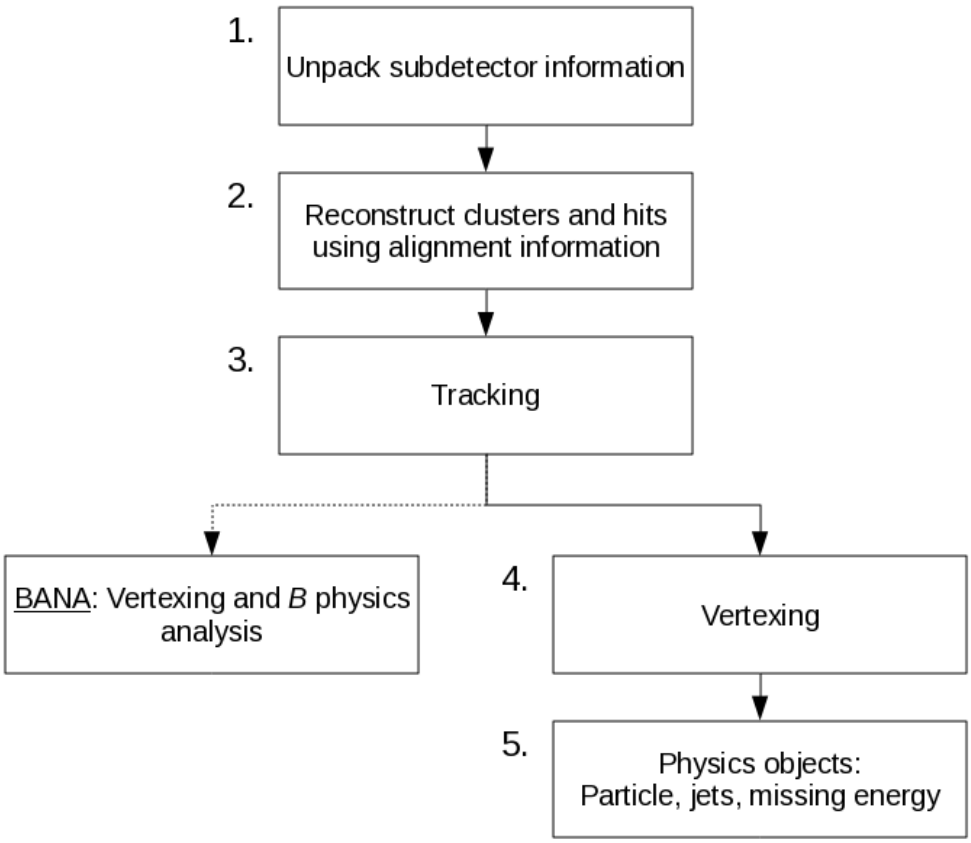

Figure 3.12: Hierarchical steps of the DØ Offline Reconstruction Program, including offshoot to the BANA package.

agation and the determination of track parameters to a later stage. HTF and AA compliment each other; AA has higher efficiency for low p_T tracks and high impact parameter, making it more suited for b-physics, whereas HTF performs better for high p_T tracks. HTF uses the transformation of hits from the (x, y) co-ordinate space to the parameter space (ρ, ϕ), where ρ is the curvature of a track, $\rho = qB/p_T$, and ϕ is the direction of the track at its closest approach to the beamline. A hit is represented as a line in this parameter space, and a track as a point. Thus, hits from the same track will intersect at the point representing the track.

AA builds a list of track hypotheses by performing the following; a series of three axial SMT hits are selected that contain at least one stereo measurement per hit, which are extrapolated to the next layer of the SMT or CFT, adding a found track chunk to the hypothesis and refitting if found. If multiple hits are found, a hypothesis is created for each hit using shared previous hits. If there is a case that no hit is found where expected, a 'miss' is recorded for that track hypothesis, which accounts for possible detector inefficiencies. The extrapolation continues until either three misses are noted or the outside of the CFT is reached. The track hypothesis is sent to the next stage if the hit-versus-miss count is sufficient.

AA and HTF track hypotheses are added to a common pool which is later filtered in a separate AA phase. The filtering involves a two-pass technique. First, the track hypotheses are ordered into a sequence in order of a combination of; greatest number of track hits, fewest misses, and smallest χ^2 of the track fit. The tracks are then filtered further in order of greatest number of axial hits shared with the previous track, N_s, compared to the total number of axial hits on the track, N_t. A track passes the first filter if either of the following two conditions are met; $N_s \leq \frac{2}{3}N_t$ and $N_t - N_s \geq 4$, or $N_s \leq \frac{1}{5}N_t$. Those passing have their primary vertices found using the method described in Section 3.4.3. These are used as the contraint for the second filter pass.

The passing tracks are passed to GTR to be refitted. GTR takes into account multiple scattering and ionisation losses in the detector material, resulting in a

much more accurate result compared to Kalman fitting. The output tracks are used to construct physics objects, such as primary and secondary vertices, jets, leptons, and so forth. They can also be matched to muon tracks to form global muons and to calorimeter clusters for global electrons.

3.4.3 Primary Vertex

The primary vertices are determined per event using the beamspot position and track candidates. The position of the beamspot tends to remain stable throughout a run, and so can be ascertained from using the run-averaged position from a beamspot database. This average becomes a constraint in the fitting of a primary vertex, which is done by minimising the following function [79],

$$\chi^2 = \sum_{\alpha} \sum_{\alpha,\,\beta=1,2} d^a_\alpha (S^{-1}_a)_{\alpha\beta} d^a_\beta + \sum_{i=x,y,z} \left(\frac{V^{sp}_i - V_i}{\sigma^{sp}_i} \right)^2 \tag{3.5}$$

$\vec{V}$ is the position of a primary vertex. $d_{\alpha/\beta}$ are two-dimensional vectors of transverse/longitudinal impact-parameter components for the track a. S is the covariance matrix of the measured impact parameter components. The first term is summed over all tracks. V^{sp}_i and σ^{sp}_i are the beamspot position and size for (x, y) co-ordinates, i. Using the beamspot constraint reduces the resolution of a primary vertex from approximately 30-60 μm to 20-25 μm. To compensate for the case where one of the tracks may not actually be from a primary vertex, the procedure is iterated for each track in the list, each time without including that track in the calculation. If the difference in χ^2 is greater than 9, that track will be removed from the list of candidates that come from a primary vertex. This is performed until no further tracks are removed by this procedure.

Secondary vertices are found by only considering the first term of Eqn. 3.5.

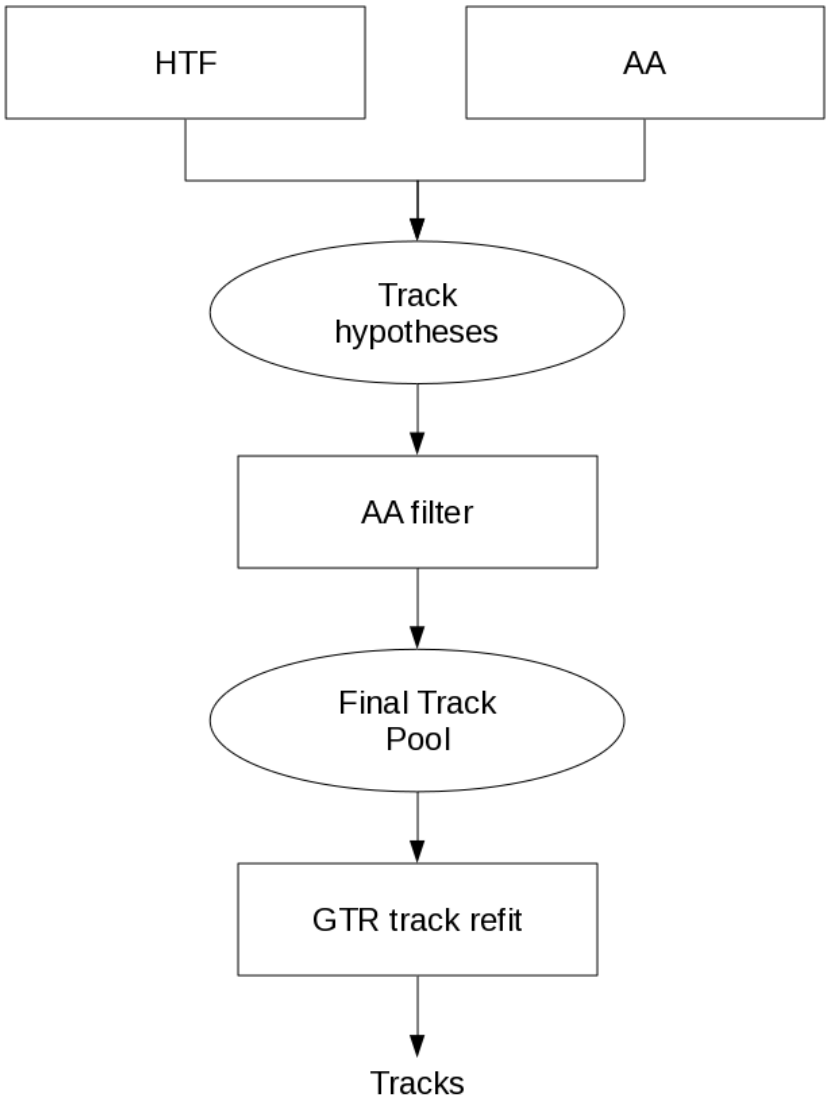

Figure 3.13: DØ Tracking procedure.

3.4.4 Event Simulation

Event simulation is a useful tool in many analyses; helping to determin optimisation cuts, expected results, fractions of decay types in a sample, and so forth. Monte Carlo (MC) events simulate a beam crossing in the detector using a multitude of software packages. DØ_Mess [80] acts as a filter to reject events according to topological or kinematic selection criteria. This is important as fully simulating decay chains and interactions is a time consuming task, there is little point in wasting resources on events that will never pass selection criteria. The first stage of the simulation is to simulate the $p\bar{p}$ interaction, producing a set of decays according to the hard-scattering underneath the event. This is handled by PYTHIA [81], which outputs four-momenta and vertex information. Another package, EVTGEN [82], is used to govern the simulation of b-hadron decays and the daughter particles produced. It is a framework that can handle more sophisticated decay modelling, including $\mathcal{CP}$ effects in complex sequential decays, decay chains where angular distributions are important, and lifetime modelling.

The DØ detector is not a homogeneous mass; it has many devices made of different materials with varying thicknesses. This must also be taken into account to simulate how MC particles interact with the detector, and so determine how their hits will be reported by the detector. DØGStar [83] uses the GEANT [84] program to calculate the paths simulated particles would take through active media, the energy deposition, and any secondary interactions with the detector. The DØSim [85] program takes the MC response and applies modifications to account for detector related effects, such as inefficiencies, electronic noise, and multiple interactions per beam crossing.

For the analyses covered in this thesis, the simulated data was produced using various versions of the DØ software that correspond to RunIIa, RunIIb1, RunIIb2, and RunIIb3 eras separately, taking into account calibrations and luminosity levels present at those times. PYTHIA and EVTGEN were used to manage the decay chains.

3.4.5 BANA

The BANA package [86] provides a front-end for b-physics analyses at DØ, allowing access to tracking and vertex information for the use of reconstructing decays. It can process DST and TMB DØRECO formats, but is normally used with a stand-alone data format, 'AADST'. AADSTs only store the information that is typically required for b-physics analyses, such as:

- Complete track information;
- Triggers fired;
- Muon ID information.

This compact format is reduced enough to allow local storage of analysis data to facilitate rapid analysis code development and testing, but can also be uploaded to and accessed with the Fermilab Sequential Access via Metadata (SAM) [87] system. SAM is an example of a grid computing system, which distributes computing over a cluster of computers. The BANA package provides a C++ library that is fully compatible with databasing frameworks, such as ROOT [88] or PAW [89], and can easily incorporate any other C++ analysis method, such as the 'Toolkit for Multivariate Data Analysis' (TMVA) [90]. Inbuilt to BANA are the following useful methods for physics analyses:

- Reconstruction of primary and secondary vertices;
- Calculation of transverse and longitudinal projections of the impact parameter of a track, along with uncertainties;
- Calculation of significance of track with respect to primary vertex;
- Jet reconstruction with the DURHAM clustering algorithm [91];
- Reconstruction of particle decays, performed by assigning an expected masses to a non-muon tracks and combining them to form a parent particle. The

position of decay, vertex, invariant mass, and momentum of a parent particle can be calculated;

- Constraining the momenta of daughter particles using the parent particle mass, which allows improvements to mass resolution;

- Flavour tagging.

The vertex reconstruction, track significance, and track combination utilities were used in the analyses in this thesis. The reconstruction of particle decays can be extended from a single chain to include an entire decay chain. For example, $B \to D^*\mu(\nu), D^* \to D^0\pi, D^0 \to K\pi$ can be reconstructed by combining candidates for the final state tracks of the charged pions, kaon, and muon. Quality cuts, such as on the χ^2 of the vertex formed by two tracks, can be used to discount ill-fitting candidates.

A 'single muon skim' was created for the entire RunII dataset and stored in AADST format and stored on SAM. These were events that passes the unbiased or dimuon triggers mentioned in section 3.3.4 with muons that pass the following quality and kinematic cuts [92]:

- Muon candidates must have recorded segments in at least the outer two layers of the muon system, and have a locally converged track hypothesis;

- Matched central track with at least two SMT and two CFT hits;

- Transverse momentum, $p_T(\mu) > 1.5$ GeV/c.

This combination of requirements is loose enough to facilitate a broad scope of semi-leptonic b analyses.

Chapter 4

Data Analysis - Asymmetry Extraction

This chapter will describe the process of extracting the semileptonic charge asymmetry in B^0_d mixing, a^d_{sl}, including the subtraction of various result biasing background asymmetry sources. Section 4.1 outlines the process for extracting the raw time-integrated charge asymmetry, which is used in both the kaon background asymmetry extraction and in the main analysis. Section 4.2 will cover the detector induced asymmetries, which are a result of detector geometry. Section 4.3 details the extraction of the kaon track reconstruction efficiency asymmetries, which act as a background to the main analysis' raw asymmetry. Section 4.4 covers the extraction of the a^d_{sl} value.

4.1 Extraction Overview

As discussed in Eqn 2.73, a charge asymmetry can be expressed by counting the difference and sum of events with a differing charge tag. However, in an experimental setting, access to pure signal events is non-trivial. One must instead extract a 'raw' asymmetry from as clean a reconstruncted signal as is possible from selection criteria. From this, any asymmetry from 'background' processes must be removed. Finally, a dilution factor, f, must be applied to account for the purity

of the sample;

$$a = \frac{A_{\text{raw}} - A_{\text{bckg}}}{f}. \tag{4.1}$$

For any asymmetry search, A_{raw} corresponds to Eqn 2.73 to within the limits of the experimental apparatus, in that a difference between the yields of the charge states is divided by the total yield;

$$A_{\text{raw}} = \frac{N^+ - N^-}{N^+ + N^-}. \tag{4.2}$$

A_{bckg} is the combination of any other source of a physical charge asymmetry, for example a difference in reconstruction efficiencies between positively and negatively charged final state particles, for example the positive kaon asymmetry discussed in section 4.3. f is the 'dilution fraction' to account for the purity of the extracted signal. It is the fraction of the candidates which contribute to the extracted yield (N) that originate from the particular process being investigated. Any background process entering the signal that does not contribute to the asymmetry acts to wash out the extracted asymmetry by increasing the denominator of Eqn 2.73 without contributing to the numerator. The type of dilution is dependent on the specific study, as shall be discussed in the later sections. For example, in the a^d_{sl} measurement, candidates which do not originate from an oscillated B^0_d meson do not contribute to the asymmetry, but do contribute to the denominator of Eqn. 2.73.

4.2 Detector Asymmetry

A particle detector will have global and local differences in the acceptance and reconstruction efficiencies for positive and negative particles. These introduce a bias to any physical charge asymmetry one would wish to measure, and so have to be taken care of. An example of a global difference is the 'forward-backward'

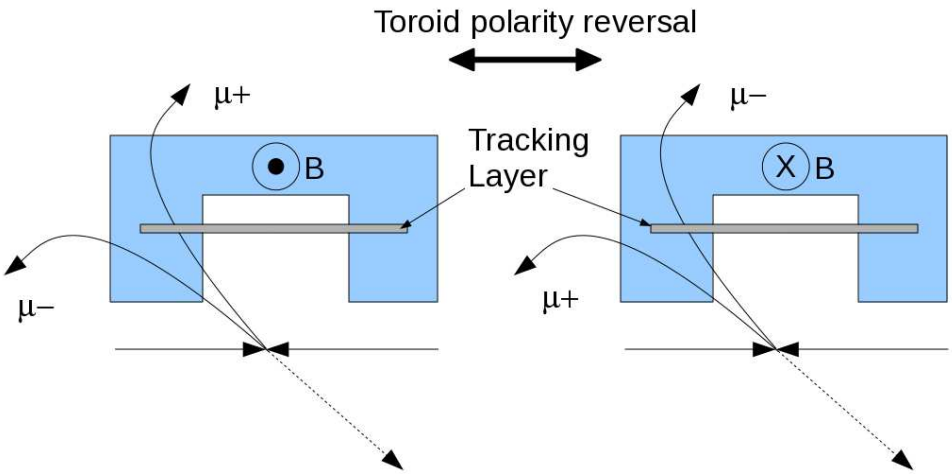

Figure 4.1: The effect of changing the toroid polarity on the acceptance of muons and anti-muons of a particular direction. Without the reversal at regular intervals a detector asymmetry would be introduced.

asymmetry, $A_{\rm fb}$, which can be seen for muons reconstructed from W decays. In $p\overline{p}$ collisions, the dominant W^+ production process is $u + \overline{d} \rightarrow W^+$, and conversely for W^-, $\overline{u} + d \rightarrow W^-$. The valence u quark carries a larger fraction of the proton momentum than the d quark which means, when taking into account that there are two u valence quarks, the $W^+(W^-)$ should prefer to travel in the proton(antiproton) direction. The same correlation should be observed in W leptonic decays. This produces a reconstruction asymmetry between the charges if the detector has asymmetric reconstruction efficiencies between the forward and backward directions. As such, an apparent charge asymmetry of W decays is observed if the detector is forward-backward asymmetric.

An example of a local difference is a difference in acceptance or reconstruction efficiency between particles and antiparticles based on the direction of track bending within the solenoid/toroid due to the distribution of matter in the detector or dead electronic channels. However, as mentioned in Sections 3.2.4 and 3.2.7, the polarities of the DØ solenoid and toroid magnets were regularly reversed during data-taking. Reversal of one of the magnets exposes the opposite section of the particular tracking system to the flux of charged particles that was previously

felt in the first half. Figure 4.1 gives an illustration of this process. This means that the net asymmetry induced by global differences in reconstruction efficiencies between positive and negative tracks cancels to first order if the contribution of the sample is equal for each toroid/solenoid polarity combination. This would be done by extracting the signal yield for the decay a particular analysis requires for each subsample of polarity combination (toroid/solenoid = $++$, $+-$, $-+$, $--$) and determining a reweighting factor to be applied per candidate in a secondary reprocessing of the data. The reweighting factor would ensure equal contribution by adjusting the yield of each subsample, which reduces the overall sample size. The weighting factors would be

$$w_{(\pm,\pm)} = N_{\text{min}}/N_{(\pm,\pm)}, \tag{4.3}$$

where $(\pm, \pm)$ is the toroid and solenoid polarity respectively, N_{min} is the smallest subsample yield, and $N_{(\pm,\pm)}$ the yield of that polarity subsample. Thus, the smallest sample has unity weighting.

Any remaining parameter asymmetries induced by the detector reweighting should be identical for positive and negative tracks. This can then be dealt with by subtracting the number of positive tracks from the number of negative tracks or vice-versa, hence subtracting the universal systematic issue. As will be discussed, this is part of the raw asymmetry extraction. The following detector asymmetries are removed by this process:

- Asymmetry accounting for the difference in reconstruction efficiency for particles with charge q, after toroid polarity, β, flip - an asymmetry between $q\beta > 0$ and $q\beta < 0$.

- Detector North-South asymmetry, which accounts for differences in the distribution of dead material between pseudorapidity $\eta > 0$ (Northern) and $\eta < 0$ (Southern).

- Particle range-out asymmetry due to the magnets. This is most prevalent for

muons in the toroid - the magnetic field pulls muons with trajectories close to the toroid end into the gap between the central and end toroid, which has a lower reconstruction efficiency. There is no significant range-out effect for particles entirely reconstructed in the central tracking system with the solenoid. The range-out effect changes if either q, β, or the sign of η changes, so the associated asymmetry is between $q\beta\eta > 0$ and $q\beta\eta < 0$ candidates. An illustration can be seen in Fig. 4.2.

- Any remaining detector related forward-backward asymmetry which remain after toroid polarity reversal, so between $\beta\eta > 0$ and $\beta\eta < 0$ candidates.

The event weighting method cancels detector asymmetries during the subtraction in the numerator of Eqn. 4.2, but there was an alternative method of dealing with these background asymmetries that was previously used in some DØ analyses [70]. Their method extracted all of the above detector asymmetries instead of negating them by cancellation. It is referred to as 'System Eight' [93], and has the advantage of not reducing the total sample yield like reweighting does. However, the process involves splitting the sample into more subsets to extract each detector effect, which may not ensure the same final statistical uncertainties as an unsplit sample. Uncertainties in the extracted background asymmetries, and correlated uncertainties in signal and background yield extractions across a greater number of histograms can contribute to an increased final uncertainty. The method requires eight signal yields of each muon charge, toroid, and pseudorapidity sign subset, which are used to solve eight equations,

$$\begin{aligned} n_q^{\beta\gamma} =& \frac{1}{4} N \epsilon^{\beta} (1 + qA)(q + q\gamma A_{\mathrm{fb}})(1 + \gamma A_{\mathrm{det}}) \\ & \cdot (1 + q\beta\gamma A_{\mathrm{ro}})(1 + q\beta A_{q\beta})(1 + \beta\gamma A_{\beta\gamma}). \end{aligned} \tag{4.4}$$

This method can extract a physics asymmetry, A, at the same time as the detector asymmetries. N is the total signal yield, ϵ^{β} is the fraction of events with toroid polarity β. γ is the sign of the muon pseudo-rapidity (η) and q the sign of the muon

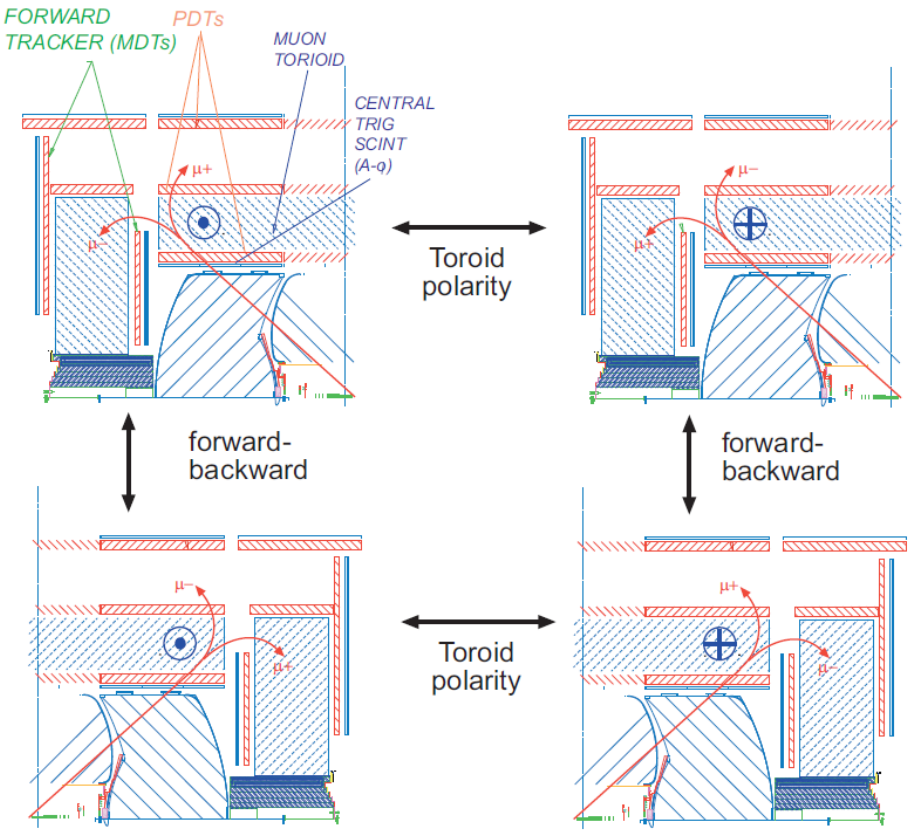

Figure 4.2: The range-out difference when the muon charge, toroid polarity or direction of flight changes [70].

charge. $n_q^{\beta\gamma}$ is then the signal yield for candidates with that combination of γ,β, and q. A is the physics asymmetry to be measured; $A_{\rm fb}$ is the forward-backward asymmetry; $A_{\rm det}$ is the detector asymmetry for particles emitted in the forward and backward directions; $A_{\rm ro}$ is the range-out asymmetry which takes into account the acceptance probability of muons bending towards or away from the beam line. $A_{q\beta}$ is the detector asymmetry governing the muon reconstruction efficiency when the toroid polarity changes and $A_{\beta\gamma}$ is the forwards-backwards asymmetry that remains after the toroid polarity flip.

4.3 Kaon Reconstruction Asymmetry

This section conveys the extraction of the charge asymmetry induced by interactions between kaons and the DØ detector. This is a background asymmetry to be subtracted from any physics asymmetry analysis with a solo charged kaon in the final state. What follows is a description of the extraction of this value, but the result given in Section 4.3.9 is not the final kaon correction used in the a_{sl}^{d} extraction. This is because an alternative channel was examined by others within the Lancaster HEPP Group [95] and found to give a result which is less contaminated by possible B decays and more inline with expectations from simulated data. This result is discussed in Section 4.3.10.

4.3.1 Motivation

When traversing the DØ detector, the charge of a kaon has a direct effect on the reconstruction efficiency of its track. This is due to positive and negative kaons having different inelastic interaction cross-sections with the material of the detector; a negative kaon ($s\overline{u}$) interacting with a proton or neutron can produce a hyperon resonance, whereas a positive one ($\overline{s}u$) cannot [94] due to the lack of valence anti-quarks. The result is a longer average path length for positively charged kaons, which leads to a greater reconstruction efficiency of K^{+} compared to K^{-}. A greater chance of reconstructing positive kaons plainly leads to a positive detector material induced asymmetry:

$$\sigma(K^{-}d_{\text{inelastic}}) > \sigma(K^{+}d_{\text{inelastic}}) \Rightarrow A_{raw} = \frac{N(K^{+}) - N(K^{-})}{N(K^{+}) + N(K^{-})} > 0. \qquad (4.5)$$

If the end state of a particle decay chain contains kaons that have a non-zero summed charge then this kaon asymmetry will alter the perceived charge asymmetry of the system. Thus it is important to understand and measure the inelastic cross-section kaon asymmetry in the DØ detector for studies into $\mathcal{CP}$ violation. To isolate kaon asymmetry, a decay process must be chosen where the physics charge

asymmetry is expected to be zero. As such, the rate of charm to strange quark decay is compared between the following and its charge conjugate:

$$D^{*+} \rightarrow D^0\pi^+,\ D^0 \rightarrow \mu^+K^-\nu_\mu, \tag{4.6}$$

where the D^* originates from quark hadronisation. D^0 oscillation is suppressed and their semi-leptonic decays are tree level single weak phase dominated, so no direct $\mathcal{CP}$ violation is expected. Thus, the only detectable asymmetry should be from the track reconstruction efficiencies. The asymmetry value, as related to Eqn 4.1, becomes

$$A_K = \frac{A_{raw} - A_\mu - A_{track}}{f_K}, \tag{4.7}$$

where the raw asymmetry (A_{raw}) is the difference between positive and negative kaons over the sum of all kaons (as per Eqn 4.5). The muon asymmetry, A_μ, is the asymmetry between the reconstruction of positive and negative muon tracks. The track asymmetry, A_{track}, is the same for the additional end state tracks. The latter two are backgrounds that need removing from the raw asymmetry. f_K is a dilution factor to take into account that not every reconstructed event is from the signal channel. Misidentifying pions as kaons reduces the measured asymmetry as there is no physics asymmetry expected from them.

An estimation of the pion reconstruction efficiency was conducted in the previous DØ extraction of the kaon reconstruction asymmetry [96], in which an upper limit was estimated to be $A_{\text{track max}} = 0.02\%$ [96]. This value was more recently extracted using a dedicated data driven tag and probe study of J/Ψ decays [97], and was found to be $A_{\text{track}} = 0.0030 \pm 0.0058\%$. As such, this value is considered negligible in this analysis.

The DØ detector is described in Section 3.2. As the single muon skimmed AADST data format is used, the subdetector sections used for this analysis are; the tracking systems (Sections 3.2.2 and 3.2.3), the muon detectors (Section 3.2.7),

and the magnets (Section 3.2.4 and 3.2.7). The polarities of the two magnets are regularly reversed so that each of the four polarity combinations are exposed to approximately equal integrated luminosity. This allows for the cancellation of first order detector asymmetries, as discussed in Section 4.2.

4.3.2 Event Selection

The events were selected from the full 10.4 fb^{-1} dataset that was collected during the RunII era of the DØ experiment. Muons were selected to have a transverse momentum greater than 2.0 GeV/c, a total momentum greater than 3.0 GeV/c, to have at least two axial hits in both the SMT and CFT portions of the detector along with at least one stereo hit in each. Also, the muons were required to have 'nseg' quality 3, which means that muon tracks require two hits in the central muon tracking layer, two hits across the outer two layers, and at least one scintillator hit associated with the track.

The D^0 candidate was constructed by pairing the muon track with another that was assigned the mass of a kaon. This kaon was required to have a transverse momentum greater than 0.7 GeV/c and at least two hits in both the SMT and CFT. As the contribution from the associated neutrino is unobtainable, a large mass window of $1.36 < m(\mu K) < 2.2$ GeV/c^2 was allowed. The lower mass constraint was chosen to suppress $D^0 \rightarrow K^*\mu\nu$ contamination [98]. This is desirable because $K^{*\pm}$ can decay into $K^0\pi^\pm$, where the charged pion track could be selected as that of the kaon. As the pion is not subject to the same reconstruction asymmetry as a kaon, the measured kaon asymmetry would be diluted. The upper $m(\mu K)$ constraint was chosen to allow the inclusion of the high mass sideband of the D^0 peak. Additionally, the D^0 candidate was required to have an angle between the direction of its momentum (as implied from the momenta of the kaon and muon candidates) and the direction from the primary vertex to the D^0 vertex in the transverse plain such to satisfy $\cos(\alpha_T^{D^0}) > 0.9$. This is to ensure that the D^0 comes from the primary vertex. The D^0 candidate track was reconstructed from

the muon-kaon vertex and momenta, and the D^* candidate which is mentioned below. This track required to fit the primary vertex such that it had a smaller significance than 4σ. A prompt $D^* \rightarrow D^0$ decay suppresses the probability of the D^* originating from an oscillated B meson decay, which could lead to additional charge asymmetry. 4σ was chosen to account for the missing neutrino introducing an uncertainty to the D^0 vertex reconstruction. The significance of the separation of the D^0 vertex and the primary vertex in the transverse plane had to satisfy $L_{xy}(D^0)/\sigma[L_{xy}(D^0)] > 3$ so that long-lived D^0 mesons were selected.

To construct the D^* candidate, a further track was added to the D^0 candidate and assigned a charged pion mass. This track also required at least two hits in both the SMT and CFT. To reduce combinatorial backgrounds from beauty decays, this pion track was required to fit the primary vertex with at least 3σ significance. This is done using the algorithm described in [99]. The invariant mass of the $\mu K\pi$ system was computed and required to produce a mass difference of $\Delta m = m(\mu K\pi) - m(\mu K) < 0.22$ GeV/c^2. This limit was chosen to give complete acceptance to the peak centred on the pion mass and to give a wide sideband region with which to constrain the background shape and extrapolate the combinatorial background beneath the resonance.

The event selection cuts are summarised in Table 4.1

Cut	Notes
	μ
$p_T > 2.0$ GeV/c	Transverse momentum
$p > 3.0$ GeV/c	Total momentum
>= 2 SMT axial hits	Silicon Microstrip Tracker
>= 1 SMT stereo hits	
>= 2 CFT axial hits	Central Fiber Tracker
>= 1 CFT stereo hits	
	$D^0(\mu K)$ candidate
$1.36 < m < 2.2$ GeV/c^2	Reconstructed mass
$\cos(\alpha_T^{D^0}) > 0.9$	Angle between D^0 momentum and spatial vector from primary vertex to D^0 vertex in transverse plane
$S_{D^0} < 16$	Combined significance of D^0 track with respect to primary vertex
$L_{xy}(D^0)/\sigma[L_{xy}(D^0)] > 3$	Distance to primary vertex in transverse plane
	K
$p_T > 0.7$ GeV/c	Transverse momentum
>= 2 SMT	
>= 2 CFT	
	π
$S_\pi < 9$	Combined significance of π track with respect to primary vertex
>= 2 SMT	
>= 2 CFT	
	$D^0(\mu K)$ candidate
$\Delta m < 0.22$ GeV/c^2	$\Delta m = m(\mu K\pi) - m(\mu K)$

Table 4.1: Table of event selection cuts.

4.3.3 Signal Extraction

The mass distributions for the D^0 candidate and the mass difference distribution without requiring charge correlations is the black line in Fig. 4.3. The D^0 peak is smeared due to the missing neutrino energy, whereas the peak in the Δm mass difference plot is plain to see. This is due to the neutrino energy loss being cancelled, which affects both $m(\mu K)$ and $m(\mu K\pi)$. The signal candidates are chosen from those that match the correct sign topology of the D^* decay. Thus to be considered signal, we require,

$$\begin{aligned} q_\mu \cdot q_K &< 0 \\ q_\mu \cdot q_\pi &> 0 \end{aligned} \tag{4.8}$$

The resonance is centred within close proximity to the kinematic threshold, the Δm distribution has no lower-mass sideband. Due to this, a wrong-sign background sample is required to model the behaviour of the combinatorial background beneath the signal region. There are three choices available:

$$\text{BG 1: } q_\mu \cdot q_K > 0 \tag{4.9a}$$

$$\text{BG 2: } q_\mu \cdot q_K > 0,\ q_\mu \cdot q_\pi < 0 \tag{4.9b}$$

$$\text{BG 3: } q_\mu \cdot q_K > 0,\ q_\mu \cdot q_\pi > 0 \tag{4.9c}$$

The background as described by Eqn 4.9c should have the least signal type contamination as there are no physical processes which can result in the three measurable final states having the same charge. The following paragraphs describe the test of this assumption, and continuation of the description of the signal extraction method follows.

Wrong sign choice: From the D^0 candidate, the non-muon track was assigned a pion mass. The mass of the candidate, $m(\pi\mu)$, was recalculated, which was then used to build the Δm mass distribution. To pick a region where the D^0 signal

is kinematically suppressed, both the region of $[2.1 < m(\pi K) < 2.2]$ GeV/c^2 and the region of $m(\mu\pi) > 2.1$ GeV/c^2 were required. This Δm is constructed for the right-sign combination in Eqn 4.8 and the three wrong-sign choices, Eqns 4.9a, 4.9b and 4.9c. These histograms, along with the ratio between right-sign and wrong-sign distributions, are shown in Fig. 4.4.

As can be seen from Fig. 4.4, the background choice using Eqn 4.9c gives the most level background comparison and the least structure in the signal mass region. The unwanted physics effect contributing to sample using Eqn 4.9b also affects Eqn 4.9a, so it is plain to see that the charge correlation in Eqn 4.9c is the best choice for combinatorial background estimation. As such, this is the choice used for 'wrong-sign' candidates from this point onwards. The $m(\mu K)$ distribution using these correlations can be seen in Fig. 4.3. The shape of the wrong-sign background under the signal was tested by constructing a mass distribution from the 20K single inclusive muon Monte-Carlo sample that a D^* was reconstructed from whilst vetoing all events that contained a signal producing process listed in Table 4.6. The shape was normalised to unit area and was compared to the normalised wrong-sign background plot made from the data sample. This is shown in Fig. 4.5. A Kolmogorov-Smirnov test produced a likelihood of source value of 0.79, justifying the decision to use the charge correlation in Eqn 4.9c as a measure of combinatorial background.

Background handling: Having chosen an appropriate wrong-charge background sample, the signal region could now be investigated. The range of $m(\mu K)$ was changed to focus on the D^0 candidate mass peak, $1.36 < m(\mu K) < 1.9$ GeV/c^2. Using this constraint, the right-sign distribution using charge requirements in Eqn 4.8 is denoted $f_{\rm sig}(\Delta m)$. Conversely, the wrong-sign background subsample by $f_{\rm bkg}(\Delta m)$.

Because of the missing neutrino, accurately describing the shape of the signal structure for different ranges of $m(\mu K)$ becomes difficult due to the smearing caused by the missing energy. To compensate for this, the sample is divided

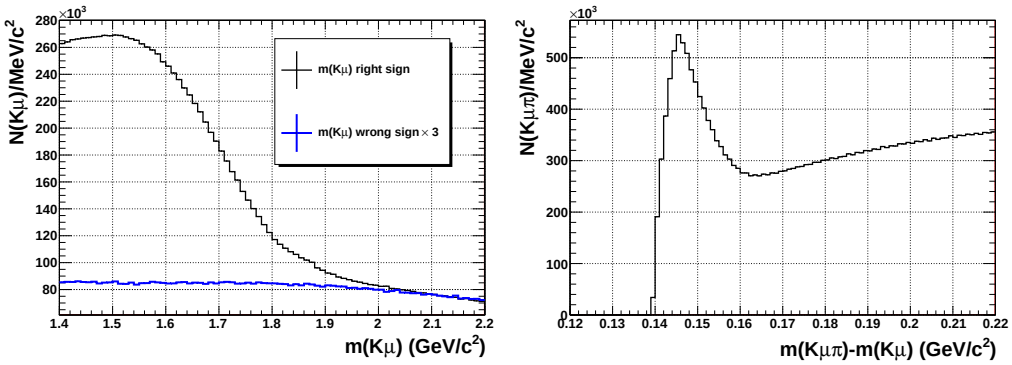

Figure 4.3: Left: m(μK) for right-sign (black) and wrong-sign correlation ($\times 3$) (blue). Right: m($\mu K\pi$) - m(μK) right-sign. The D^0 candidate peak that is formed in the left plot is very wide due to the missing neutrino energy, whereas the mass difference peak is much narrower. The right-sign correlation is described in Eqn 4.8 and the wrong-sign in Eqn 4.9c

into six $m(\mu K)$ ranges of 100 MeV/c^2 between 1.3 GeV/c^2 to 1.9 GeV/c^2. The signal shape is still non-trivial, so the method used to extract the signal count was background modelling and subtraction rather than signal shape fitting. This was done using two methods; sideband scaled wrong-sign subtraction and background fitting. The former was used in the previous kaon asymmetry search [96] and also to define the signal region for the sample. The latter was a method tested to reduce the effects of fluctuation in low statistics subsamples. This will be discussed later.

Assuming that the shape of the combinatorial background in the right-sign Δm distribution has the same shape as the wrong-sign counterpart, the ratio of events in each sample should be the same when examining both the resonance region of (0.139 GeV/c^2 $< \Delta m < \Delta m_{\rm cut}$) and the sideband region of ($0.19 < \Delta m < 0.22$) GeV/c^2. $\Delta m_{\rm cut}$ is a value to be found which constrains the signal area which gives the greatest significance, $Sig = \sqrt{\text{signal/signal+background}}$. The ratios would then give

$$\frac{B}{N_{ws}^{\rm sig}} = \frac{N_{rs}^{\rm side}}{N_{ws}^{\rm side}}, \tag{4.10}$$

where B is the combinatorial background contribution in the signal region of the right-signed sample. $N_{rs}^{\rm sig}$ is the total number of candidates within the signal

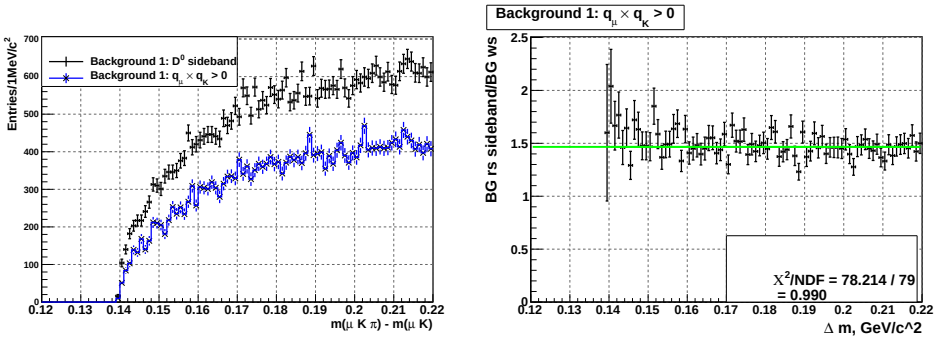

(a) BG1

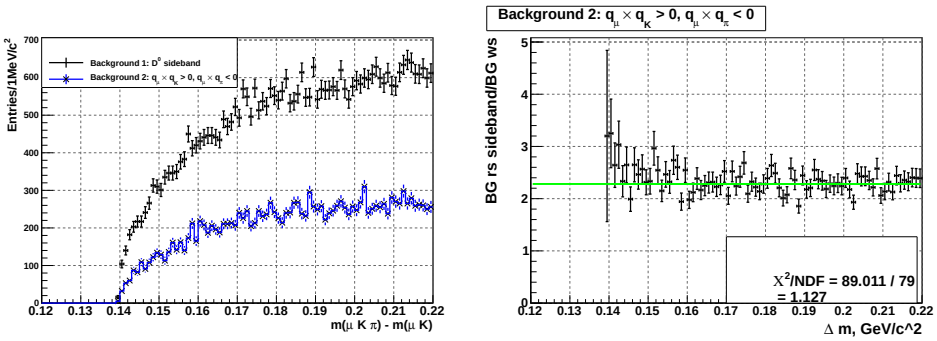

(b) BG2

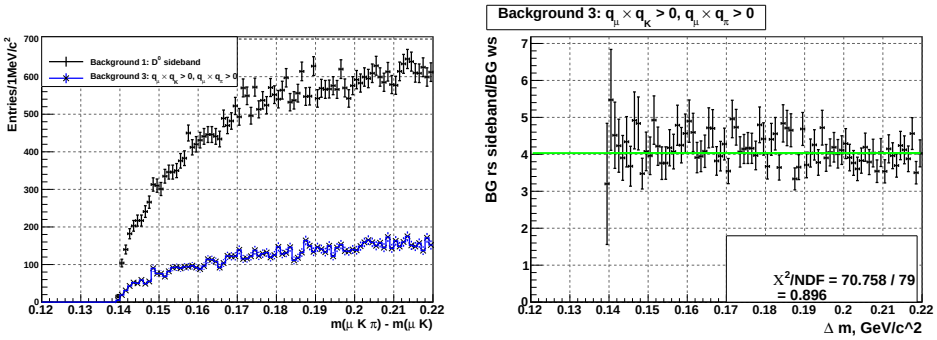

(c) BG3

Figure 4.4: An examination of the wrong-sign charge correlation possibilities. On the left are plots for the Δm distributions for the μK sideband mass > 2.1 GeV/c^2 against the various wrong-sign possibilities as described in Eqns 4.9a,4.9b, and 4.9c. On the right are the plots for the sideband distribution divided by the wrong-sign distribution. BG1 and BG2 have a slight peaking structure in the mass difference signal region, whereas BG3 does not. This is due to the impossibility of having a signal effect from three like-charged end state particles.

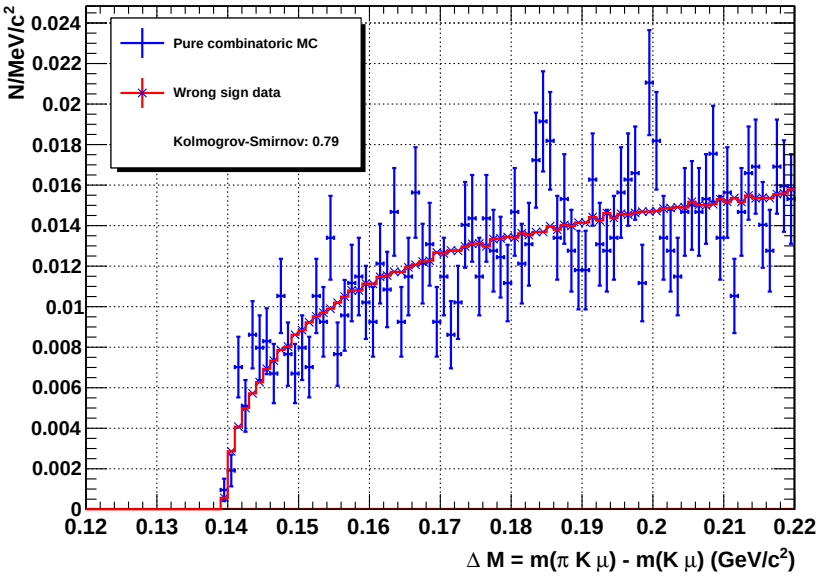

Figure 4.5: From 20k single inclusive muon Monte-Carlo events, a distribution was constructed from all passing candidates that did not have a D^0 decay which contributes to the signal (all decays listed in Table 4.6). This distribution was normalised to unit area and compared to a normalised distribution of the wrong-sign charge correlated background from Eqn 4.9c. The resulting Kolmogorov-Smirnov value was 0.79, confirming that this charge correlation choice reflected the combinatorial background shape well.

$m(\mu K)$ region (GeV/c^2)	Best $m(\mu K\pi) - m(\mu K)$ cut (GeV/c^2)
1.3 – 1.4	0.1655
1.4 – 1.5	0.1605
1.5 – 1.6	0.1565
1.6 – 1.7	0.1535
1.7 – 1.8	0.1515
1.8 – 1.9	0.1495

Table 4.2: The cutoff mass difference values that provides a signal yield with the greatest significance for a given $D^0(\mu K)$ candidate mass range.

region which fulfill the right-sign requirements, N_{rs}^{side} is the number of right-sign candidates in the sideband, and N_{ws}^{sig} and N_{ws}^{side} are the wrong-sign equivalents of the same regions. The number of combinatorial background events in the sample can be defined as

$$B = N_{ws}^{\text{sig}} \cdot \frac{N_{rs}^{\text{side}}}{N_{ws}^{\text{side}}} \tag{4.11}$$

and the number of signal candidates is,

$$S = N_{rs}^{sig} - B. \tag{4.12}$$

Using this method, Δm_{cut} is investigated for each of the $m(\mu K)$ regions. It is seen that with increasing D^0 candidate mass, Δm_{cut} decreases to reflect the narrower peak. See Fig. 4.6 and Table 4.2 for the results. To find the total number of signal and background candidates under the mass difference peak, one must simply sum across the counts from the $m(\mu K)$ split samples using the individually defined signal region in each:

$$\begin{aligned} S_{\text{total}} &= \sum_i S_i \\ B_{\text{total}} &= \sum_i B_i, \end{aligned} \tag{4.13}$$

where i is the i^{th} $m(\mu K)$ bin.

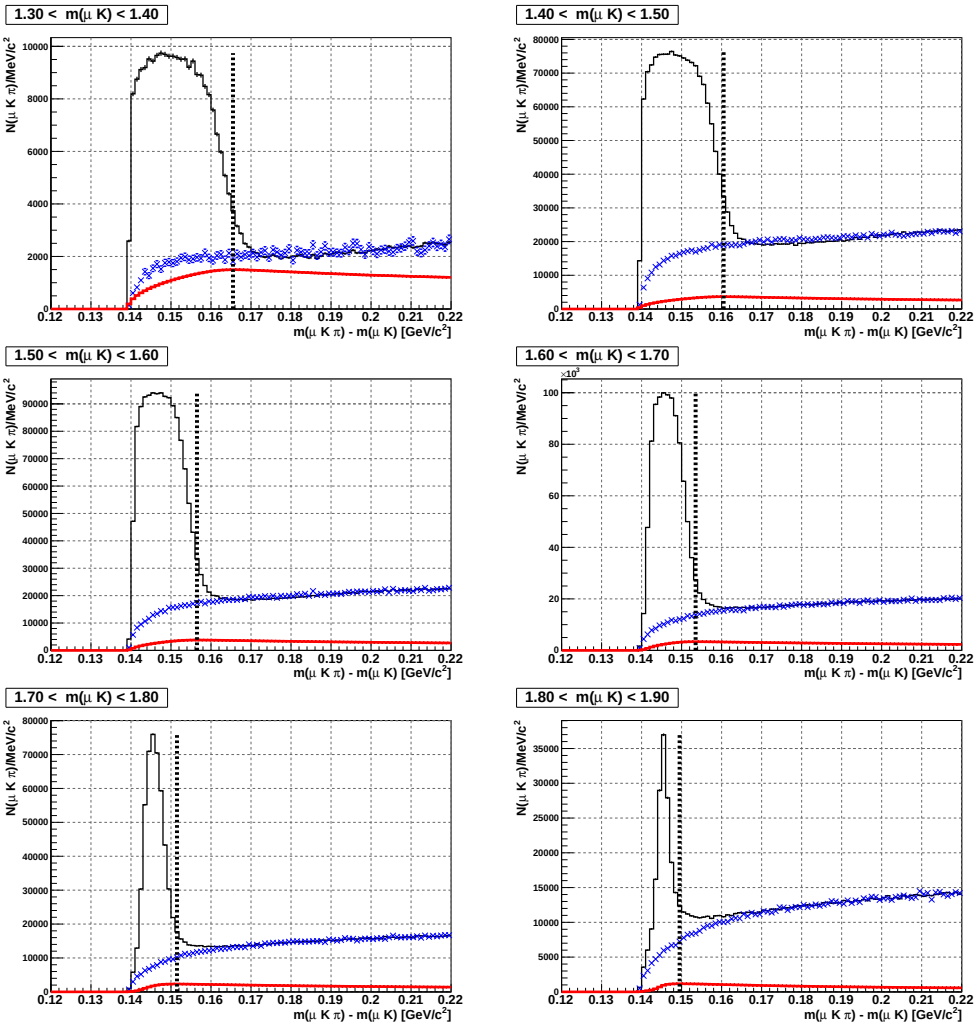

Figure 4.6: Finding the mass difference cut value to maximise the significance of the extracted yield. The points with the crosses are the wrong-sign correlated candidates as described by Eqn 4.9c. The solid black lines are the right-sign correlated candidates. The solid red line shows the significance of the yield scaled up by 4 for a cutoff at that mass difference, $S/\sqrt{S+B}$ where S and B are given in Eqns 4.11 and 4.12. The dashed line shows the mass difference with the greatest significance yield. These values can be found in Table 4.2.

4.3.4 Analysis Method

The kaon charge asymmetry is measured using the charge of the associated muon. Since $q_\mu \cdot q_K < 0$, the asymmetry found by measuring the muon should be opposite to that of the kaon, i.e. negative.

The cross-sectional difference in the physics of the kaon is not the only source of detectable charge asymmetry; additional physics and detector sources of asymmetry between the muons of different charge must be negated first. Regions of the detector can have differing reconstruction efficiencies for differently charged particles in the same area, leading to global and local charge asymmetries as discussed in Section 4.2. The weighting method discussed in that section was applied to negate this. The entire sample was examined in bins of total kaon momentum on a candidate by candidate basis, counting events which fall beneath the ΔM cutoff for their respective $m(\mu K)$ value for each polarity combination of the toroidal and solenoidal magnets. From these counts, the weight for each candidate was found by dividing the total yield of the smallest sample by the yield for that candidate's corresponding polarity combination. The weights can be seen in Table 4.3. The raw kaon asymmetry extraction method (using Eqn 4.4) that was used in previous kaon asymmetry analysis at DØ[96] is investigated in Section 4.3.8 as a source of systematic uncertainty.

For each $m(\mu K)$ region, four Δm distributions were constructed:

- Right-signed, positive muon (r_+)
- Right-signed, negative muon (r_-)
- Right-signed, either charge (r_c)
- Wrong-signed, either charge (w_c)

Each entry was weighted according to Table 4.3. A difference plot is constructed by performing the subtraction r_- - r_+. The yield found by integrating the resulting distribution up to Δm_{cut} corresponds to $N(K^+) - N(K^-)$. To account for the

p(K) (GeV/c)	0.70 → 1.70	1.70 → 2.40	2.40 → 3.20	3.20 → 4.20	4.20 → 5.50	5.50 → 7.50	7.50 → 11.50	> 11.50
$N_{(+1,+1)}$	146136	140414	140271	143639	138363	136424	129622	103253
$N_{(+1,-1)}$	151325	143065	143490	146869	140656	141014	133391	105958
$N_{(-1,+1)}$	156515	147843	149051	151386	146606	144210	136076	109666
$N_{(-1,-1)}$	155873	147770	148566	151992	146221	144377	136688	108977
$w_{(+1,+1)}$	1.000	1.000	1.000	1.000	1.000	1.000	1.000	1.000
$w_{(+1,-1)}$	0.966	0.981	0.978	0.978	0.984	0.967	0.972	0.974
$w_{(-1,+1)}$	0.934	0.950	0.941	0.949	0.944	0.946	0.953	0.942
$w_{(-1,-1)}$	0.938	0.950	0.944	0.945	0.946	0.945	0.948	0.947

Table 4.3: The total right-sign event count N for the charge combination of the toroidal and solenoidal magnet polarities $(\pm 1, \pm 1)$ per kaon momentum region, and the weights w each event was to be weighted by according to these counts as per Eqn 4.34. Each combination then gives equal contribution to the sample, allowing first order detector asymmetries to be subtracted. Although it is expected that the weighting should not be very dependent on kaon momentum, and it is shown above that it is not, the weights were still calculated in these regions. This is due to a kaon momentum dependence on the kaon asymmetry, so the full detector correction was required for the extraction of asymmetry in each $p(K)$ bin.

combinatorial background shape in the difference histogram, a background value is constructed and subtracted. The sideband scaled wrong sign contribution is found using w_c scaled by the ratio of the sidebands between the difference histogram and w_c. This histogram is integrated to the same Δm_{cut} value, where the resulting value is subtracted from the difference plot yield. This can be described in terms of Eqn 4.11 and 4.12 as

$$N_{\text{diff}} = N_{rs}^{\text{sig}}(K^+ - K^-) - \left(\frac{N_{rs}^{\text{side}}}{N_{ws}^{\text{side}}} N_{ws}^{\text{sig}}\right)(K^+) - (K^-) \tag{4.14}$$

$$= \sum_i \int_{m_{\pi^\pm}}^{\Delta m_{\text{cut}\,i}} (r_- - r_+)_i d\Delta m - \frac{\int_{0.19\ \text{GeV/c}^2}^{0.22\ \text{GeV/c}^2} (r_- - r_+)_i d\Delta m}{\int_{0.19\ \text{GeV/c}^2}^{0.22\ \text{GeV/c}^2} w_{ci} d\Delta m} \int_{m_{\pi^\pm}}^{\Delta m_{\text{cut}\,i}} (w_{ci}) d\Delta m, \tag{4.15}$$

where i is the i^{th} $m(\mu K)$ bin and N_{diff} is the signal yield of the difference plot, and $m_{\pi^\pm}$ is the mass of a charged pion.The total signal yield was found for the subsample by using the same with r_c instead of $r_- - r_+$, along with w_c,

$$N_{\text{total}} = N_{rs}^{\text{sig}}(K^\pm) - \left(\frac{N_{rs}^{\text{side}}}{N_{ws}^{\text{side}}} N_{ws}^{\text{sig}}\right)(K^\pm) \tag{4.16}$$

$$= \sum_i \int_{m_{\pi^\pm}}^{\Delta m_{\text{cut}\,i}} (r_c)_i d\Delta m - \frac{\int_{0.19\ \text{GeV/c}^2}^{0.22\ \text{GeV/c}^2} (r_c)_i d\Delta m}{\int_{0.19\ \text{GeV/c}^2}^{0.22\ \text{GeV/c}^2} w_{ci} d\Delta m} \int_{m_{\pi^\pm}}^{\Delta m_{\text{cut}\,i}} (w_{ci}) d\Delta m. \tag{4.17}$$

The difference and combined yields for each $m(\mu K)$ subsample are summed as per Eqn 4.13. The raw asymmetry for the sample was calculated as per Eqn 4.5. This process will be referred to as the "weighted difference method".

For a comparison of the sensitivities between these two methods, see Section 4.3.5. An alternative method of extracting the signal yield using fitting was tested as a source of systematic uncertainty, and is described in Section 4.3.8.

4.3.5 Sensitivity

To give an indication of the statistical uncertainty that can be expected from this analysis, the dataset was run over many times with randomly assigned muon

charge each time. This should give a central asymmetry value of zero plus or minus a small value based on statistical fluctuation. If this process is repeated many times, a distribution can be constructed from the extracted asymmetries. If the individual differences from zero are purely statistical, then this distribution should be Gaussian in nature. The mean of the Gaussian reflects a bias and the width gives us the sensitivity. In Fig. 4.7 the system eight and weighted difference methods are tested in this manner. It can be seen that the weighted difference method has a finer sensitivity value of 0.057%, compared to 0.109% for system eight, and thus should be used to gain a final result with the smallest statistical uncertainty.

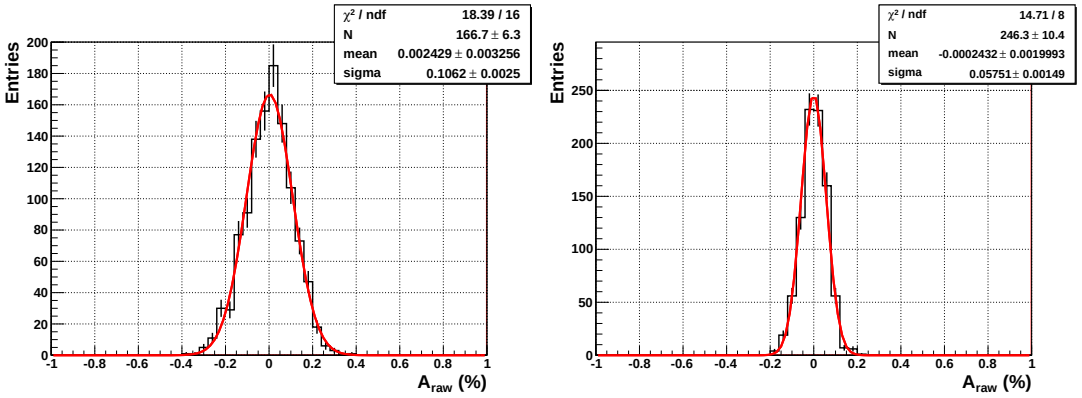

Figure 4.7: A comparison of the statistical sensitivity of extracting the charge asymmetry using the old system 8 method (left) and the newer weighted difference method (right). These plots are produced by running the asymmetry extraction program many times whilst randomising the muon charge for every candidate, making the effective charge asymmetry zero. By building a distribution of the extracted asymmetries it is possible to see bias by fitting a Gaussian and comparing the mean to zero. The expected statistical uncertainty of the method is found by looking at the sigma of the fitted Gaussian. It is clear that the weighted difference method has a better expected statistical uncertainty.

4.3.6 Yield Extraction

The extraction of N_{total} and N_{diff} for $m(\mu K)$ regions using the sideband scaled wrong-sign subtraction can be seen in Fig. 4.8. Yield results are in Table 4.4. These yields are in bins of kaon total momentum for reasons that are described in

Section 4.3.7. The yields of the former using a fitted background can be seen in Section 4.3.8.

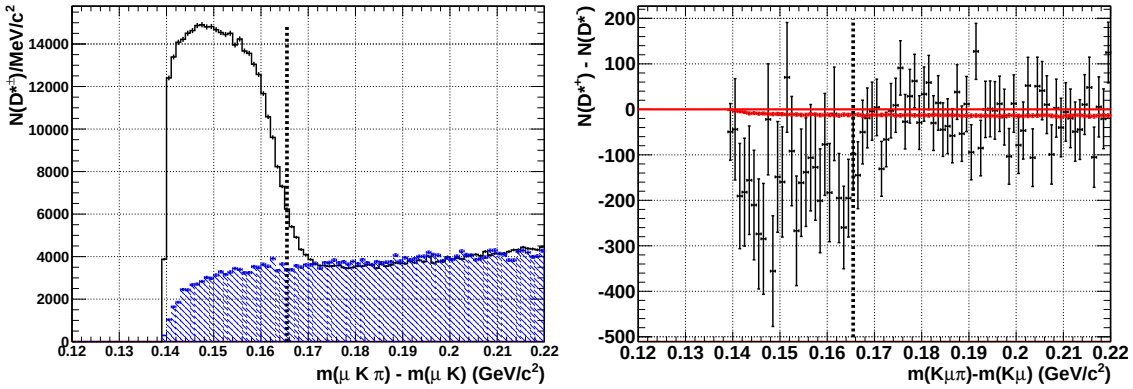

(a) $1.3 < m(\mu K)/\mathrm{GeV/c^2} < 1.4$

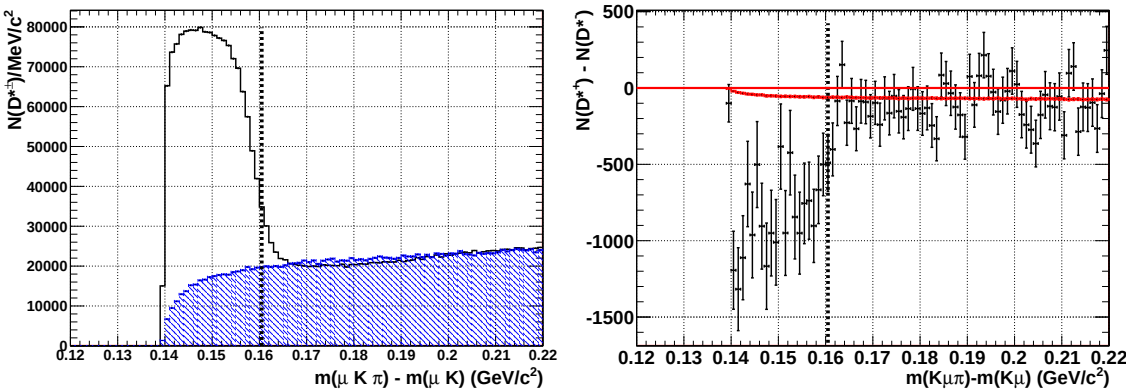

(b) $1.4 < m(\mu K)/\mathrm{GeV/c^2} < 1.5$

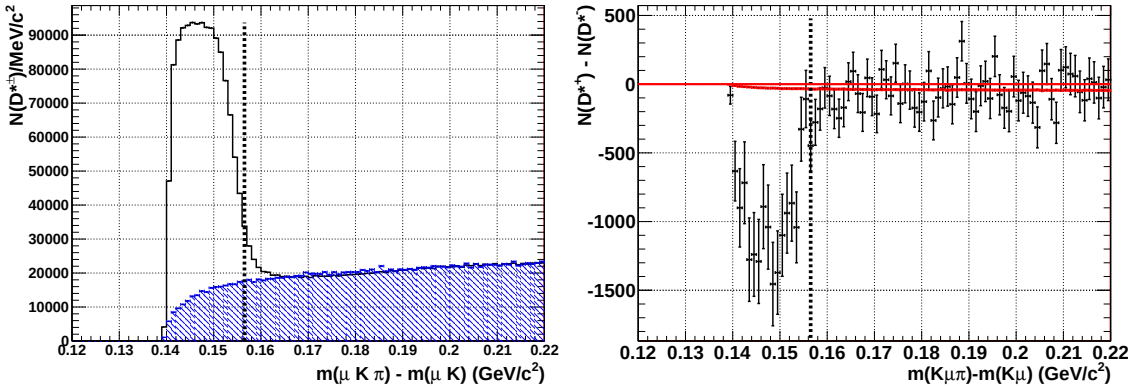

(c) $1.5 < m(\mu K)/\mathrm{GeV/c^2} < 1.6$

Figure 4.8

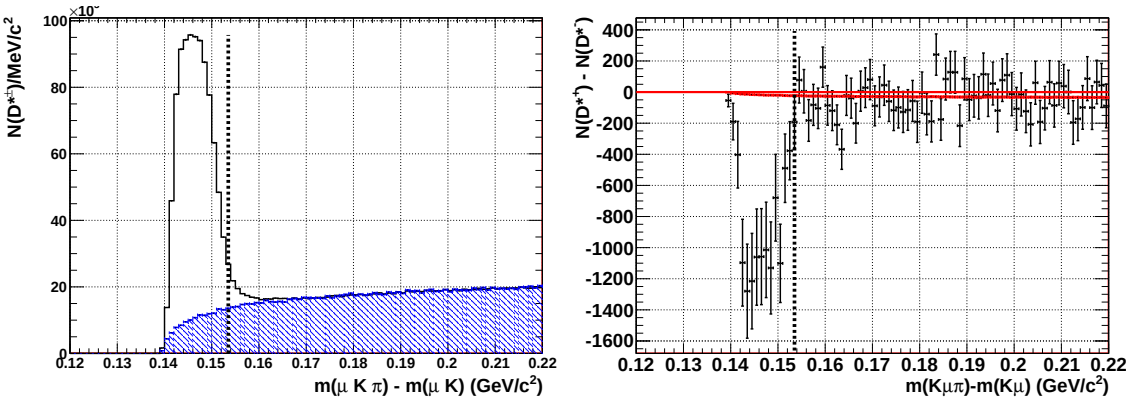

(d) $1.6 < m(\mu K)/\mathrm{GeV/c^2} < 1.7$

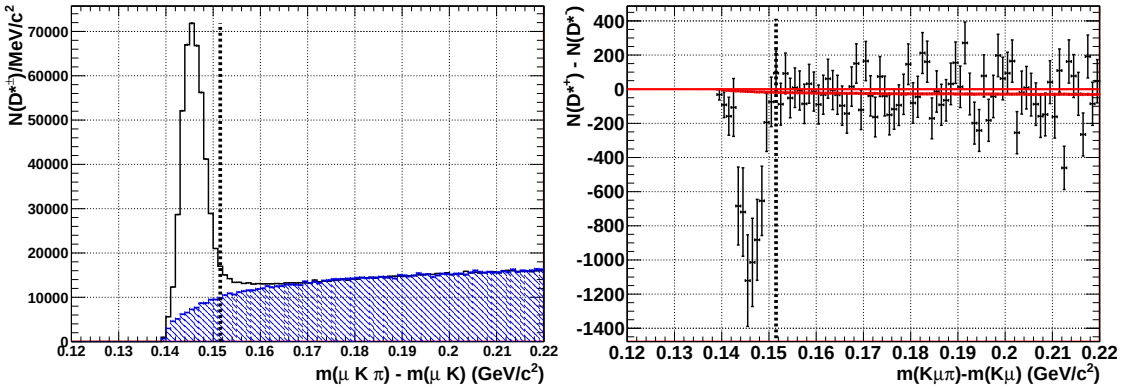

(e) $1.7 < m(\mu K)/\mathrm{GeV/c^2} < 1.8$

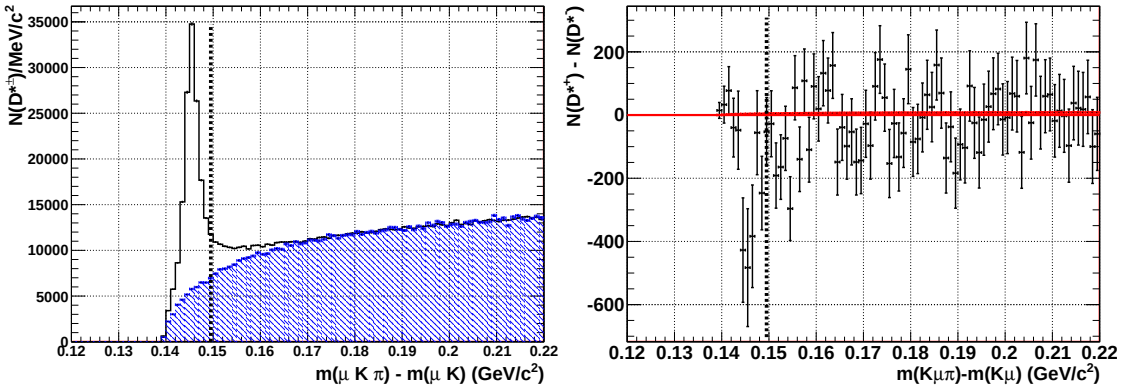

(f) $1.8 < m(\mu K)/\mathrm{GeV/c^2} < 1.9$

Figure 4.8: continued - Signal extraction for single momentum bin of $p(K) > 0.7$ GeV/c for the six $m(\mu K)$ regions. Left: N_{total} extraction by sideband scaled background subtraction. Right: -1×N_{diff}. The total signal yield is approximately 3.45M. The hashed histogram shows the sideband scaled wrong-sign distribution. The other histogram is the right-sign distribution. The dashed line shows the significance cutoff value for that $m(\mu K)$ range. The solid red line on the difference histograms is set at $N_{\mathrm{diff}} = 0$, and the red histogram shows the sideband scaled wrong sign combinatorial contribution.

p(K) range (GeV/c)	N($D^{*\pm}$)	N(K^+) - N(K^-)
0.7 – 1.7	375289 ± 1353	8251.3 ± 794.7
1.7 – 2.4	437012 ± 1307	7714.7 ± 781.0
2.4 – 3.2	472879 ± 1299	7083.3 ± 781.0
3.2 – 4.2	512974 ± 1310	6158.9 ± 791.0
4.2 – 5.5	514952 ± 1318	6898.3 ± 778.9
5.5 – 7.5	529594 ± 1405	7061.8 ± 783.2
7.5 – 11.5	539683 ± 1513	6706.0 ± 784.9
> 11.5	508068 ± 1581	5582.5 ± 754.9

Table 4.4: Signal and difference yields per kaon momentum region.

4.3.7 Raw Asymmetry Result

Using the weighted difference method, the raw kaon asymmetry for the entire sample was be extracted as (1.437±0.058 (stat))%. Note that the extracted uncertainty is consistent with the expectations of the sensitivity test. This shows an increase in precison from the previous raw asymmetry result which was (1.31 ± 0.09%). However, this is not the final result. As stated in Eqn 4.7, the reconstruction asymmetry for muons must be addressed. The track asymmetry has been predicted to be negligible as mentioned in the first section. A study was undertaken to extract the muon reconstruction asymmetry per kaon momentum region using a tag and probe study of J/Ψ to dimuon decays. An asymmetry is found between a muon passing muon quality cuts when the antimuon does not and vice versa. This asymmetry is muon p_T dependent, so each $p(K)$ subsample was split into six $p_T(\mu)$ regions. The resulting asymmetries were convoluted with the occupancy of signal yield per region. The description of this asymmetry extraction can be found in a DØ Note [100]. The results can be seen in Table 4.5. These numbers can be directly subtracted from the raw kaon charge asymmetries, where the resulting value would represent the numerator of Eqn 4.7.

p(K) range (GeV/c)	A_μ %
0.7 – 1.7	0.184 ± 0.025 (stat) ± 0.044 (syst)
1.7 – 2.4	0.172 ± 0.024 (stat) ± 0.043 (syst)
2.4 – 3.2	0.166 ± 0.024 (stat) ± 0.044 (syst)
3.2 – 4.2	0.162 ± 0.024 (stat) ± 0.044 (syst)
4.2 – 5.5	0.156 ± 0.024 (stat) ± 0.045 (syst)
5.5 – 7.5	0.151 ± 0.024 (stat) ± 0.046 (syst)
7.5 – 11.5	0.176 ± 0.023 (stat) ± 0.063 (syst)
> 11.5	0.130 ± 0.025 (stat) ± 0.045 (syst)

Table 4.5: The muon charge asymmetry per kaon momentum region [100].

4.3.8 Systematics

Dilution

As per Eqn 4.7, the sample composition must be dealt with to find the final values of momentum dependent kaon asymmetry. The raw asymmetry is equivalent to $A = f_K A_K + f_\pi A_\pi$, where f_K is the fraction of modes with a real charged kaon in the final state and f_π is the fraction of modes with a pion in the final state that have been misidentified as a kaon. The cross-sections of positively and negatively charged pions when interacting with the detector material should be roughly equal over the experimentally measured range of momenta [94], so the pion physics asymmetry, A_π, was assumed to be negligible [98]. Thus, the corrected Kaon asymmetry $A_K = A/f_K$, meaning the dilution factor is the fraction of candidates with a final state charged kaon. Table 4.6 shows the contributing D^0 decay modes and their branching fractions as found on the Particle Data Group website [101]. Channels 1 and 2 are signal modes as they have charged final state kaons. Channels 3, 4, and 5 feature charged pions in their final state, which contribute to the background if mis-identified as kaons. Channels 2 and 5 have an additional reconstruction efficiency to take into account due to their intermediate states. To find this efficiency, the analysis code was executed over a sample of 20k single inclusive muon Monte-Carlo events that have a $D^* \to D^0 X$ candidate in them. 92 candidates were reconstructed out of 369 true decays for channel 2 and 29 candidates were reconstructed from 114 decays for channel 5. This gives

No	D^0 Decay Channel	Br(%)	Reco Eff (%)
1	$\mu^+K^-\nu$	3.30 ± 0.13	
2	$\mu^+K^{*-}(K^-\pi^0)\nu$	0.63 ± 0.08*	25 ± 3
3	$\mu^+K^{*-}(K^0\pi^-)\nu$	see text	
4	$\mu^+\pi^-\nu$	0.24 ± 0.02	
5	$\mu^+\rho^-(\pi^-\pi^0)\nu$	0.19 ± 0.04	25 ± 5

Table 4.6: The contributing D^0 decay modes which contribute to the μK signal candidates. There is an additional reconstruction efficiency for the modes which involve final state pions that come from a secondary decay. The reconstruction efficiencies are found by comparing generated and reconstructed numbers for each type in a generic single inclusive muon Monte-Carlo sample. Channels 1 and 2 have real charged kaon final states, and so contribute to the kaon asymmetry. Channels 3 to 5 have pions mis-identified as kaons in the final state, and so contribute to the dilution of the measured kaon asymmetry.
*Channel No 2 has a branching ratio of 1/3×BR($\mu^+K^{*-}\nu$)

reconstruction efficiencies of (25 ± 3)% and (25 ± 5)% respectively. The values agree with each other as expected. The reconstruction efficiency of these modes was set at a slightly conservative (25±3)% due to the small statistics, unmeasured systematics associated with this measurement, and because the dilution fraction is not very sensitive to this reconstruction efficiency and its uncertainty.

Channel 3 is a special case in that the final state pion can be misidentified as a kaon, making it difficult to distinguish the signal and background contribution of K^* decays in flight. This channel is kinematically suppressed for $m(\mu K) > 1.2$ GeV/c^2 and is rarely seen for $m(\mu K) > 1.36$ GeV/c^2. The few remaining $K^{*\pm} \rightarrow K^0\pi^\pm$ decays act as a dilution to the sample. To find this dilution, $K^{*\pm} \rightarrow K^0\pi^\pm$, $K^0 \rightarrow K_S \rightarrow \pi^+\pi^-$ candidates are reconstructed from the full data sample, which corresponds to approximately 3.45M D* signal candidates. From the remaining tracks in the events, two with opposite charge are chosen that form a vertex. The mass of a pion was assigned to each track, and the invariant mass window of $0.460 < m(\pi\pi) < 0.525$ GeV/c^2 was cut on. These two pions formed the K_S candidate, whose trajectory was assumed to pass through the K_S decay vertex and be directed along the reconstructed momentum of the two-pion system. Next, the kaon candidate from the regular part of the analysis

was assigned a pion mass and combined with the K_S candidate. Thus, the mass of the $K^* \to K_S\pi$ is calculated. After fitting with a Gaussian with a third degree polynomial background, 2k signal candidates are extracted from the 3.45M D^* containing sample. This can be seen in Fig. 4.9. Taking into account that the fraction of K_S in K^0 is 0.5, the branching ratio of $K_S^0 \to \pi\pi = 0.69$ [101] and the reconstruction efficiency of $\pi\pi$ in the DØ detector is 0.30 [46], the total contamination is of the order 0.55%. This was assigned a conservative uncertainty of ± 0.55 %. Taking into account this contamination and the uncertainty of the reconstruction efficiencies of channels 2 and 5, the fraction of signal kaons in the sample was found to be $f_K = 0.918 \pm 0.006$. This results in a central value for the kaon asymmetry of $A_K = [(1.437 \pm 0.058)\ \% - A_\mu]/(0.918 \pm 0.006) = (1.724 \pm 0.080)\ \%$. A_μ is subtracted per $p(K)$ region as described in Table 4.5. By altering the reconstruction efficiencies of channels 2 and 5 by $\pm 3\%$ and by altering the K^* contamination by $\pm 0.55\%$, a systematic change in final asymmetry was observed by a factor $\Delta A_K = 0.010\%$.

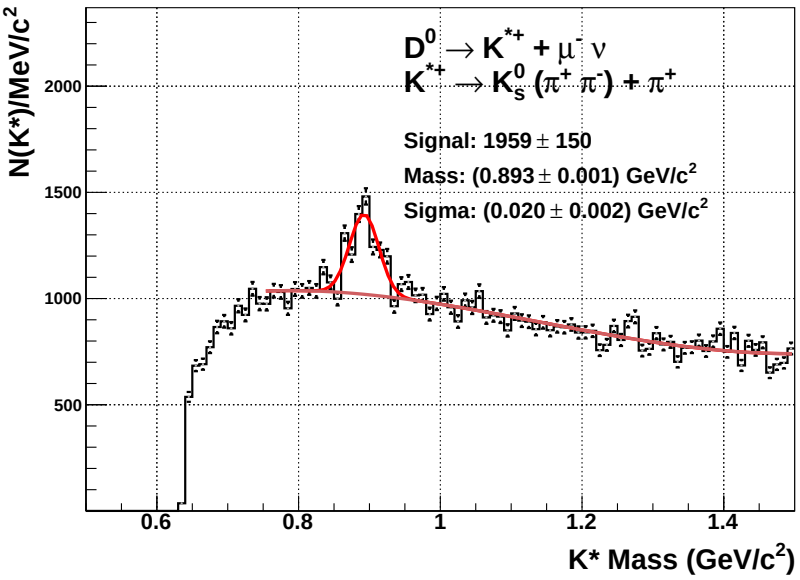

Figure 4.9: Reconstructed $K^*\pi$ mass distribution where the pion is misidentified as a kaon. This is produced from a sample which contains ∼3.5M signal candidates. The fit function is a single Gaussian signal plus third degree polynomial background.

Other Systematics

Asymmetry extraction method The asymmetry extraction method which was used in the previous kaon asymmetry analysis [70], known as 'system eight', was to split each sample into eight histograms of toroid polarity, muon charge and muon pseudo-rapidity sign combinations. It is shown in Eqn 4.4 and is described in [93]. Although more background asymmetry values can be extracted using this method, the correlated uncertainties of the detector asymmetries, extracted by a χ^2 minimising algorithm, adds to the uncertainty of the raw asymmetry. Due to this reason, the event reweighting method was preferred.

Alternative Combined Yield Method An alternative method of extracting the total signal yield for any subsample was to fit the background within the signal region and subtract that yield from the integration of the right-sign histogram up to the signal cutoff. With this method, the background need not be restricted to being the scaled wrong-sign histogram. The fewer entries a wrong sign histogram has, the larger the statistical fluctuation the distribution will display. A hybrid background was constructed from the wrong-sign scaled histogram below a cutoff and the right-sign histogram sideband above it. This cutoff was chosen to be 0.010 GeV/c^2 above the $m(\mu K)$ significance cutoff to be sure no signal structure entered the sideband portion of the hybrid background histogram. This method reduced the statistical fluctuations in the sideband and gave a stronger anchor for the fitting function in that region. A hyperbolic tangent function added to a straight line was normalised between the function turn on and the significance cutoff point and fit to the distribution with Minuit [103]. This fit can be seen in Fig. 4.10.

Using this method to extract the combined sample signal yields heralded a raw asymmetry value of $(1.437 \pm 0.058)\%$, which is exactly the same central value and uncertainty as with the regular sideband scaled wrong-sign method. As such, the method of counting the background yields has lead to no measurable systematic uncertainty.

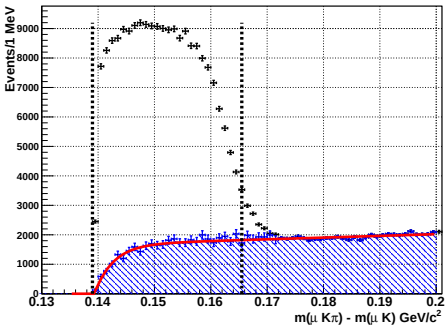

(a) $1.3 < m(\mu K)/\mathrm{GeV/c^2} < 1.4$

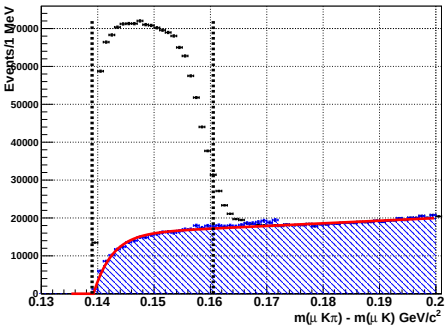

(b) $1.4 < m(\mu K)/\mathrm{GeV/c^2} < 1.5$

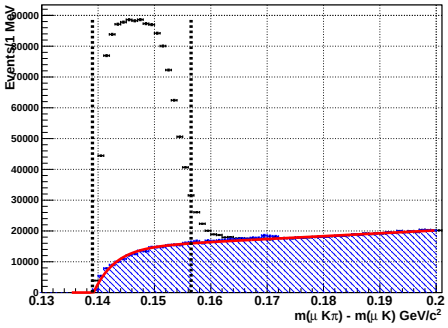

(c) $1.5 < m(\mu K)/\mathrm{GeV/c^2} < 1.6$

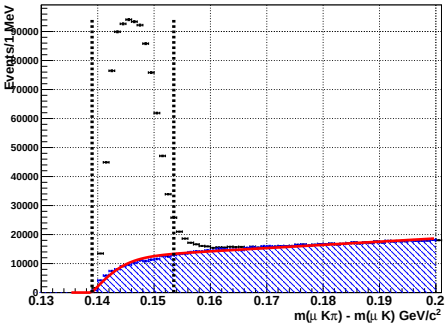

(d) $1.6 < m(\mu K)/\mathrm{GeV/c^2} < 1.7$

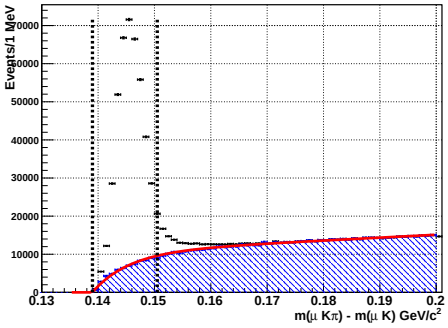

(e) $1.7 < m(\mu K)/\mathrm{GeV/c^2} < 1.8$

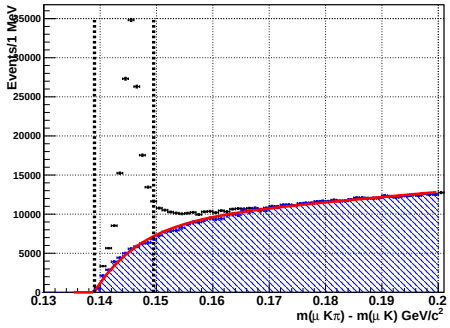

(f) $1.8 < m(\mu K)/\mathrm{GeV/c^2} < 1.9$

Figure 4.10: N_{total} extraction by background fitting. Total signal yield ∼3.5M. The unhatched histogram shows the right-sign correlated candidates. The hatched histogram shows the wrong-sign candidates as per Eqn 4.9c. The solid line is the hybrid background fit line, whereas the broken line is the maximum significance cut. The fit function is a hyperbolic tangent plus a straight line, normalised to the region below the significance cutoff. A comparison between the fitline and the wrong-sign background can be seen in Fig. 4.11.

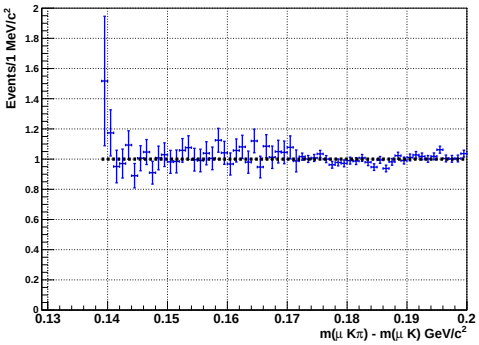

(a) $1.3 < m(\mu K)/\mathrm{GeV/c^2} < 1.4$

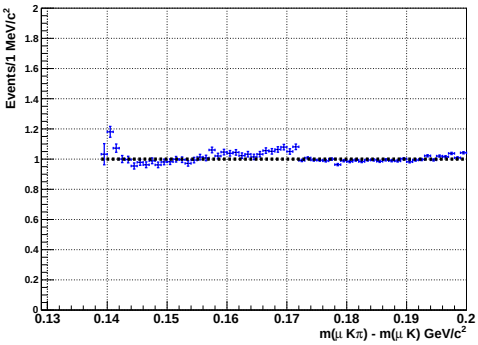

(b) $1.4 < m(\mu K)/\mathrm{GeV/c^2} < 1.5$

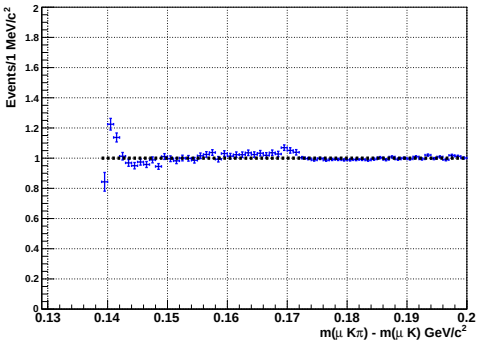

(c) $1.5 < m(\mu K)/\mathrm{GeV/c^2} < 1.6$

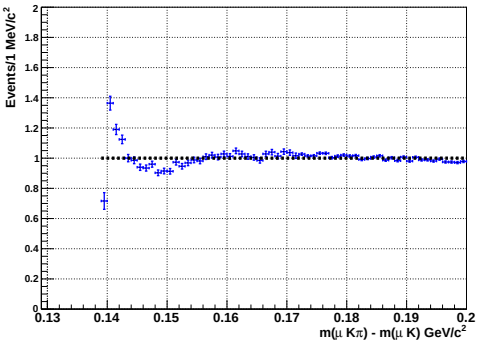

(d) $1.6 < m(\mu K)/\mathrm{GeV/c^2} < 1.7$

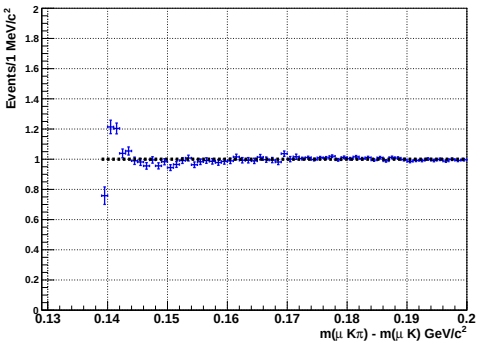

(e) $1.7 < m(\mu K)/\mathrm{GeV/c^2} < 1.8$

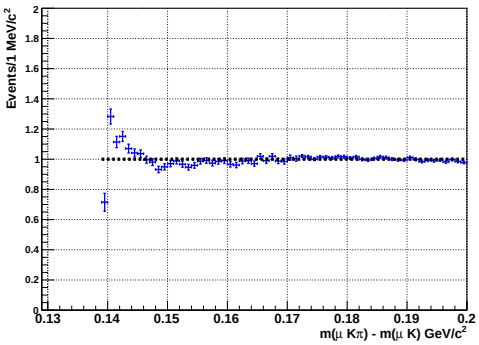

(f) $1.8 < m(\mu K)/\mathrm{GeV/c^2} < 1.9$

Figure 4.11: The wrong-sign background divided by the fit function from Fig. 4.10. The dashed black line shows histogram/fit = 1.

The high Kolmogorov-Smirnov value found when comparing the chosen wrong-sign background shape to the signalless Monte-Carlo shape suggests that the background charge correlation choice is not a source of systematic bias or uncertainty.

Changing the mass range of the sideband had negligible effect on the results. Changing the binning of the histograms had a small effect of $\Delta A_K = 0.005\%$.

The systematic uncertainty associated with the muon asymmetry increases the systematic uncertainty for each kaon momentum bin. The asymmetries along with their systematic uncertainties are listed in Table 4.5.

Combining the kaon fraction, binning effects, and an averaged muon asymmetry systematic effect, an average combined systematic uncertainty was determined to be $\sqrt{0.005\%^2 + 0.010\%^2 + 0.018\%^2} = 0.019\%$. Thus, the average kaon charge asymmetry is $A_K = (1.724 \pm 0.060(\text{stat}) \pm 0.019(\text{syst}))$ %. The systematic uncertainty is dominated by the muon asymmetry uncertainty.

4.3.9 Convolution of Kaon Asymmetry in Samples With Final State Single Kaons

If a background asymmetry has dependencies on kinematic variables of the associated particle, then one must convolute the asymmetry as a function of that variable with the fraction of the signal in the main analysis with the same kinematic properties. The weighted average number A_K is not immediately useful for removing the effects of the kaon asymmetry in other analyses with single kaons in the final state of their decays. To be able to do this one must take account of all measurables which affect the measured kaon asymmetry and convolve the distributions of those variables and the kaon asymmetry dependence on them.

It is expected that the measured asymmetry should differ with the momentum of the kaon; interaction cross-section increases with decreasing momentum, which would then increase the cross-section difference K^- and K^+ with the detector material [94]. The other possibility is the angle of kaon flight, θ_K. The raw asymmetry as defined in Eqn 4.5 displays how asymmetry is measured by candidate

counting. These counts are of reconstructed $D^* \rightarrow K\,X$ events, which is the initial number of charged kaons originating in the interaction region minus the kaons which have interacted destructively with the detector material, $N^{\pm} = N^{\pm}_{\text{initial}} - N^{\pm}_{\text{interacted}}$. If it is assumed that the number of positive and negative kaons produced are equal then

$$A_{\text{raw}} = \frac{N^{+}_{\text{interacted}} - N^{-}_{\text{interacted}}}{2N_{\text{initial}}} \sim N^{+}_{\text{interacted}} - N^{-}_{\text{interacted}} \tag{4.18}$$

However, the number of interacting kaons is proportional to the length of the Kaon trajectory in the tracking detectors, L. As seen from Fig. 4.12, $L \propto 1/\sin(\theta_K)$. As the kaon asymmetry should be dependent on the interaction cross-section between the kaon and the detector material, it is expected that the measured asymmetry should have a dependence on $1/\sin(\theta_K)$ also.

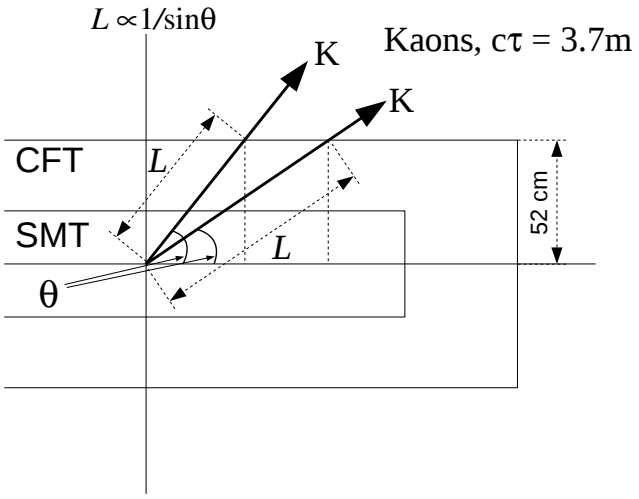

Figure 4.12: The θ dependence of the length of the kaon trajectory within the SMT and CFT.

The sample was split into kaon momentum ranges of roughly equal statistics and the analysis method was performed for each region. The result of testing asymmetry per kaon momentum bin can be seen in Fig. 4.13 and in Table 4.7. The dependence is considerable, as expected from PDG [94] and as seen in [98]. At high momentum, the asymmetry converges to a saturated value for $p(K) > 10$ GeV/c^2

p(K) range (GeV/c)	$A_K = A_{\text{raw}} + A_\mu / f_K$ %
0.7 – 1.7	2.59 ± 0.23 (stat) ± 0.05 (syst)
1.7 – 2.4	2.11 ± 0.20 (stat) ± 0.05 (syst)
2.4 – 3.2	1.81 ± 0.18 (stat) ± 0.05 (syst)
3.2 – 4.2	1.49 ± 0.17 (stat) ± 0.05 (syst)
4.2 – 5.5	1.63 ± 0.17 (stat) ± 0.05 (syst)
5.5 – 7.5	1.62 ± 0.16 (stat) ± 0.05 (syst)
7.5 – 11.5	1.55 ± 0.16 (stat) ± 0.05 (syst)
> 11.5	1.33 ± 0.16 (stat) ± 0.07 (syst)

Table 4.7: $A_K = (A_{\text{raw}} + A_\mu)/f_K$ for various kaon momentum regions. This is required to convolute the kaon charge asymmetry into other analyses by way of kaon momentum region occupation. These numbers take into account the muon reconstruction asymmetry as shown in Table 4.5. Due to charge correlations, A_μ is summed with A_{raw} to be removed. The systematic uncertainty is dominated by the systematic uncertainty in the muon asymmetry, but also includes contributions from dilution and binning as mentioned in Section 4.3.8

where $\sigma(K^+ d_{\text{total}}) \sim \sigma(K^- d_{\text{total}})$. To avoid this momentum dependence when examining the angle of flight effect on asymmetry, the region where $A_K(p_K)$ starts to saturate is examined; $4.2 < p_K < 11.5$ GeV/c^2. The sample is split into three $1/\sin(\theta_K)$ bins with approximately equal statistics. The asymmetry in these bins can be seen in Fig. 4.14 and Table 4.8. The average value band of $A(1/\sin(\theta_K)) = (1.22 \pm 0.10)\%$ passes through the uncertainty bars of every point. The three points may also be consistent with a negative slope, which is opposite to what was predicted. It is not possible to conclude on any proportional dependence in this plot with the limited statistics and datapoints. There could be systematic effects due to of inhomogeneities in the detector, but without additional statistics it will be difficult to confirm. This value coincides with the saturation asymmetry value for high $p(K)$ regions, which is also a pointer towards non-detectable dependence for this dataset. Due to the large statistical uncertainties in this search the distribution is considered to be flat and so the possible $A_K(\theta_K)$ dependence was not taken into account. The angle dependent asymmetry can not be used as a source of systematic uncertainty in the momentum dependent asymmetry due to the additional $p(K)$ cut, which means that the central values of the absolute asymmetries are not directly comparable.

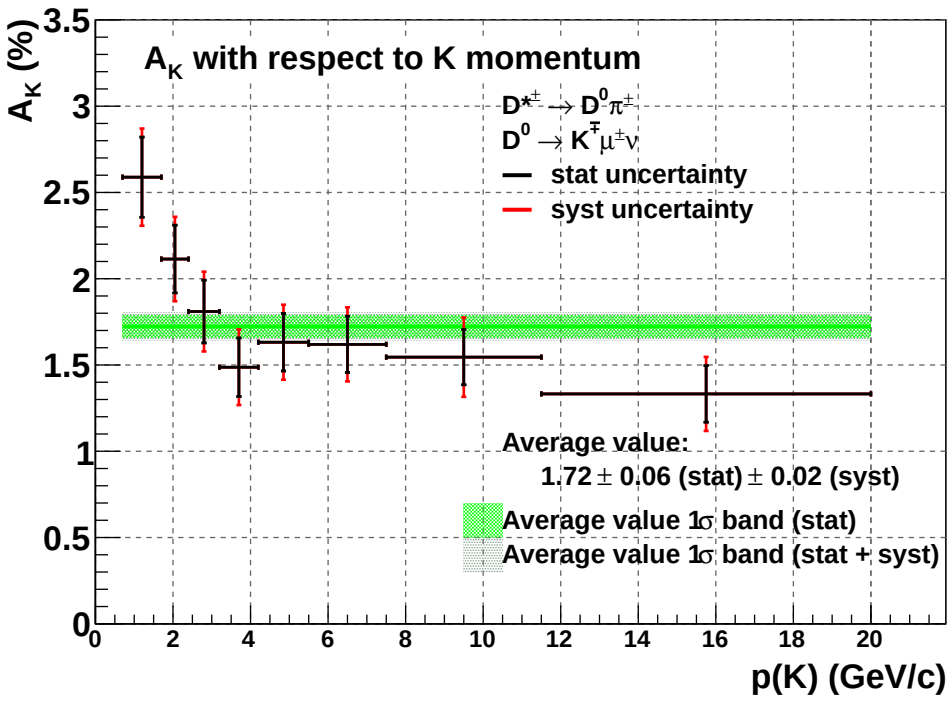

Figure 4.13: Kaon asymmetry as a function of total kaon momentum, $p(K)$. The weighted mean asymmetry with one sigma band is shown also.

To summarise, The kaon charge asymmetry that occurs as a result of charged kaon interactions with the DØ detector material as a result of different inelastic interaction cross-sections was updated to use the full RunII dataset at DØ, Fermilab. The resulting kaon asymmetry per kaon momentum range can be convoluted with the momenta distribution in a $\mathcal{CP}$ violation study that involves a single charged kaon end product to allow the subtraction of this detector asymmetry. After correcting for muon reconstruction asymmetry and dilution factors, the weighted average value was found to be $A_K = (1.724 \pm 0.060(\text{stat}) \pm 0.019(\text{syst}))\%$. The measurement is still limited by the finite size of the data sample, but has an improved precision on the previous result nonetheless.

$1/\sin(\theta_K)$ range	A_K including f_K %
1.0 – 2.0	1.52 ± 0.21
2.0 – 2.6	1.27 ± 0.17
2.6 – 3.5	0.98 ± 0.10

Table 4.8: $A_K = A_{\text{raw}}/f_K$ for various kaon momentum regions. This is required to convolute the kaon charge asymmetry into other analyses by way of kaon momentum region occupation.

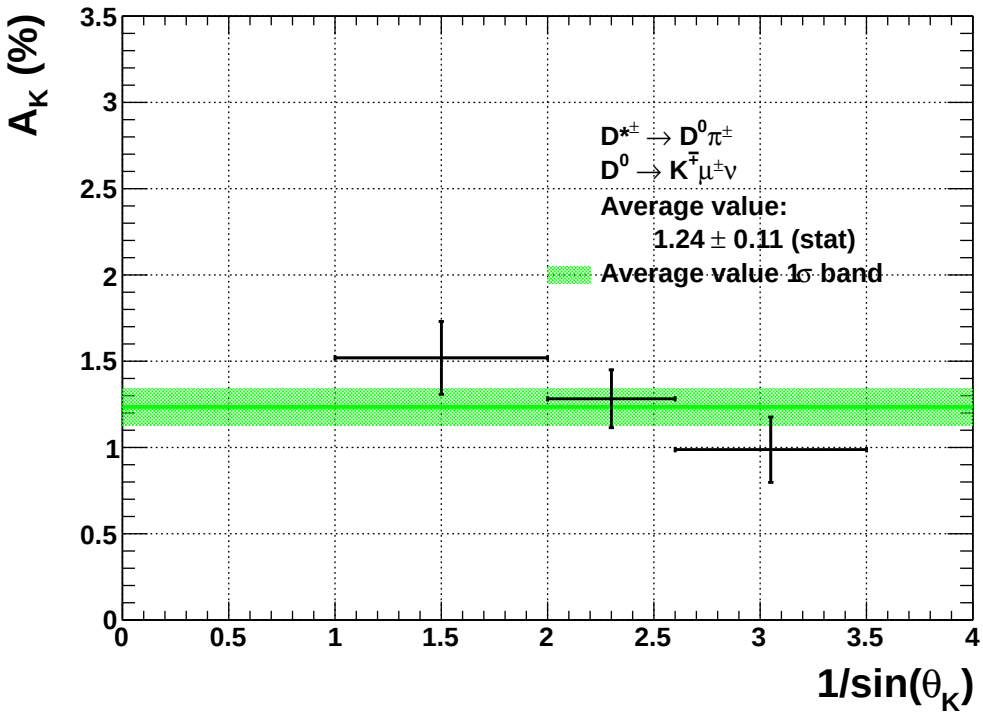

Figure 4.14: Kaon asymmetry with respect to $1/\sin(\theta_K)$, where θ_K is the sine of the angle of kaon flight in the transverse plain. The green band is the weighted average value $\pm 1\sigma$. $p(K) > 4.2$ GeV/c to avoid the kaon momentum dependence on the asymmetry. No definite dependence can be concluded. There is a suggestion that there may be a dependence of $A_K \propto -1/\sin(\theta_K)$, which is inconsistent with the prediction. Larger statistics to allow more datapoints and smaller uncertainties will be required to test this relationship further.

4.3.10 Additional DØ Analysis of A_k

A separate study of the kaon asymmetry was performed for the dimuon asymmetry analysis [104], described in the appendices B3 and C, using the $K^{*0} \rightarrow K^+\pi^-$ channel. The study was remade using the selection cuts described in Section 4.3.2. The resulting average kaon charge asymmetry was found to be $A_K = (1.176 \pm 0.046)\%$ (stat), which is significantly lower than that found using the D^* channel described in this section. This asymmetry was found to be strongly dependent of the pseudorapidity on the kaon, which is to be expected in a roughly cylindrical detector where large η values mean that more material is passed through. A large $|\eta|$ value is equivalent to a large $1/\sin(\theta_K)$ value, and the extracted asymmetry suggests that larger $|\eta|$ values produce larger kaon asymmetries. This is as predicted in Section 4.3.9. The kaon charge asymmetries per $p(K)$ and $|\eta(K)|$ region can be seen in Table 4.9 and in Fig. 4.15. A comparison for asymmetry differences per kaon momentum region can be seen in Table 4.10. The channel and methodology of this newer search is not sensitive to any anomalous direct $\mathcal{CP}$-violation in charm decays, for which evidence has recently been found at the LHCb experiment [105] and at CDF [106]. As such, the $A_K[p(K)]$ values from the K^{*0} channel shall be used for subtracting the kaon reconstruction efficiency asymmetry background from the a^d_{sl} study.

As the contamination from any B parent particle is suppressed in the D^* study, the additional track asymmetry was found to be negligible, and the extracted asymmetries are consistent with the previous D^* channel A_K study[98], the source of the discrepancy is currently unknown. An extended analysis will be performed by the Lancaster group, which will include an investigation to ensure the D^* candidates are from direct charm hadronisation and not from B mesons, and possible the role of $\mathcal{CP}$ violation in the charm system.Due to the event being tagged by the charge on the slow pion daughter particle from the D^* decay and the charges on the muon and kaon daughters of the D^0, any anomalous D^0 mixing would cause the candidate to be discarded on charge requirement grounds. This

	$A_K[p(K)](K^{*0})$ (%)		
p(K) range (GeV/c)	$\|\eta(K)\| < 0.7$	$0.7 < \|\eta(K)\| < 1.2$	$1.2 < \|\eta(K)\| < 2.2$
0.7 – 1.7	$1.453 \pm 0.131 \pm 0.073$	$1.833 \pm 0.199 \pm 0.092$	$1.535 \pm 0.571 \pm 0.077$
1.7 – 2.4	$0.948 \pm 0.152 \pm 0.047$	$1.030 \pm 0.192 \pm 0.052$	$1.627 \pm 0.258 \pm 0.081$
2.4 – 3.2	$0.724 \pm 0.174 \pm 0.036$	$1.232 \pm 0.204 \pm 0.062$	$1.363 \pm 0.240 \pm 0.068$
3.2 – 4.2	$1.000 \pm 0.209 \pm 0.050$	$0.493 \pm 0.216 \pm 0.025$	$1.694 \pm 0.245 \pm 0.085$
4.2 – 5.5	$0.437 \pm 0.241 \pm 0.022$	$0.841 \pm 0.237 \pm 0.042$	$1.874 \pm 0.243 \pm 0.094$
5.5 – 7.5	$0.176 \pm 0.269 \pm 0.009$	$0.988 \pm 0.250 \pm 0.049$	$1.323 \pm 0.234 \pm 0.066$
7.5 – 11.5	$0.221 \pm 0.343 \pm 0.011$	$0.912 \pm 0.258 \pm 0.046$	$0.975 \pm 0.227 \pm 0.049$
> 11.5	$0.137 \pm 0.540 \pm 0.007$	$0.443 \pm 0.379 \pm 0.022$	$0.955 \pm 0.224 \pm 0.048$

Table 4.9: Kaon charge asymmetry from the $K^{*0} \to K^+\pi^-$ channel per $p(K)$ and $\eta(K)$ region.

p(K) range (GeV/c)	$A_K[p(K)](K^{*0})$ (%) (stat)	(syst)	$\Delta(A_K)$ (%)	$A_K(D^{*\pm})/A_K(K^{*0})$
0.7 – 1.7	1.588 ± 0.105	± 0.079	1.00	1.63
1.7 – 2.4	1.197 ± 0.119	± 0.060	0.92	1.77
2.4 – 3.2	1.168 ± 0.125	± 0.058	0.65	1.55
3.2 – 4.2	1.203 ± 0.136	± 0.060	0.28	1.24
4.2 – 5.5	1.196 ± 0.142	± 0.060	0.43	1.36
5.5 – 7.5	0.984 ± 0.142	± 0.049	0.64	1.65
7.5 – 11.5	0.807 ± 0.157	± 0.040	0.74	1.92
> 11.5	0.743 ± 0.160	± 0.037	0.59	1.79

Table 4.10: The kaon asymmetry values for the K^{*0} channel study without $\eta(K)$ binning and how they compare to the values from the $D^{*\pm}$ channel study as described in this section. The third column is the absolute difference between asymmetry extracted from the (old) $D^{*\pm}$ channel and the (new) K^{*0} channel, and the fourth column is their ratio. The new numbers, which are immune to charm physics contamination and have been checked against B meson parentage, are roughly two-thirds the magnitude of the $D^{*\pm}$ channel numbers.

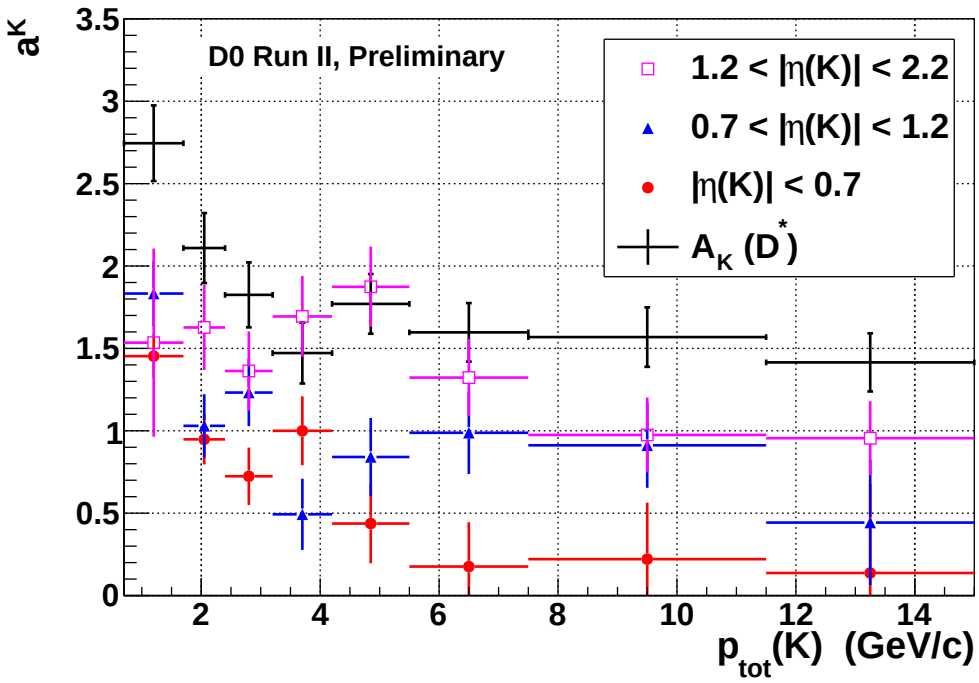

Figure 4.15: The kaon asymmetry values per kaon momentum region using the channel $K^{*0} \to K^+\pi^-$ [110].

means that if any portion of the inflated asymmetry is from D meson decays, it should come from direct $\mathcal{CP}$ violation. There is also the possibility that the enhanced asymmetry is from unexplored systematic effects which may be solved or avoided in later iterations of the $A_K(D^*)$ study.

4.4 Extraction of the Semileptonic Charge Asymmetry, a^d_{sl}

4.4.1 Motivation and Measurables

This section presents a measurement of a time integrated flavour-unspecific charge asymmetry, a^d_{sl} in the inclusive semileptonic B^0_d decay $B^0_d \to D^{*-}\mu^+\nu$, $D^{*-} \to D^0\pi^-$, $D^0 \to K^+\pi^-$, using 10.4 fb^{-1} of integrated luminosity collected by the DØ detector at Fermilab.

The asymmetry is defined in Eqn 2.73 as:

$$a^d_{sl} = \frac{N(\overline{B}^0_d \to B^0_d \to D^{*-}\mu^+) - N(B^0_d \to \overline{B}^0_d \to D^{*+}\mu^-)}{N(\overline{B}^0_d \to B^0_d \to D^{*-}\mu^+) + N(B^0_d \to \overline{B}^0_d \to D^{*+}\mu^-)}, \tag{4.19}$$

where N denotes a count of decays of that type. This is a search for $\mathcal{CP}$ violation from mixing, caused by the interference of the decay amplitudes of B^0_d and $\bar{B}^0_d$ that occur when neutral B meson oscillation takes place [107]. Non-oscillating decays provide decay amplitudes which cancel and so do not contribute to the asymmetry. The standard model predicts charge asymmetry in the B^0_d systems of a level of $a^{\rm d}_{\rm sl} = (-0.048^{+0.010}_{-0.012})\%$ [108]. As shown in Table 2.4, the current experimental average is $a^{\rm d}_{\rm sl} = (-0.47 \pm 0.46)\%$ [43]. To provide a shorthand notation, N^+ will be used to donate a decay process where the lepton candidate is a μ^+ and N^- for when the candidate is a μ^-.

As mentioned in the asymmetry extraction overview in Section 4.1, it is impossible to be certain what the parent particle is of a reconstructed decay chain,

so the first step is to extract a raw asymmetry, defined by,

$$A_{\text{raw}} \equiv \frac{N^+ - N^-}{N^+ + N^-}, \tag{4.20}$$

where the numerator is difference in count between the yields of the charge types and the denominator is the total yield of the entire sample. This value is contaminated with various background asymmetries and is diluted in contrast to the true asymmetry due to a portion of the candidates originating from non-oscillated B_d^0 or other sources, such as other B meson types or a prompt charm hadronisation. As such, it is necessary to subtract any background asymmetries and then account for the fraction of the sample that comes from the desired parent,

$$a_{sl}^d = \frac{A_{\text{raw}} - A_K - A_\mu - A_{\text{track}}}{f_{B^0_{d\,\text{osc}}}} \tag{4.21}$$

A_K, A_μ and A_{track} are detector asymmetries which can contaminate the extracted asymmetry, and are ascertained through data driven analyses. $f_{B^0_{d\,\text{osc}}}$ is a dilution factor to take into account the fraction of a sample that has candidates that originate from an oscillated B_d^0 meson, as a_{sl}^d is charge asymmetry from mixing and not direct $\mathcal{CP}$ violation. These fractions are determined using Monte-Carlo simulated data, and are discussed in Section 4.4.6. As the probability of oscillation is lifetime dependent and as there is a missing neutrino in the decay chain, the study is performed in regions of visible proper decay length (VPDL),

$$\text{VPDL} = L_{xy}(B)\frac{cM(B_d^0)}{pT(\mu D^*)_{\text{reco}}}, \tag{4.22}$$

where L_{xy} is the recorded transverse decay length, $M(B_d^0)$ is the true mass of a B_d^0, and $pT(\mu D^*)_{\text{reco}}$ is the reconstructed transverse momentum of the B candidate. The VPDL binning is as follows:

- Bin 1: -0.10 < VPDL (cm) < 0.00
- Bin 2: 0.00 < VPDL (cm) < 0.02

- Bin 3: $0.02 <$ VPDL (cm) < 0.05
- Bin 4: $0.05 <$ VPDL (cm) < 0.10
- Bin 5: $0.10 <$ VPDL (cm) < 0.20
- Bin 6: $0.20 <$ VPDL (cm) < 0.60

The first two bins are expected to contain a very low amount of oscillated B_d^0 event parents, and so should contain negligible charge asymmetry once the background and detector asymmetries have been dealt with.

The DØ detector is described in Section 3.2. The important aspects of the detector to this study are; the tracking systems (Sections 3.2.2 and 3.2.3), the muon detectors (Section 3.2.7), and the magnets (Section 3.2.4 and 3.2.7). The polarities of the two magnets are regularly reversed so to have each of the four polarity combinations exposed to approximately the same integrated luminosity. This allows for the cancellation of first order geometry based background asymmetries. It was hoped that the large statistics of the analysis would lead to a measurement with precision to compete with the current averaged uncertainty of $\pm 0.46\%$ [43].

Additionally, the analysis would be a complimentary and independent measurement of a_{sl}^d to the anomalous dimuon charge asymmetry search [46], which has dependencies on both a_{sl}^d and a_{sl}^s.

4.4.2 Event Selection

The decay chain used in this study is as follows,

$$B_d^0 \to D^{*-}\mu^+\nu,\ D^{*-} \to \overline{D^0}\pi^-_{D^*},\ \overline{D^0} \to K^+\pi^-, \tag{4.23}$$

The chain and its charge conjugate will be examined from the full dataset recorded by DØ, corresponding to 10.4 fb^{-1} of integrated luminosity. Loose quality and kinematic cuts on the tracks are described in Table 4.11. In short, four tracks are searched for which satisfy those cuts and combine to form a B decay vertex.

Producing and utilising the mass difference distribution of $m(D^* - D^0)$ reduces common systematic issues that could be present in both mass measurements. One of the cut values involves a value called 'pseudorapidity (η)', which is defined in Eqn 3.1. Another value used is significance with respect to a reference vertex, S,

$$S_{vtx} = \sqrt{(\epsilon^d/\sigma^d) + (\epsilon^z/\sigma^z)}, \tag{4.24}$$

where $\epsilon^{d/z}$ is the axial/stereo projection of the impact parameter of a track with respect to a reference vertex and σ is the corresponding uncertainty.

In addition to this, the TMVA package [90] was used to create a multivariate discriminant to reduce the combinatorial background in the $D^* - D^0$ invariant mass distribution. Twenty two variables were examined using Monte-Carlo generated signal candidates and incorrectly charge correlated candidates from data, and are described in Table 4.13. The charge correlations for wrong sign status are as follows:

- $q_K \times q_\pi > 0$
- $q_K \times q_\mu < 0$

Of the one million Monte-Carlo generated $D^* + \mu$ events generated, 124k candidates survived reconstruction and event selection. These were compared to 2.45M wrong-sign (any incorrect charge correlation) background candidates from data to create a multivariate discriminant. The boosted decision tree (BDT), log-likelihood ratio (LLR) and multi-layer perceptrons (MLP) methods were tested, where it was found that BDT gave the most efficient discriminant. An illustration of this can be seen in Fig. 4.16, where the BDT option gives a comparatively greater background rejection for the same signal efficiency. The BDT cut efficiency based upon 1000 MC signal and 1000 wrong sign background events is shown in Fig. 4.17, though the actual BDT cut values used were found using the full dataset by maximising the signal/($\sqrt{\text{signal + background}}$) significance, as can be seen in Fig. 4.18. Due to performing this analysis in bins of VPDL, a BDT cut value was required for each

VPDL region. Taking this further, the BDT cut values were determined separately for RunIIa and RunIIb. This was because the software used to generate the signal events assumed the existance of the L0 silicon detector modules, which is only the case for RunIIb. This meant that fewer signal events would be lost from a sub-efficient BDT discriminant for the RunIIa data. The cut values can be seen in Table 4.12. A demonstration of the effectiveness of this discriminator can be seen in Fig. 4.19. The signal yields before and after BDT optimisation can be seen in Fig. 4.20. By using the BDT discriminant, the signal significance for the entire dataset increased from 378.5 to 551.5 at the cost of roughly a tenth of the signal yield. This signal loss is quite small considering the drastic background reduction. It is important to reduce this combinatorial background as much as possible as the sharp turn on at $m(\pi)$ for both signal and background makes reducing the uncertainty on the signal measurements difficult, and also the uncertainties in difference plots $(N^+ - N^-)$ become larger with increasing background.

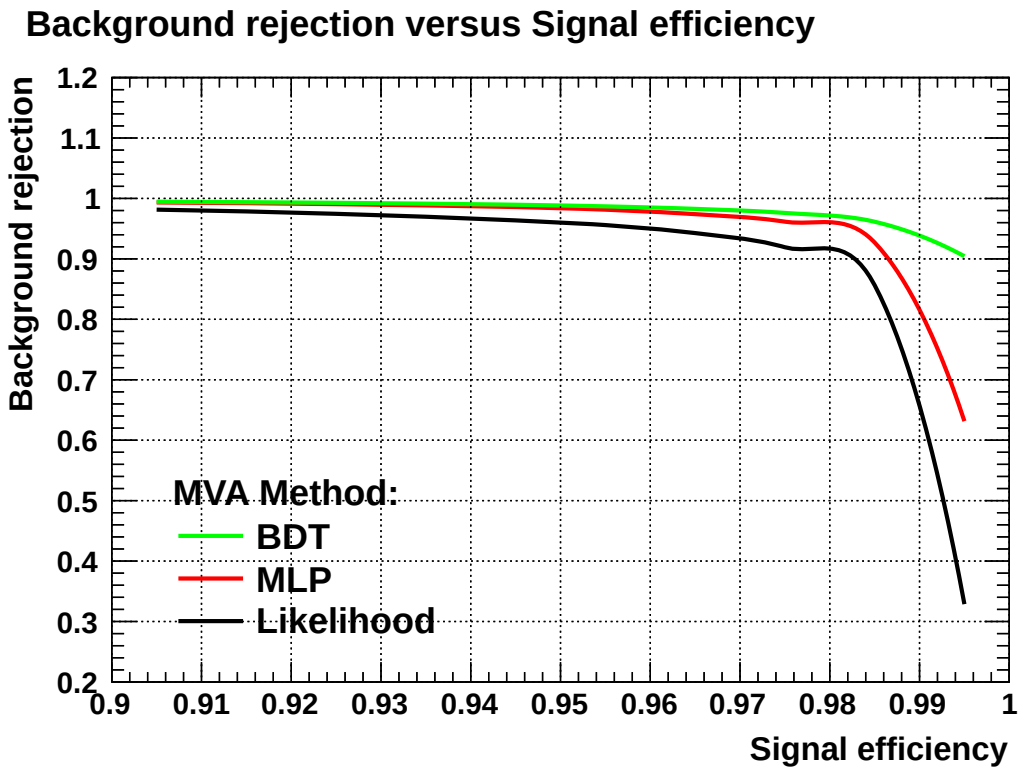

Figure 4.16: This is an illustration of the difference between the discriminating performance of BDT, MLP, and LLR as determined by TMVA. BDT gives a marginally better result, with greater background rejection for a given signal efficieny. This figure demonstrates the reason why BDT was chosen over the other options and is based upon a Monte-Carlo generated pure signal sample and a wrong-sign , no cut is based on this graph.

Particle	Cut	Notes
B_d^0	$2.0 < m(B_d^0) < 5.5$ GeV/c^2	
μ	SMT axial hits >=2	
	CFT axial hits >=2	
	SMT stereo hits >=1	
	CFT stereo hits >=1	
	"nseg" =1 or 3	see caption*
	$pT > 2.0$ GeV/c	
	$p_{\text{total}} > 3.0$ GeV/c	
$D^0(\pi K)$		Track with same charge as q_μ is designated K. πK forms the D^0 vertex, which is associated with the primary vertex
	$pT(\pi, K, D^0) > 0.7$ GeV/c	
	π, K CFT & SMT hits >=2 each	
	$\eta(D^0) < 2.0$	See Eqn. 3.2
	$S_{vtx}(D^0 wrt D^*) > 3\sigma$	See Eqn. 4.24
	$1.7 < m(D^0) < 2.0$ GeV/c^2	Tight cut to the signal region
π_{D^*}		From D^* decay, associated with D^0 and μ
	SMT hits >= 2	
	CFT hits >= 2	
D^*	$0.120 < m(D^* - D^0) < 0.200$ GeV/c^2	There is a kinematic turn on at the mass of a charged pion - there is no lower mass sideband. The upper constraint produces a wide high mass sideband to anchor the fitting of the distribution.

Table 4.11: Selection cuts for the particles in the signal decay chain.
*nseg is a measure of the quality of a muon track by noting which layers of the muon detector the track passes through. For nseg = 1 or 3 to be satisfied, it means that the track is present in at least the inner layer of the muon detector.

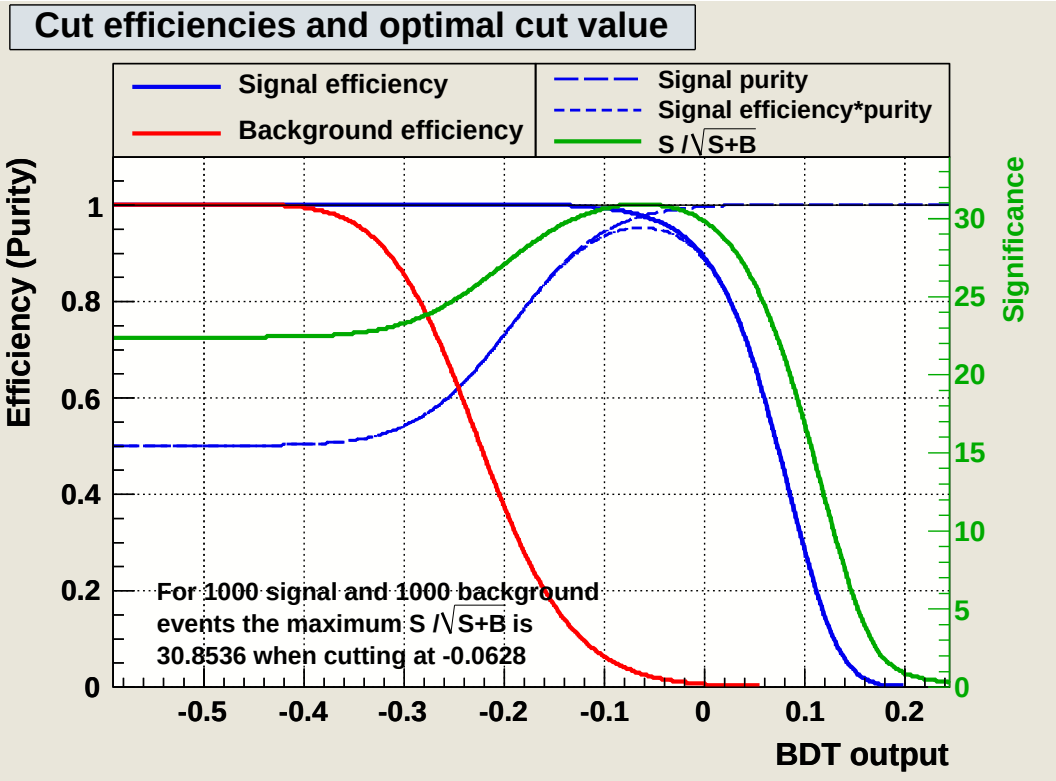

Figure 4.17: TMVA BDT cut efficiencies based on 1000 Monte-Carlo generated signal events and 1000 wrong-sign data background events with no VPDL region requirements. This is purely illustrative at this stage, as the best BDT cuts are determined from the full data sample in Fig. 4.18. This plot hints at where the best cut may be, and demonstrates how the signal/background purity and efficiencies change with BDT response.

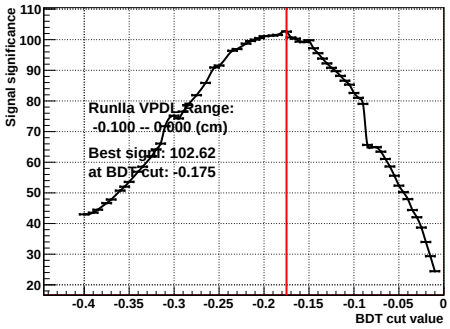

(a) RunIIa: -0.10 < VPDL (cm) < 0.00

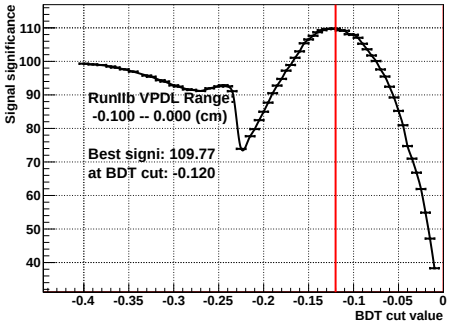

(b) RunIIb: -0.10 < VPDL (cm) < 0.00

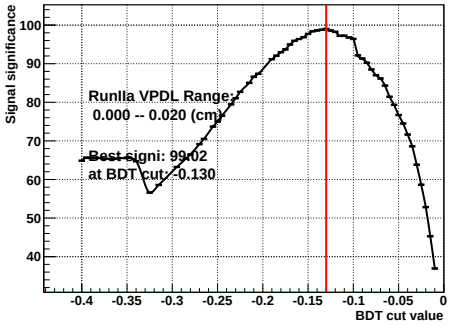

(c) RunIIa: 0.00 < VPDL (cm) < 0.02

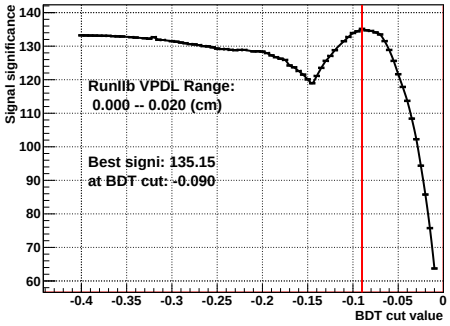

(d) RunIIb: 0.00 < VPDL (cm) < 0.02

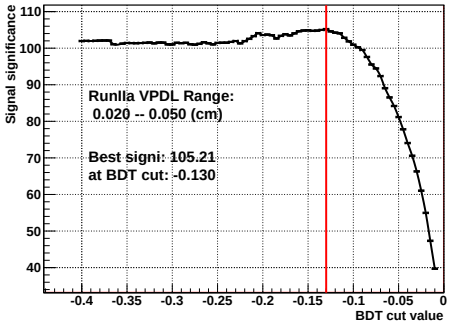

(e) RunIIa: 0.02 < VPDL (cm) < 0.05

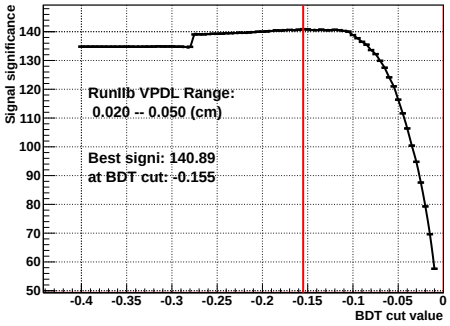

(f) RunIIb: 0.02 < VPDL (cm) < 0.05

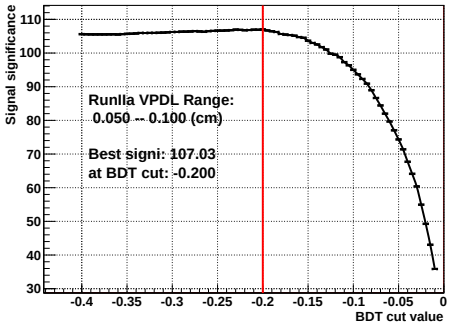

(g) RunIIa: 0.05 < VPDL (cm) < 0.10

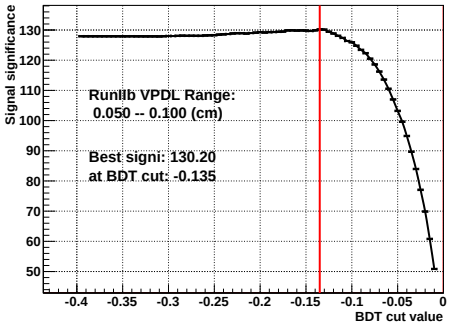

(h) RunIIb: 0.05 < VPDL (cm) < 0.10

Figure 4.18

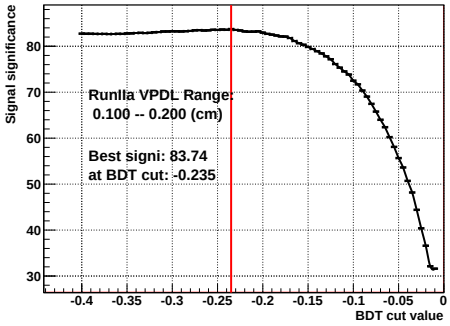

(i) RunIIa: 0.10 < VPDL (cm) < 0.20

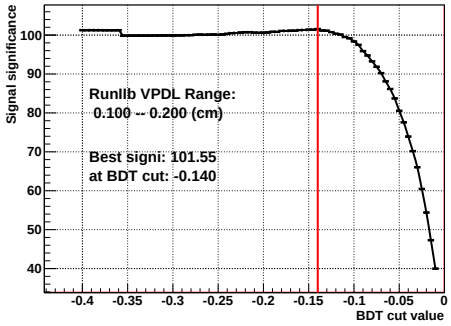

(j) RunIIb: 0.10 < VPDL (cm) < 0.20

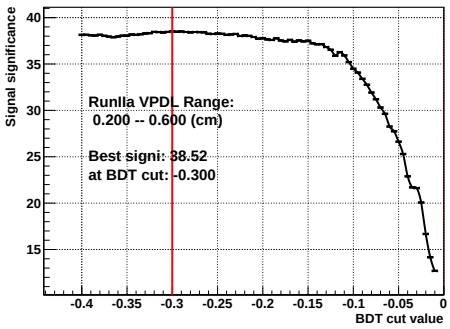

(k) RunIIa: 0.20 < VPDL (cm) < 0.60

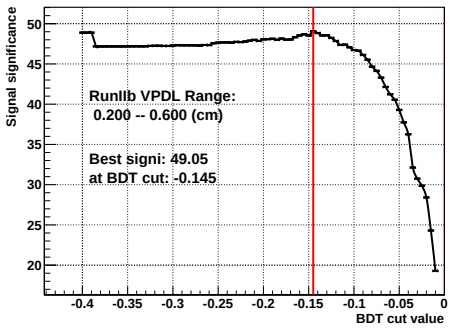

(l) RunIIb: 0.20 < VPDL (cm) < 0.60

Figure 4.18: continued - The optimum BDT cuts for each VPDL range, for the first 1.3 fb^{-1} (RunIIa) on the left and remaining 9.1 fb^{-1} (RunIIb) on the right. This is done by maximising signal/$\sqrt{\text{signal + background}}$ significance. The full fitting procedure as described in Section 4.4.3 is used to determine the signal yield, and the background yield is determined within three widths of the signal shape. The red line shows the BDT cut value which gives the maximum signal significance.

VPDL (cm)	Optimum BDT cut value for first 1.3 fb^{-1}	For the last 9.1 fb^{-1}
-0.10 → 0.00	-0.175	-0.120
0.00 → 0.02	-0.130	-0.090
0.02 → 0.05	-0.130	-0.155
0.05 → 0.10	-0.200	-0.135
0.10 → 0.20	-0.235	-0.140
0.20 → 0.60	-0.300	-0.145

Table 4.12: Optimised BDT cut values for data taking eras and VPDL regions.

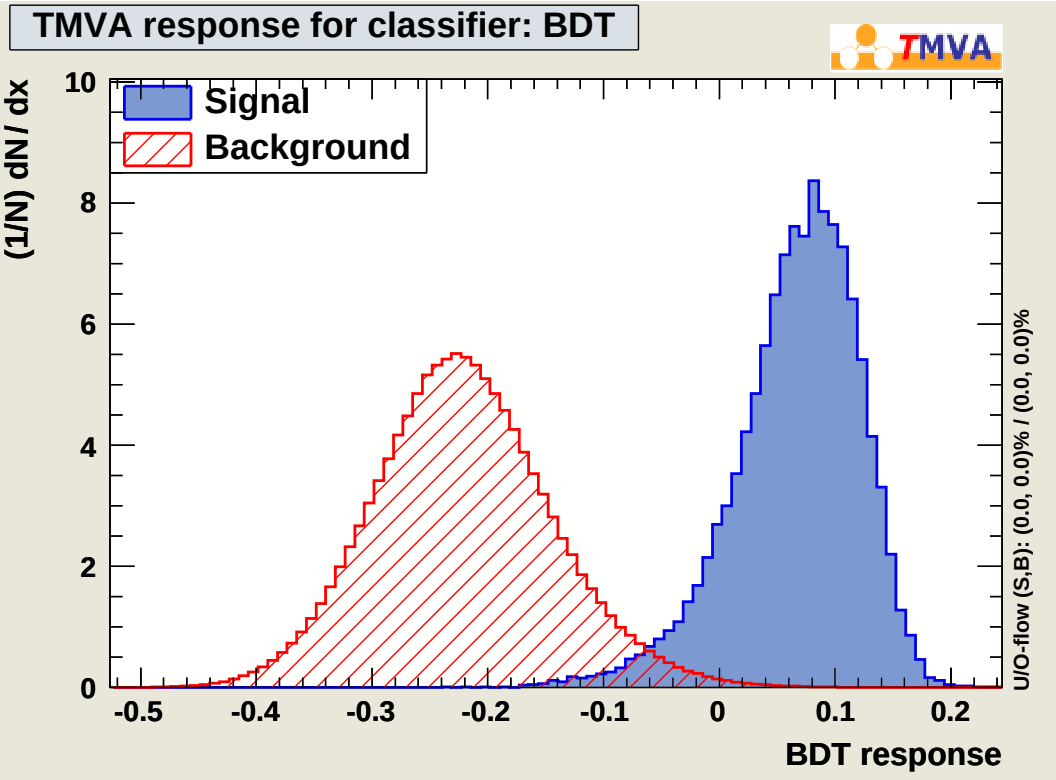

Figure 4.19: TMVA BDT response. Based on the 1000 trial Monte-Carlo generated signal events and 1000 wrong-sign background events, this shows the distribution of BDT values for signal (blue) and background (red hashed). This demonstrates how cutting on a particular BDT value can exclude background events whilst leaving the signal events intact.

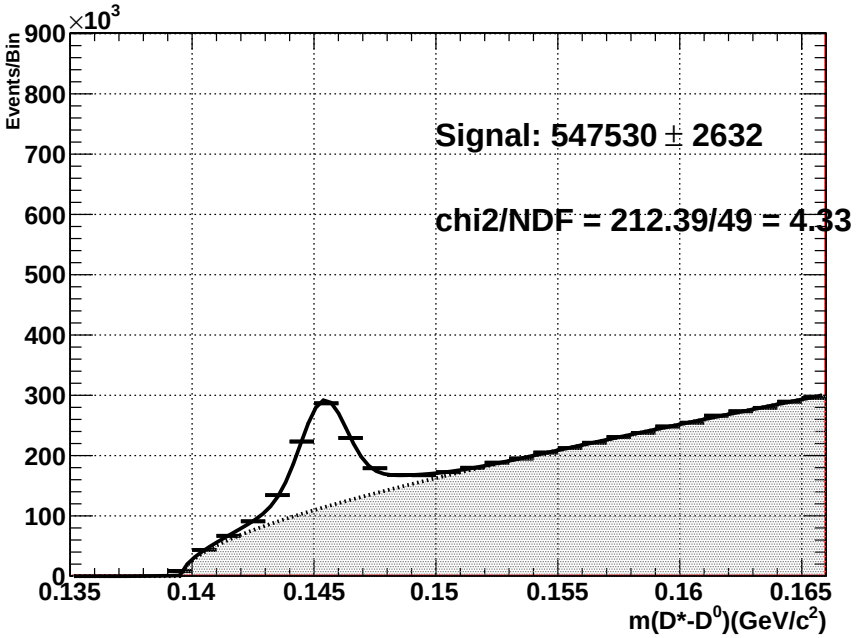

(a) Before BDT cut - Signal significance = 378.5

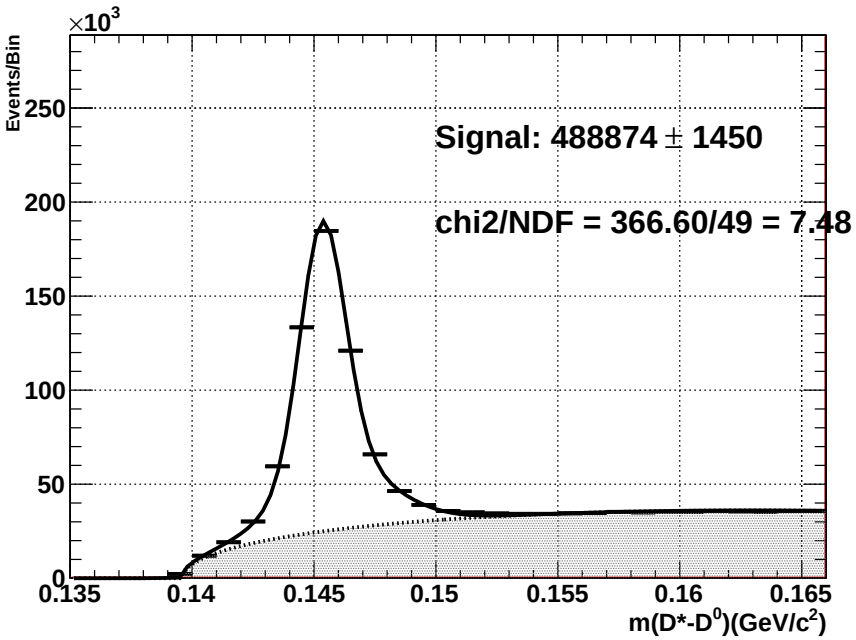

(b) After BDT cut - Signal significance = 551.5

Figure 4.20: The change in signal significance after applying the BDT discriminant to the full dataset. The histograms are binned to 1 MeV/c^2 and fit with a skewed double Gaussian signal with a power law multiplied by a linear function background. The signal significance improves drastically at the expense of roughly 10 % of the signal. The increase in χ^2 is due to the shape of the highmass sideband background being altered quite drastically in the low VPDL regions by the BDT discriminant. This can be seen in the residual plots per VPDL region [109].

Discriminating Value	Description
B candidate	
$\chi^2(B)$	chi-squared of B decay vertex
iso(B)	isolation of B
m(B)	mass of B candidate
D^* candidate	
cxy(D^*)	cosine of D^* flight angle in transverse plain from primary vertex
iso(D^*)	isolation of D^*
D^0 candidate	
dR($D\mu$)	angular separation, D^0 to muon
m(D^0)	mass of D^0 candidate
$p_T(D^0)$	transverse momentum of D^0
lxy(D^0)	track length of D^0
σlxy(D^0)	uncertainty of the track length of D^0
lxy(D^0)/σlxy(D^0)	significance of D^0 track
cxy(D^0)	cosine of D^0 flight angle in transverse plain from primary vertex
cxy(BD^0)	cosine of D^0 flight angle in transverse plain from B decay vertex
Final state hadrons	
$p_T(K)$	transverse momentum of kaon
$p_T(\pi_{D^*})$	transverse momentum of pion from the D^* decay
$p_T(\pi_{D^0})$	transverse momentum of pion from the D^0 decay
dR($K\pi_{D^*}$)	angular separation, kaon to exclusive pion
dR($K\pi_{D^0}$)	angular separation, kaon to inclusive pion
dR($\pi_{D^*}\pi_{D^0}$)	angular separation, pion to pion
iso(K)	isolation of kaon
iso(π_{D^*})	isolation of pion from D^* decay
iso(π_{D^0})	isolation of pion from D^0 decay

Table 4.13: List of variables used to build multivariate discriminant with TMVA

4.4.3 Raw Asymmetry Extraction Method

All histograms and distributions mentioned in this section assume the correct charge correlation in candidates of $q(\mu)q(K) = 1$. All mass histograms are binned with widths of 1 MeV. Before tackling the raw asymmetry it must be noted that a particle's $\mathcal{CP}$ violating parameters are not the only source of charge asymmetry.

The detector used to measure the tracks in the experiment is the source of background asymmetries, as discussed in Ssection 4.2. Weighting each reconstructed candidate so that the yield of candidates with each combination of polarities is equal and by having a large sample, the first order background asymmetries are removed when subtracting the mass distribution of candidates with μ^- from the distribution of candidates with μ^+ (i.e. $N^+ - N^-$). This weighting requires constructing four histograms from the dataset per VPDL bin; one for each toroid-solenoid polarity combination. The weighting can be based upon either the entry count in these histograms or by fitting the distribution, as the combinatorial background is not magnet-polarity-dependant. This choice of weighting is the basis for a systematic uncertainty as shall be discussed in Section 4.4.6. The fitting function, which was used later on for finding the various N values from Eqn 4.20 is as follows:

$$F = f_{\text{signal}} + f_{\text{background}} \tag{4.25}$$

$$f_{\text{signal}}(N^+ + N^-) = N\left\{ r\,\text{erfc}\left[-s\frac{(m-\mu)}{\sqrt{2}\sigma_1}\right]\frac{1}{\sqrt{2\pi}\sigma_1}\exp\left[\frac{(\mu-m)^2}{2\sigma_1^2}\right] + \right.$$
$$\left. + (1-r)\text{erfc}\left[-s\frac{(m-\mu)}{\sqrt{2}\sigma_2}\right]\frac{1}{\sqrt{2\pi}\sigma_2}\exp\left[\frac{(\mu-m)^2}{2\sigma_2^2}\right]\right\}/W \tag{4.26}$$

$$f_{\text{signal}}(N^+ - N^-) = A_{\text{raw}} \cdot f_{\text{signal}}(N^+ + N^-) \tag{4.27}$$

$$f_{\text{background}}(N^+ + N^-) = C(m - m_\pi)^a(1 + bm) \tag{4.28}$$

$$f_{\text{background}}(N^+ - N^-) = a_{bg} \cdot f_{\text{background}}(N^+ + N^-) \tag{4.29}$$

$$\tag{4.30}$$

The signal function is a skewed double Gaussian. N is the signal yield, r is the ratio of the two Gaussians involved in the signal, s is the skew, $\sigma_{1,2}$ are the sigmas of the Gaussians and μ is the central mass. W is the width of the histogram bins. The combined $(N^+ + N^-)$ histogram background shape is a straight line times by a power function with a turn on at the mass of a pion, m_π. C is a unitless numer-

ical variable. The background of the difference distribution is simultaneously fit to the same function, though multiplied by a background asymmetry factor, a_{bg}. It is expected that there should be only a small difference in combinatorial shape between candidates with a muon and those with an anti-muon, originating from kaons in the non-peaking processes. This background asymmetry should be very small compared to A_{raw}. Additionally, only the first couple of VPDL bins have a notable amount of combinatorial background, so this factor will become increasingly inconsequential with increasing VPDL region. In total, there are six signal parameters and three background parameters to describe either the combined or difference fit, totalling eleven when combining parameters for the full simultaneous fit. The weight for each polarity combination is found using Eqn 4.34, dividing the polarity with minimum events by the number of events with the polarity combination being weighted. The weighting to account for the detector asymmetries is evaluated per VPDL bin by counting candidates for each polarity combination. Signal yield fitting was also trialled, and forms the basis for one of the systematic checks listed in Section 4.4.6. These weights can be seen in Table 4.14. The binned histogram fits are conducted by minimising the χ^2 between the integration of the fit function across a bin, divided by the bin width, with the occupation number of that bin using Minuit [103]. The raw charge asymmetry is defined in Eqn 4.20. To calculate it, two distributions are required; the difference between the counts of each charge possibility and the total distribution of both charge possibilities combined. The former is made by subtracting a histogram of the mass difference $m(D^* - D^0)$ for candidates with a positive muon from the same distribution for negative muon candidates. The latter is a distribution of all candidates regardless of muon charge. The total distribution is fitted using Eqn 4.25 to find the combined yield. The signal parameter results apart from N are then fixed for fitting the difference distribution with Eqn 4.25 with the flat background, Eqn 4.29.

VPDL(B^0) (cm)	Bin 1 -0.10 → 0.00	Bin 2 0.00 → 0.02	Bin 3 0.02 → 0.05	Bin 4 0.05 → 0.10	Bin 5 0.10 → 0.20	Bin 6 0.20 → 0.60
N(+1,+1)	265642	174584	81775	51357	26634	6361
N(+1,-1)	301402	191116	87146	55416	28744	6917
N(-1,+1)	284492	180824	83286	53288	27587	6734
N(-1,-1)	278008	182921	86740	54535	27862	6703
W(+1,+1)	1.000	1.000	1.000	1.000	1.000	1.000
W(+1,-1)	0.881	0.913	0.938	0.927	0.927	0.920
W(-1,+1)	0.934	0.965	0.982	0.964	0.965	0.945
W(-1,-1)	0.956	0.954	0.943	0.942	0.956	0.949
$N_{\rm sig}$(+1,+1)	14304	36989	31623	25254	13988	3073
$N_{\rm sig}$(+1,-1)	15632	39428	33337	26791	15246	3058
$N_{\rm sig}$(-1,+1)	14069	37637	32729	26422	14505	3107
$N_{\rm sig}$(-1,-1)	15298	38079	33604	26420	14798	3057
$W_{\rm sig}$(+1,+1)	0.984	1.000	1.000	1.000	1.000	0.995
$W_{\rm sig}$(+1,-1)	0.900	0.938	0.949	0.943	0.917	1.000
$W_{\rm sig}$(-1,+1)	1.000	0.983	0.966	0.956	0.964	0.984
$W_{\rm sig}$(-1,-1)	0.920	0.971	0.941	0.956	0.945	1.000

Table 4.14: The yields and weights for candidates depending on the solenoid and toroid polarities. The default weighting method is event counting, and is covered in the first two sections of this table. The alternative method, signal fitting, is in the bottom two sections. Weighting ensures each combination has equal exposure to the results, making the first order detector asymmetries cancel.

Sensitivity

A sensitivity test was performed before extracting the raw asymmetry. The full process of the extraction is performed, but the muon charges were forced as so to produce a set asymmetry in the sample of 1.5 %. The setting and asymmetry extraction was performed a thousand times, each iteration creating a randomised 1.5 % asymmetrical distribution to be fit. By plotting the extracted asymmetries and fitting a Gaussian curve to the distribution, the expected raw asymmetry precision can be estimated to be the sigma of that Gaussian. Bias is shown if the average is significantly different from 1.5 %. The results of this test for various VPDL regions can be seen in Fig.4.22. For the unsplit sample, the sensitivity was found to be 0.17%, as displayed in Fig. 4.21.

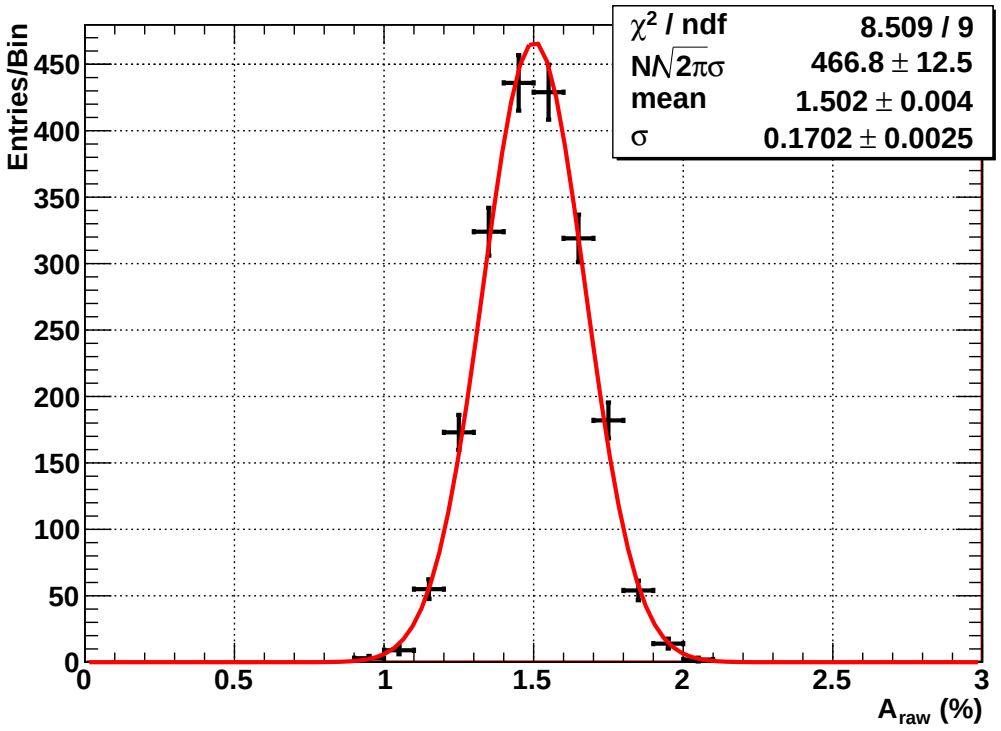

Figure 4.21: The statistical sensitivity of the dataset without lifetime splitting. This is made by running the analysis procedure many times with randomised muon charges that seed a 1.5 % input asymmetry, then plotting the extracted asymmetry. The statistical sensitivity on the raw asymmetry extraction is $\sim 0.17\%$.

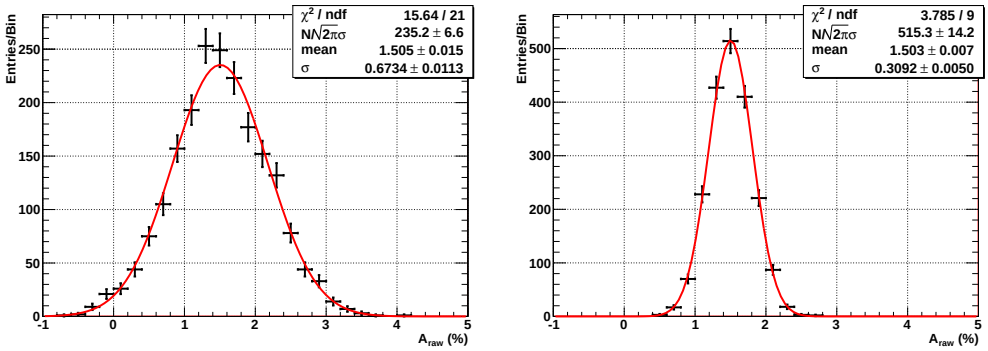

(a) -0.10 < VPDL (cm) < 0.00

(b) 0.00 < VPDL (cm) < 0.02

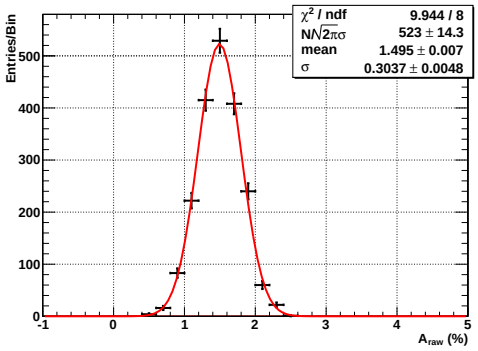

(c) 0.02 < VPDL (cm) < 0.05

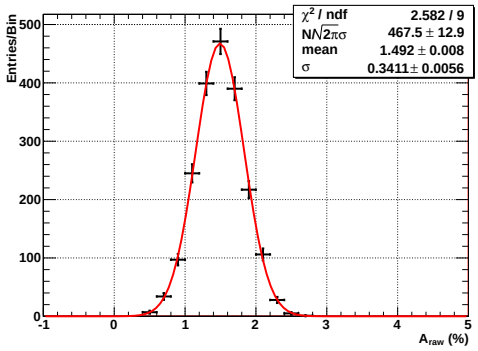

(d) 0.05 < VPDL (cm) < 0.10

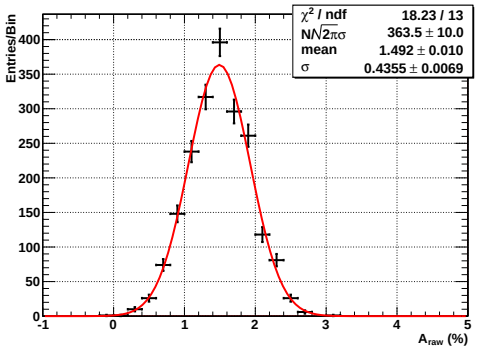

(e) 0.10 < VPDL (cm) < 0.20

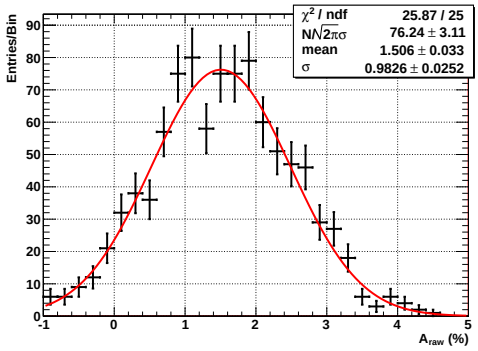

(f) 0.20 < VPDL (cm) < 0.60

Figure 4.22: The statistical sensitivity of the dataset for lifetime regions. This is made by running the analysis procedure many times with the distribution of equally numbered muon and antimuons randomised for events passing cuts, and plotting the extracted asymmetry. The expected statistical sensitivity for each VPDL region in percent is the σ value shown in the respective plot.

A further biasing test was conducted, where the input asymmetry was varied from -5% to +5%, where input asymmetry was then plotted against extracted asymmetry. A straight line fit was performed. If the intercept or gradient did not agree with $y = x$, then the fit would be biased. The resulting line of $y = (0.993 \pm 0.004)x + (0.008 \pm 0.012)$ suggests the asymmetry extracting procedure is adequately robust. The result of this test can be seen in Fig. 4.23.

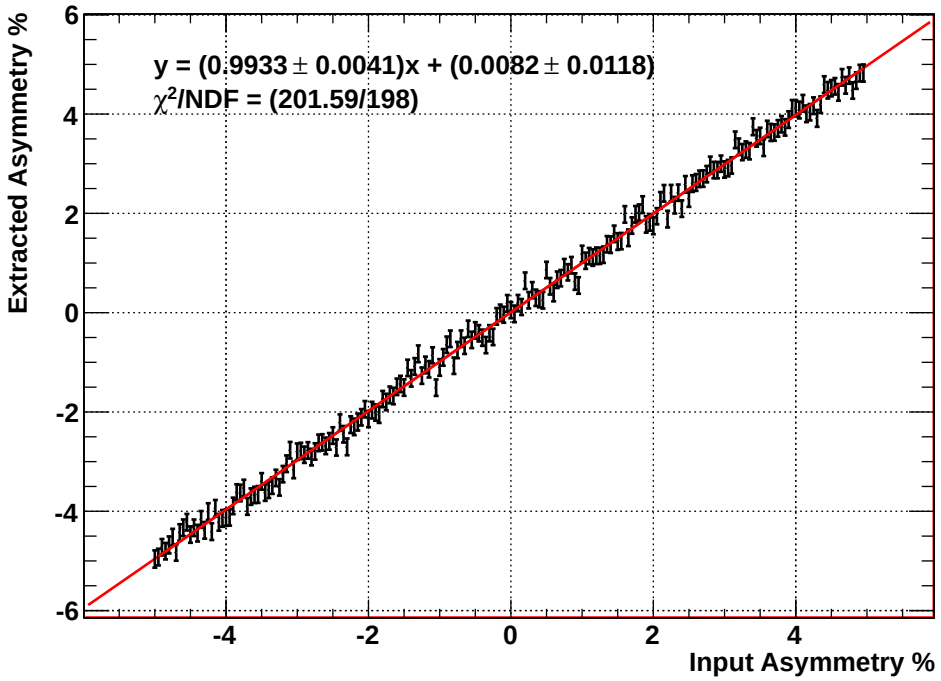

Figure 4.23: The extracted asymmetry as provided by the analysis compared to an artificial asymmetry introduced to the data sample. A perfect straight line of gradient unity and intercept zero would demonstrate perfect asymmetry extraction.

4.4.4 Raw Asymmetry Extraction Results

The raw asymmetry extraction process was be conducted for six bins of VPDL. This will allow factoring in how the fraction of the sample that has come from an oscillated B_d^0 changes with lifetime. The bins were chosen to be identical to the ones used in the parallel a_{sl}^d study using $B_d^0 \to D^- \mu^+ X$ [110]. This will allow the results to be combined easily. The results of the fits can be seen in Fig. 4.24

for the combined sample, and Fig. 4.25 per VPDL range. The extracted signal parameters and uncertainties of raw asymmetries are in Table 4.15.

	Bin 1			Bin 2			Bin 3			Bin 4			Bin 5			Bin 6		
VPDL (cm)	-0.10	→	0.00	0.00	→	0.02	0.02	→	0.05	0.05	→	0.10	0.10	→	0.20	0.20	→	0.60
$N(D^{*\pm})$	54898	±	1249	145492	±	969	126487	±	645	100184	±	568	56168	±	391	11725	±	177
A_{raw}	0.0180	±	0.0069	0.0107	±	0.0031	0.0098	±	0.0031	0.0144	±	0.0034	0.0214	±	0.0045	0.0051	±	0.0101
ΔM (MeV/c^2)	145.00	±	0.07	144.99	±	0.03	144.92	±	0.02	144.88	±	0.03	144.86	±	0.03	144.89	±	0.08
σ_{G1} (MeV/c^2)	0.90	±	0.05	0.95	±	0.02	0.99	±	0.02	1.04	±	0.02	1.08	±	0.03	1.01	±	0.06
σ_{G2} (MeV/c^2)	2.27	±	0.19	2.33	±	0.06	2.41	±	0.05	2.58	±	0.06	2.69	±	0.08	2.43	±	0.15
f_{G1}	0.58	±	0.04	0.62	±	0.01	0.63	±	0.01	0.65	±	0.01	0.66	±	0.01	0.60	±	0.04
skew	0.453	±	0.093	0.563	±	0.038	0.636	±	0.032	0.673	±	0.036	0.719	±	0.047	0.632	±	0.101
χ^2/ndf	68	/	51	107	/	51	198	/	51	148	/	51	135	/	51	76	/	51
χ^2(sum)/ndf	45	/	22	80	/	22	179	/	22	121	/	22	107	/	22	45	/	22
χ^2(diff)/ndf	22	/	22	28	/	22	19	/	22	27	/	22	28	/	22	31	/	22

Table 4.15: Extracted raw asymmetry parameters and uncertainties using Eqn 4.20 for various reconstructed B_d^0 visible proper decay lengths. Only the statistical uncertainties are shown. The central asymmetry values were blinded until all sensitivity tests were concluded to guard against experimenter bias.

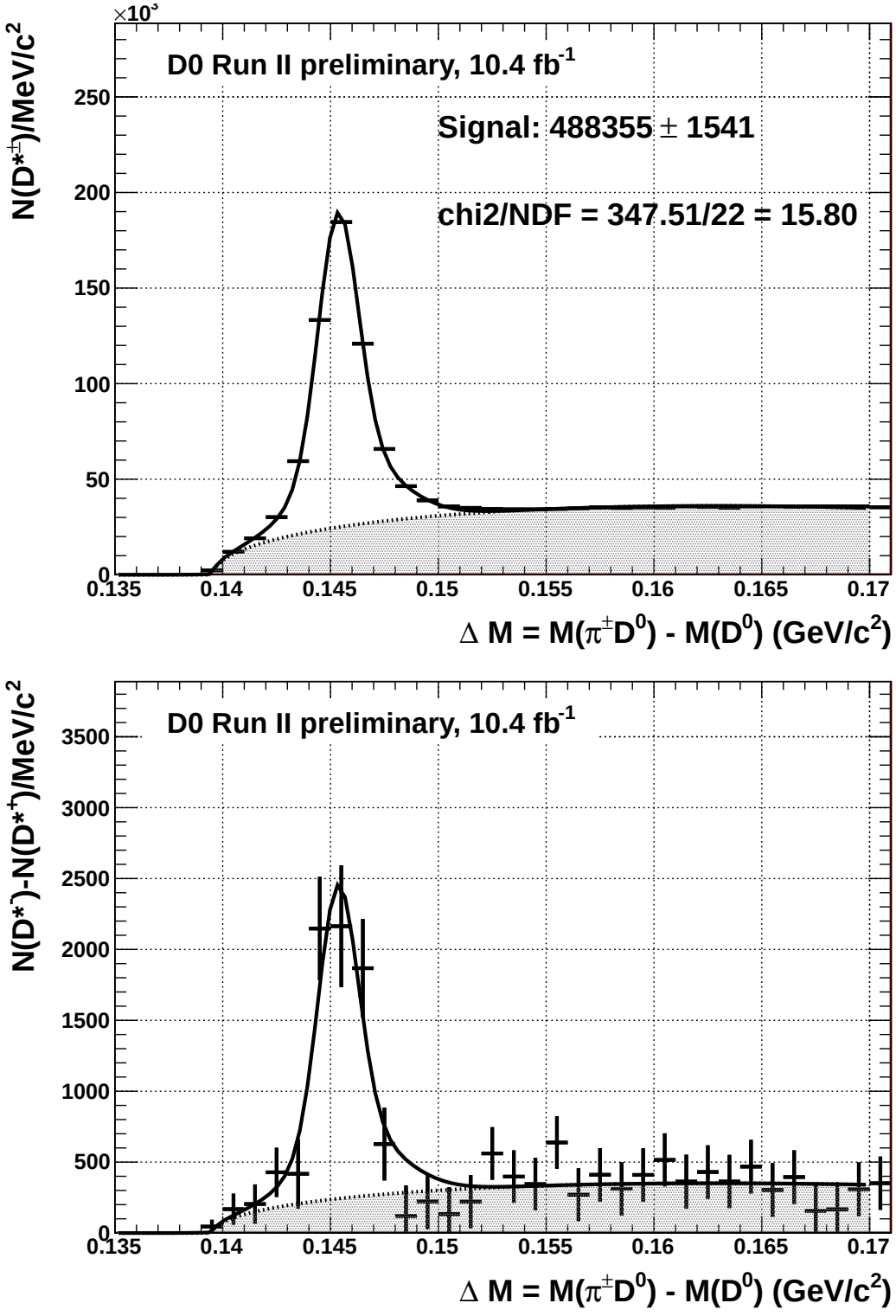

Figure 4.24: Combined (above) and Difference (below) fits for the full 10.4 fb^{-1} dataset without VPDL binning. The χ^2/NDF of the difference plots can be seen in Table 4.15, and are all close to unity.

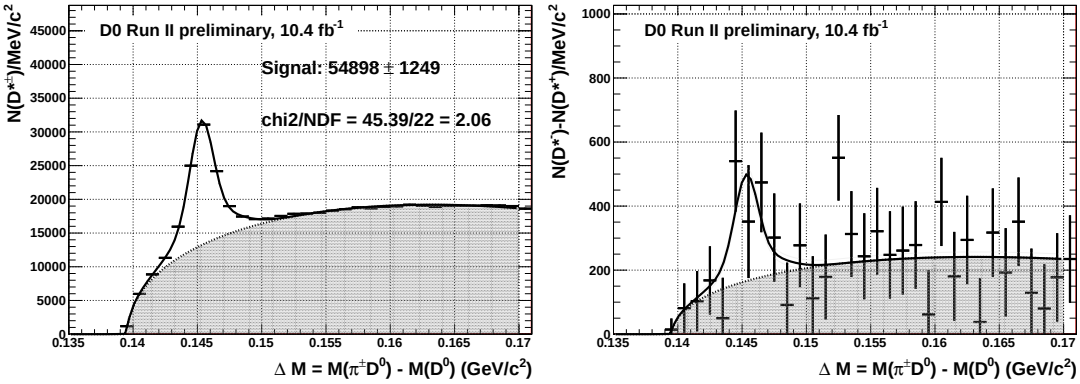

(a) -0.10 < VPDL (cm) < 0.00

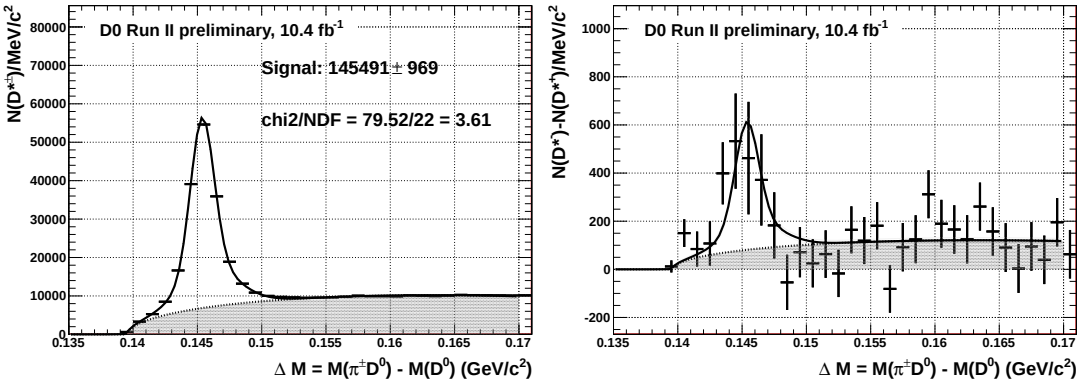

(b) 0.00 < VPDL (cm) < 0.02

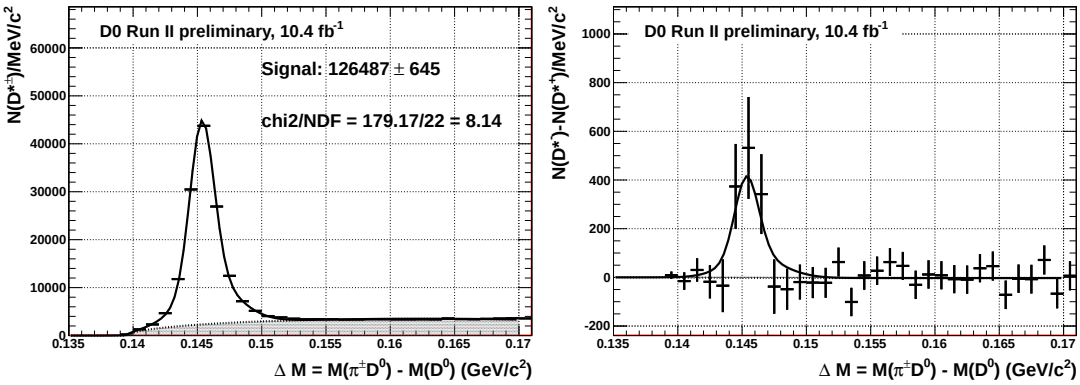

(c) 0.02 < VPDL (cm) < 0.05

Figure 4.25

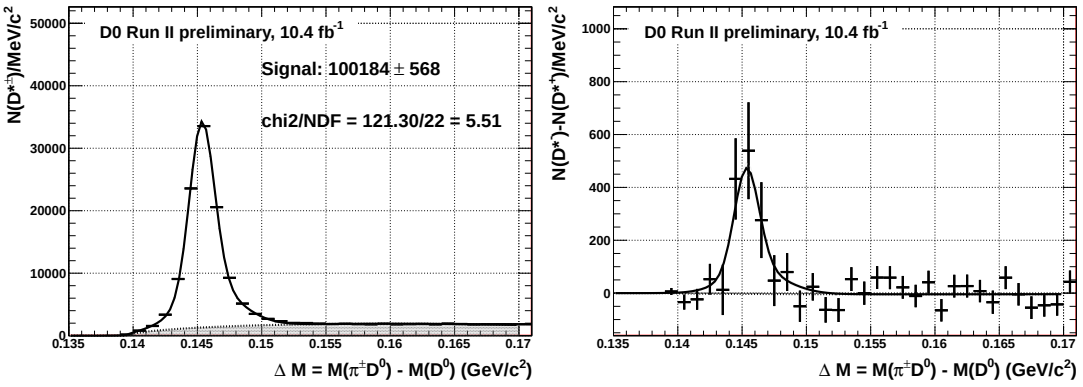

(d) $0.05 <$ VPDL (cm) < 0.10

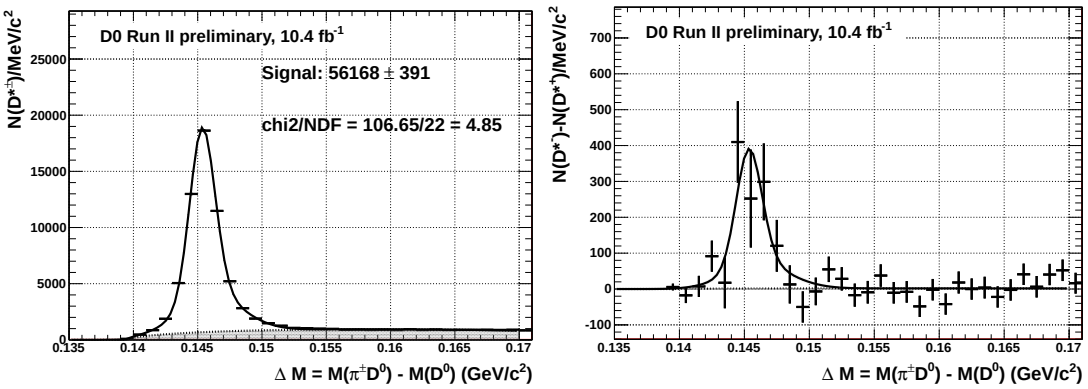

(e) $0.10 <$ VPDL (cm) < 0.20

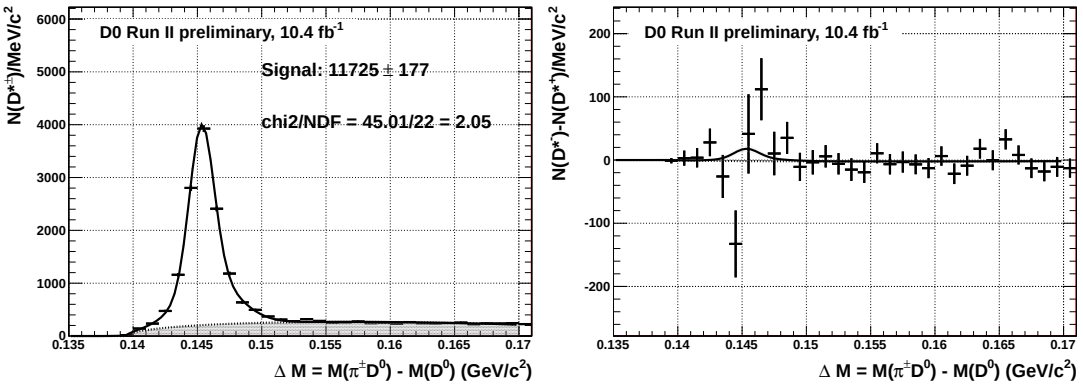

(f) $0.20 <$ lVPDL (cm) < 0.60

Figure 4.25: continued - Combined and Difference fits for the full 10.4 fb^{-1} dataset. Combined signal(left) and $\mu^+ - \mu^-$ difference(right) yields for the different VPDL(B) regions. Uncertainties are statistical only. The points are data, the solid line is the combined fit, the shaded area is the combinatorial background fit. Combined and difference plots are fitted simultaneously with Eqn 4.25. The residual plots for these fits can be seen in [109]

Comparing the sensitivities to the extracted uncertainties, it can be seen that the final results are of the same order as what can statistically be expected. The differences reported would be due to differing background shapes between a uniform enforced asymmetry in the background in the sensitivity test and an background asymmetry in data averaged over the mass difference range. A comparison can be seen in Table 4.16.

4.4.5 Background Asymmetries

The reconstruction efficiency for muons and anti-muons is different, leading to a charge asymmetry in the particles used to tag B flavour at decay [100]. The resulting asymmetries are muon transverse momentum dependent, and so can be convoluted with the signal yields in this analysis per muon transverse momentum region. The corrections from this are small, and were calculated in a data driven tag and probe analysis of J/Ψ decays [100]. The fractional occupation convoluted corrections can be seen in Table 4.17. Also present may be a reconstruction efficiency for the additional hadron tracks of opposite charges. The resulting asymmetry was found to be transverse momenta independent, so a single correction could be made to the raw asymmetry to account for this. The correction was found to be $A_{\text{track}} = 0.0030 \pm 0.0058$ % [97], which is negligible to the sensitivity of this analysis.

VPDL range (cm)	Sensitivity (%)	σA_{raw} (%)
-0.10 $\rightarrow$ 0.00	0.67	0.69
0.00 $\rightarrow$ 0.02	0.31	0.31
0.02 $\rightarrow$ 0.05	0.30	0.31
0.05 $\rightarrow$ 0.10	0.34	0.34
0.10 $\rightarrow$ 0.20	0.44	0.45
0.20 $\rightarrow$ 0.60	0.98	1.01

Table 4.16: Statistical sensitivities compared to extracted raw asymmetry uncertainties. The values are very close, as expected. Any differences would be due to signal and background shape differences between an input asymmetry sensitivity test and in unmodified data.

VPDL range (cm)	Muon asymmetry correction, A_μ (%)
-0.10 $\rightarrow$ 0.00	0.097 $\pm$ 0.027 (stat) $\pm$ 0.018 (syst)
0.00 $\rightarrow$ 0.02	0.098 $\pm$ 0.031 (stat) $\pm$ 0.022 (syst)
0.02 $\rightarrow$ 0.05	0.100 $\pm$ 0.033 (stat) $\pm$ 0.024 (syst)
0.05 $\rightarrow$ 0.10	0.101 $\pm$ 0.033 (stat) $\pm$ 0.023 (syst)
0.10 $\rightarrow$ 0.20	0.101 $\pm$ 0.033 (stat) $\pm$ 0.021 (syst)
0.20 $\rightarrow$ 0.60	0.101 $\pm$ 0.031 (stat) $\pm$ 0.017 (syst)

Table 4.17: Muon asymmetry corrections per VPDL range. These are the absolute muon asymmetries convoluted with muon transverse momenta occupancies, as discussed in [100].

The largest background asymmetry remaining after the polarity weighting is that of the kaon reconstruction efficiency asymmetry as determined in Section 4.3. The signal yields were found for the same kaon momentum regions mentioned in Table 4.7 and were converted into fractional occupations. The asymmetries in the same table were then convoluted with the momenta distribution occupations to provide an asymmetry correction per VPDL region; $A_{\rm K} = \sum_i A_K(p(K))_i \times f_i$, where f_i is the fraction of candidates in the sample with kaon momentum in the $i^{\rm th}$ range. This value is to be summed with the raw asymmetry due to charge correlations. The table of kaon asymmetries corrections per VPDL region can be seen in Table 4.18. The fractional $p(K)$, $|\eta(K)|$ occupation of kaon candidates can be seen in Fig. 4.26, which is used to convolute the values from Table 4.9 into the background kaon charge asymmetry correction. The result of subtracting the background asymmetries from the raw asymmetry can be seen in Fig. 4.27. What is important to take from this plot is that the first two points, which correspond to the insensitive VPDL regions, are consistent with zero. This is a good indication that the background asymmetries have been cancelled out.

4.4.6 Dilution

To convert the extracted asymmetry to the asymmetry in B^0_d it is required to know the fraction of the sample used that originated with an oscillated B^0_d. Only with oscillation can a semileptonic B^0_d decay produce a measurable $\mathcal{CP}$ violation as

VPDL range (cm)	Kaon asymmetry correction, A_K (%)
-0.10 $\rightarrow$ 0.00	0.947 $\pm$ 0.060 (stat) $\pm$ 0.012 (syst)
0.00 $\rightarrow$ 0.02	0.893 $\pm$ 0.063 (stat) $\pm$ 0.012 (syst)
0.02 $\rightarrow$ 0.05	0.900 $\pm$ 0.061 (stat) $\pm$ 0.012 (syst)
0.05 $\rightarrow$ 0.10	0.913 $\pm$ 0.060 (stat) $\pm$ 0.012 (syst)
0.10 $\rightarrow$ 0.20	0.914 $\pm$ 0.060 (stat) $\pm$ 0.012 (syst)
0.20 $\rightarrow$ 0.60	0.934 $\pm$ 0.062 (stat) $\pm$ 0.012 (syst)

Table 4.18: Kaon asymmetry corrections per VPDL range. These are the absolute kaon asymmetries convoluted with kaon total momentum occupancies found using the K^{*0} channel, as discussed in Section 4.3.10.

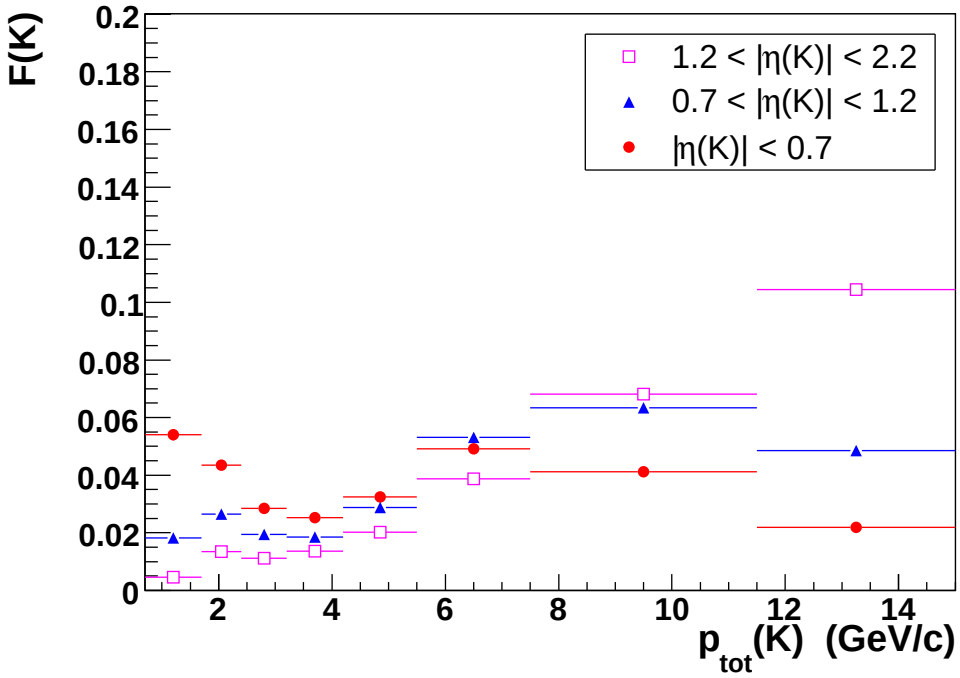

Figure 4.26: Fractional occupation of kaon candidates per kaon momentum and kaon pseudorapidity region.

oscillation is the source of the differing decay amplitudes, as noted in Section 2.3.

It is possible that the candidates may have originated from a prompt charm quark decay to D^*, though this dilution will only affect low VPDL bins. These events are named 'prompt'. It is also possible for $B^{\pm}$ and B_s mesons to produce decay chains which can be reconstructed to form a peak in the ΔM signal region. The mixing frequency of B_s is rapid, so approximately half of the B_s parents will have oscillated. This introduces a small contribution from a^s_{sl} into the calculation, which can be accounted for with a systematic uncertainty. Such decay possibilities

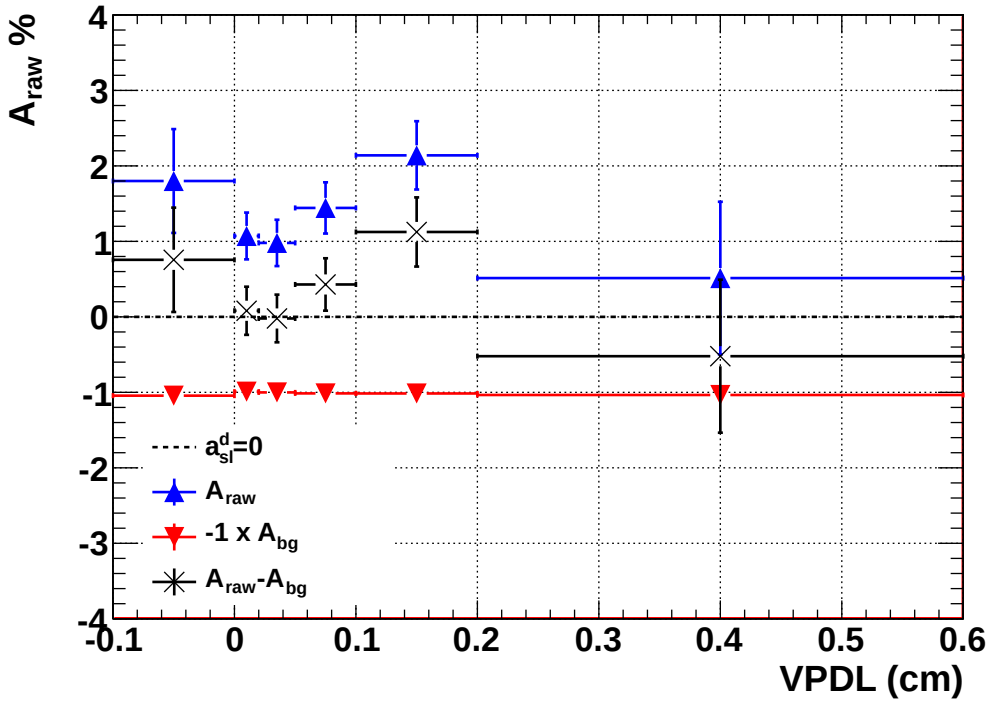

Figure 4.27: Extracted raw asymmetry with the background kaon and muon asymmetries removed. Due to charge correlations, this is done by performing $A_{\text{raw}} - A_K - A_\mu$. The first two bins, which have a negligible fraction of oscillated B_d^0 parents, are consistent with zero. This is a good indication that all background asymmetries have been negated.

are listed in Table 4.19.

To test this, 2M Monte-Carlo events were generated from quark level that required a D^* and an exclusive muon, where the D^* decayed as per the signal decay chain. For every event, the true parent(s) of every muon and D^* in the event were found up to the level of a B meson or a quark. If the parent was of type B_d^0 or B_s^0 then the true particle decay length was found and the probability that the hadron would have oscillated was found using [111],

$$P(\text{mix}) = \frac{1}{2}[1 - \cos(\Delta M t)], \tag{4.31}$$
$$t = \frac{m(B)d}{p(B)c},$$

where ΔM is the mass differences between the respective B meson eigenstates as found on PDGlive [101], t is the lifetime of the B meson as calculated from the

truth information of its mass, decay length, d, and momentum. The event was then processed by the analysis code used to extract signal candidates. If both the D^* and μ candidates were fully reconstructed and matched to the respective particle in the truth information, then the parent type for that decay was noted, along with the proper lifetime for use in calculating the probability of mixing for the B_d^0 case. For each of the reconstructed lifetime bins used in the analysis, the signal yield of each parent type is extracted and the relative fraction calculated, along with the probability of oscillation. As expected, the fraction of oscillated B_d^0 parents increases with reconstructed lifetime, as seen in Fig. 4.28 and Table 4.20.

Channel	Parent	Chain	Branching Ratio ($\Gamma_i/\Gamma_{totB_q^{0/\pm}}$) [8]
1	B^+	$B^+ \to \bar{D}_1^0(2420)\mu^+\nu_\mu$ $\bar{D}_1^0(2420) \to D^{*-}(2010)\mu^+\nu_\mu$	$(2.5 \pm 0.5) \times 10^{-3}$
2	B^+	$B^+ \to \bar{D}_2^{*0}(2460)\mu^+\nu_\mu$ $\bar{D}_2^{*0}(2460) \to D^{*-}(2010)\mu^+\nu_\mu$	$(1.53 \pm 0.16) \times 10^{-3}$
3	B^+	$B^+ \to D^{*-}\pi^+\mu^+\nu_\mu$ $(\pm)$	$(6.1 \pm 0.6) \times 10^{-3}$
4	B_s	$B_s \to \bar{D}_{s1}^-(2536)\mu^+\nu_\mu$	$(2.5 \pm 0.7) \times 10^{-3}$
5	B_s	$B_s^0 \to \bar{D}_{s2}^-(2573)\mu^+\nu_\mu$	$(2.6 \pm 1.2) \times 10^{-3}$
6	B_s	$B_s^0 \to \bar{D}^{*0}K^-\mu^+\nu_\mu$ or $B_s^0 \to \bar{D}^{*-}K^0\mu^+\nu_\mu$ or $B_s^0 \to \bar{D}^0K^-\mu^+\nu_\mu$	Not listed
9	c	$c \to D^{(*)}$	Direct hadronisation

Table 4.19: Background decays which may contribute to the signal peak in this analysis. Candidates reconstructed from these events act to dilute the measured asymmetry, apart from B_s parents which contaminate the result with contributions from a_{sl}^s.

The extracted raw asymmetry, corrected for background asymmetries, was divided by the fraction of oscillated candidates. The resulting asymmetry distribution is shown in Section 4.4.7 after the systematic analysis. The a_{sl}^d(VPDL) distribution is consistent with a straight line as expected, as a_{sl}^d is not time dependent.

	Bin 1	Bin 2	Bin 3	Bin 4	Bin 5	Bin 6
VPDL (cm)	-0.10 $\rightarrow$ 0.00	0.00 $\rightarrow$ 0.02	0.02 $\rightarrow$ 0.05	0.05 $\rightarrow$ 0.10	0.10 $\rightarrow$ 0.20	0.20 $\rightarrow$ 0.60
$f_{B_d^0}$(osc) %	1.28 $\pm$ 0.15	0.98 $\pm$ 0.03	6.15 $\pm$ 0.11	23.12 $\pm$ 0.37	56.99 $\pm$ 0.83	71.30 $\pm$ 1.70
$f_{B_d^0}$(total) %	55.96 $\pm$ 1.03	83.50 $\pm$ 0.38	90.09 $\pm$ 0.32	90.34 $\pm$ 0.36	88.02 $\pm$ 0.52	83.63 $\pm$ 1.30
$f_{B_s^0}$ %	0.94 $\pm$ 0.20	1.06 $\pm$ 0.10	1.44 $\pm$ 0.13	1.34 $\pm$ 0.14	1.57 $\pm$ 0.20	1.73 $\pm$ 0.48
$f_{B^\pm}$ %	5.83 $\pm$ 0.48	7.26 $\pm$ 0.27	8.01 $\pm$ 0.29	8.32 $\pm$ 0.33	10.35 $\pm$ 0.49	14.64 $\pm$ 1.23
f_{prompt} %	37.27 $\pm$ 1.00	8.18 $\pm$ 0.28	0.46 $\pm$ 0.07	0.00 $\pm$ 0.00	0.05 $\pm$ 0.04	0.00 $\pm$ 0.00

Table 4.20: The absolute fractions of the sample that originated from various parent types per VPDL region. $f_{B_d^0}$(total) includes the fraction of non-oscillated and oscillated ($f_{B_d^0}$(osc)) B_d^0 parents. The fraction of oscillated B_d^0 that have undergone mixing contribute to the semileptonic charge asymmetry is shown in red.

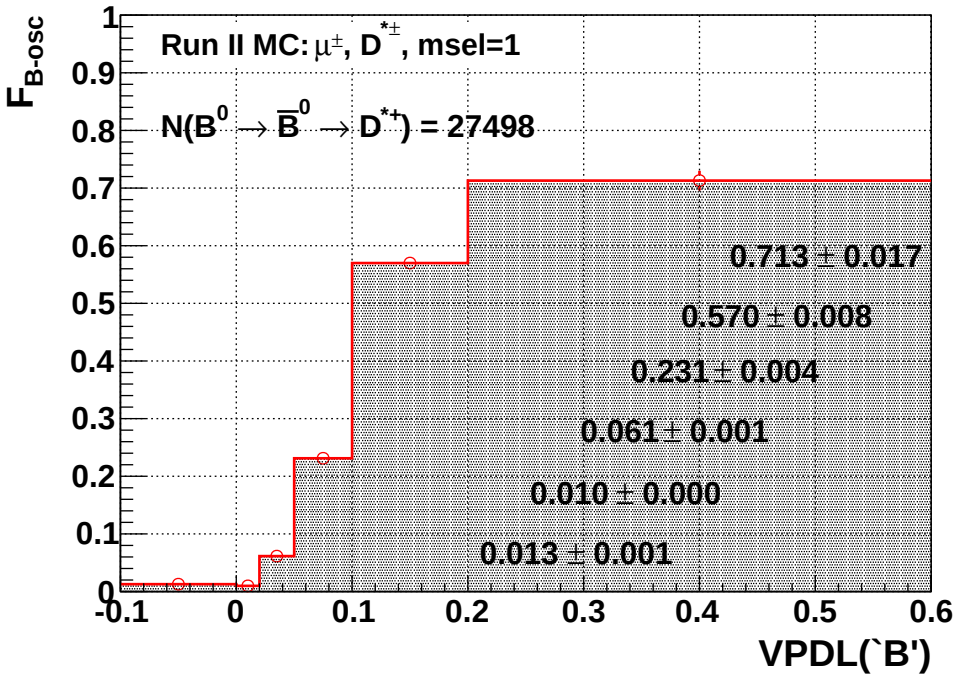

Figure 4.28: The fraction of the sample that has originated from an oscillated B_d^0 per VPDL bin.

Systematics

By combining two event weighting methods, three choices of parameterising the background distribution, three choices of bin width, thirteen different D^0 candidate mass cuts and sixteen different fitting ranges, a total of 3744 alternative raw asymmetry extractions were tested for each VPDL range. A table of variables trialled along with their test values can be seen in Table 4.21. Each systematic source was investigated independently, and then in an ensemble plot to account for any correlations. The root-mean square of the systematic ensemble plots was taken to be the final systematic uncertainty from these sources per VPDL bin. These plots can be seen in Fig. 4.29 and each systematic contribution can be seen in Table 4.22. The determination of which alternative difference background models to use is summed up in Table 4.23.

As seen in the dilution section, a small fraction of reconstructed candidates came from an oscillated B_s^0, showing that $a_{\rm sl}^{\rm s}$ has contributed to the results. With the very small number of events originating from probable B_s^0 parents (Approxi-

mately $\frac{1}{2} \times f_{B_s^0}$ from Table 4.20), the extraction of this separate asymmetry value is difficult and destined to have huge uncertainties. Instead, a systematic uncertainty is assigned to account for the fraction, $f_{B_s^0\text{osc}}/(f_{B_s^0\text{osc}} + f_{B_d^0\text{osc}})$. This uncertainty can be estimated by multiplying the final extracted asymmetry by the aforementioned factor, or more accurately dealt with by using the value extracted in the a_{sl}^s study [112]. As this value has not yet been extracted, this contamination will be dealt with by assigning a further 0.03 % systematic factor to add in quadrature to the figures in Table 4.22.

The dilution fraction is the source of further systematic uncertainty. Firstly, the relative production fractions of B^0 and B^+ from an initial $b\bar{b}$ state should be equal due to isospin invariance, but they have only been shown to be equal to a precision of around 1% [43]. To account for this, the B^+ and B_d^0 fractions were varied by equal mangnitudes in opposite directions, where the resulting change in $f_{B_{d\,\text{osc}}^0}$ is recorded as a systematic. To account for the uncertainties in the world-average B meson lifetime values, the dilution fraction was re-evaluated with the lifetime for the B_d^0 set to the lower 1σ bound of the world average and the B^+ and B_s^0 set to the upper of their 1σ bound lifetime. This was repeated for the converse correction. This provides a further systematic uncertainty. In a similar fashion, world average value of ΔM_d was varied between its upper and lower 1σ limits. The outcome of these dilution tests can be seen in Table 4.24.

Test Variable	Range	Number of Tests
Event weighting method	Candidate counting and yield extracting	2
Difference plot background choice	Renormalised combined plot background, polynomials degree two and four	3
Bin width	0.8 MeV/c^2, 1.0 MeV/c^2, 1.2 MeV/c^2	3
D^0 candidate mass acceptance	(1.680-a) $\rightarrow$ (2.020+a) GeV/c^2 for a = $\pm$0.030, 0.025, 0.020, 0.015, 0.010 0.005, 0.00	13
Fit range	Upper fit limit 0.1650 $\rightarrow$ 0.1800 GeV/c^2 in steps of 0.001 GeV/c^2	16
Total individual		37
Total ensemble		3744

Table 4.21: The range of variables tested to extract the systematic uncertainty on the raw asymmetry measurement. The total ensemble combines every alternative fit to account for correlations between them, $\prod N$(Test Variables).

VPDL (cm)	Bin 1 -0.10 $\rightarrow$ 0.00	Bin 2 0.00 $\rightarrow$ 0.02	Bin 3 0.02 $\rightarrow$ 0.05	Bin 4 0.05 $\rightarrow$ 0.10	Bin 5 0.10 $\rightarrow$ 0.20	Bin 6 0.20 $\rightarrow$ 0.60
Magnet weighting	$\pm$0.01%	$\pm$0.01%	$\pm$0.00%	$\pm$0.00%	$\pm$0.00%	$\pm$0.01%
BG shape	$\pm$0.13%	$\pm$0.01%	$\pm$0.00%	$\pm$0.01%	$\pm$0.07%	$\pm$0.01%
Bin width	$\pm$0.06%	$\pm$0.03%	$\pm$0.02%	$\pm$0.02%	$\pm$0.01%	$\pm$0.08%
m(D^0) cut range	$\pm$0.01%	$\pm$0.01%	$\pm$0.01%	$\pm$0.01%	$\pm$0.02%	$\pm$0.02%
Fit range	$\pm$0.05%	$\pm$0.01%	$\pm$0.01%	$\pm$0.01%	$\pm$0.06%	$\pm$0.06%
Combined systematic	$\pm$0.13%	$\pm$0.04%	$\pm$0.02%	$\pm$0.03%	$\pm$0.07%	$\pm$0.09%

Table 4.22: Systematic source contributions and the final correlated systematic uncertainty on the raw asymmetry per VPDL bin.

BG choice	pol(0)	pol(1)	pol(2)	pol(3)	pol(4)
avg χ^2	235.2	223.4	220.8	213.6	213.6
total NDF	234	228	222	216	210
χ^2/NDF	1.005	0.980	0.995	0.990	1.017

Table 4.23: The result of changing the background parameterisation of the difference plots to find an alternative parameterisation. The second degree polynomial was found to have the best χ^2/NDF and so was chosen as an alternative to the simultaneous background shape fit. A fourth degree polynomial was also trialled when constructing the systematic ensemble tests.

	Bin 1	Bin 2	Bin 3	Bin 4	Bin 5	Bin 6
VPDL (cm)	-0.10 $\rightarrow$ 0.00	0.00 $\rightarrow$ 0.02	0.02 $\rightarrow$ 0.05	0.05 $\rightarrow$ 0.10	0.10 $\rightarrow$ 0.20	0.20 $\rightarrow$ 0.60
Production Fractions ($f(B^0_d) \pm 1$ %, $f(B^+) \mp 1$ %)	$\pm$ 0.000	$\pm$ 0.000	$\pm$ 0.001	$\pm$ 0.002	$\pm$ 0.004	$\pm$ 0.005
B Meson lifetimes ($\tau(B^0_d) \pm 1\sigma$, $\tau(B_s) \mp 1$ %, $\tau(B^+) \mp 1\sigma$)	$\pm$ 0.000	$\pm$ 0.000	$\pm$ 0.001	$\pm$ 0.001	$\pm$ 0.003	$\pm$ 0.005
ΔM_d ($\pm 1\sigma$)	$\pm$ 0.000	$\pm$ 0.000	$\pm$ 0.001	$\pm$ 0.003	$\pm$ 0.005	$\pm$ 0.003
Total	$\pm$ 0.000	$\pm$ 0.000	$\pm$ 0.002	$\pm$ 0.004	$\pm$ 0.007	$\pm$ 0.008

Table 4.24: Systematic uncertainties for the dilution fraction, $f_{B^0_{d\,\mathrm{osc}}}$, per VPDL region. The mean lifetimes and ΔM_d values are varied within one standard deviation of the world average values [8]: $\tau(B^+) = (1.641 \pm 0.008) \times 10^{-12}$ s, $\tau(B^0_d) = (1.519 \pm 0.007) \times 10^{-12}$ s, $\tau(B_s) = (1.466 \pm 0.031) \times 10^{-12}$ s, $\Delta M_d = (3.337 \pm 0.033) \times 10^{-10}$ MeV.

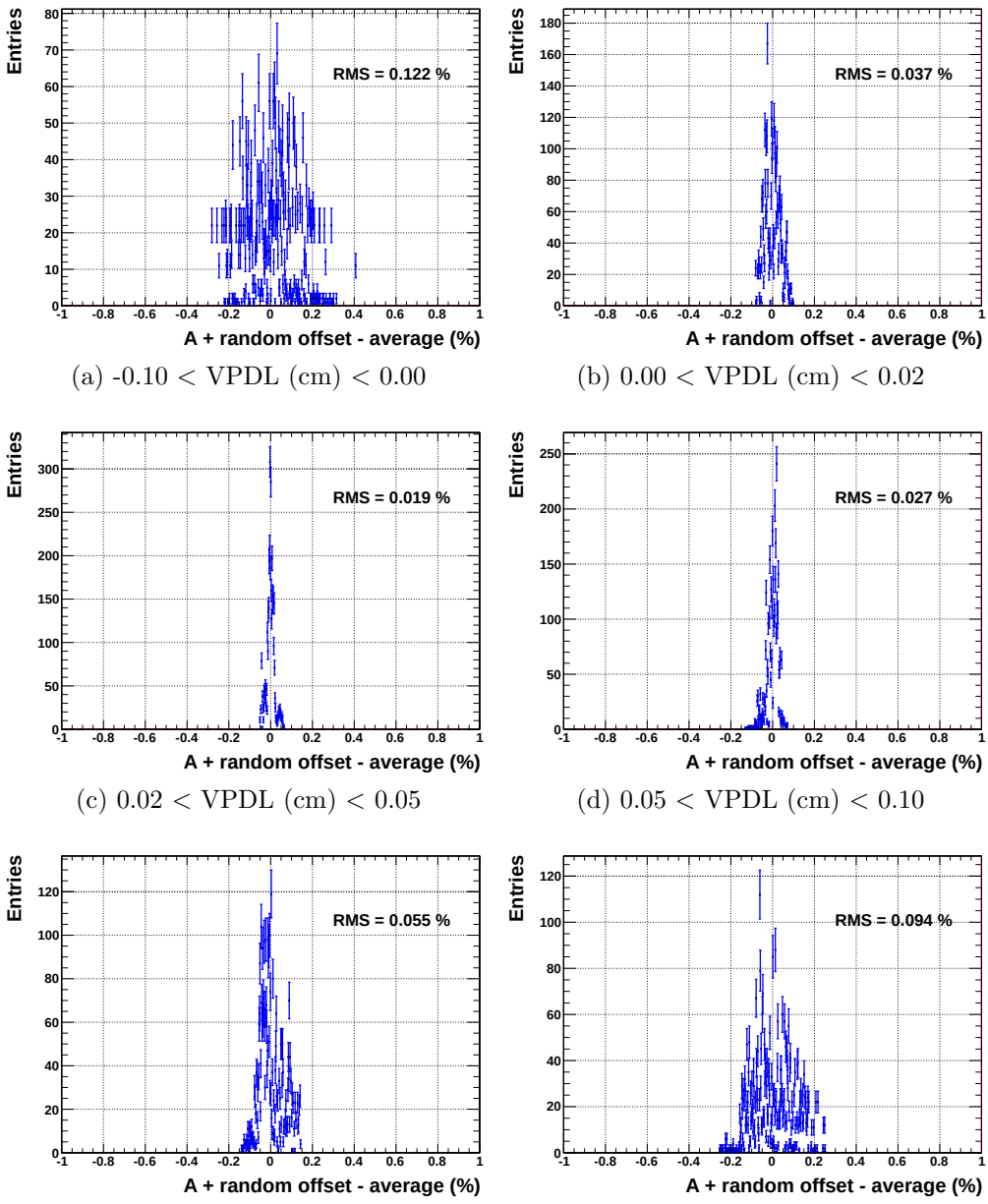

(a) -0.10 < VPDL (cm) < 0.00

(b) 0.00 < VPDL (cm) < 0.02

(c) 0.02 < VPDL (cm) < 0.05

(d) 0.05 < VPDL (cm) < 0.10

(e) 0.10 < VPDL (cm) < 0.20

(f) 0.20 < VPDL (cm) < 0.60

Figure 4.29: Systematic ensemble tests per VPDL region. The raw asymmetry from each combination of alternative fits from Table 4.21 (with an offset which was keeping the analysis blinded) minus the mean average raw asymmetry is plotted in finely binned histograms. The RMS of the distribution is taken as the systematic uncertainty from the sources mentioned in Table 4.21, with correlations accounted for by using this ensemble approach.

4.4.7 Result

As it is expected that $a^d_{\rm sl}$ is consistent with being lifetime (VPDL) independent, the final value can be extracted by performing a weighted sum of the VPDL bins with the largest dilution fraction. This corresponds to the last four VPDL bins;

$$a^d_{sl} = \frac{\sum_{i=3}^{6} a^d_{sl}(i) w(i)}{\sum_{i=3}^{6} w(i)}, \tag{4.32}$$

where i is the VPDL bin and

$$a^d_{sl}(i) = \frac{A_{\rm raw}(i) - A_K(i) - A_\mu(i)}{f_{B^0_{d\,\rm osc}}(i)}. \tag{4.33}$$

$w(i)$ are weights constructed from the statistical and systematic uncertainties for the a^d_{sl} measurement per VPDL bin,

$$w(i) = \frac{1}{\sqrt{\sigma^2_{\rm stat}(i) + \sigma^2_{\rm syst}(i)}}. \tag{4.34}$$

It should be noted that in the PRD draft and DØ note [110] of this result, which is combined with a complimentary a^d_{sl} measurement from another channel, uses a different weighting system which causes the results to differ slightly from the measurement in this thesis. This weighting scheme produces the final result of

$$a^d_{sl} = [1.10 \pm 0.62({\rm stat}) \pm 0.08({\rm syst})]\ \%. \tag{4.35}$$

This includes the additional $f_{B^0_{s\,\rm osc}}$ systematic of $\pm 0.03\%$ added in quadrature to account for the unknown value and contamination of a^s_{sl}. The contributions of the VPDL bins can be seen in Table 4.25 and Fig. 4.30.

VPDL (cm)	$a_{sl}^d(i)$ (%)	weight (Eqn. 4.34)
0.02 → 0.05	-0.35 ± 5.16 (stat) ± 0.55 (syst)	0.193
0.05 → 0.10	1.86 ± 1.50 (stat) ± 0.17 (syst)	0.663
0.10 → 0.20	1.97 ± 0.80 (stat) ± 0.13 (syst)	1.228
0.20 → 0.60	-0.73 ± 1.42 (stat) ± 0.13 (syst)	0.701

Table 4.25: The a_{sl}^d values per contributing VPDL bin (i) and their weights in the combination.

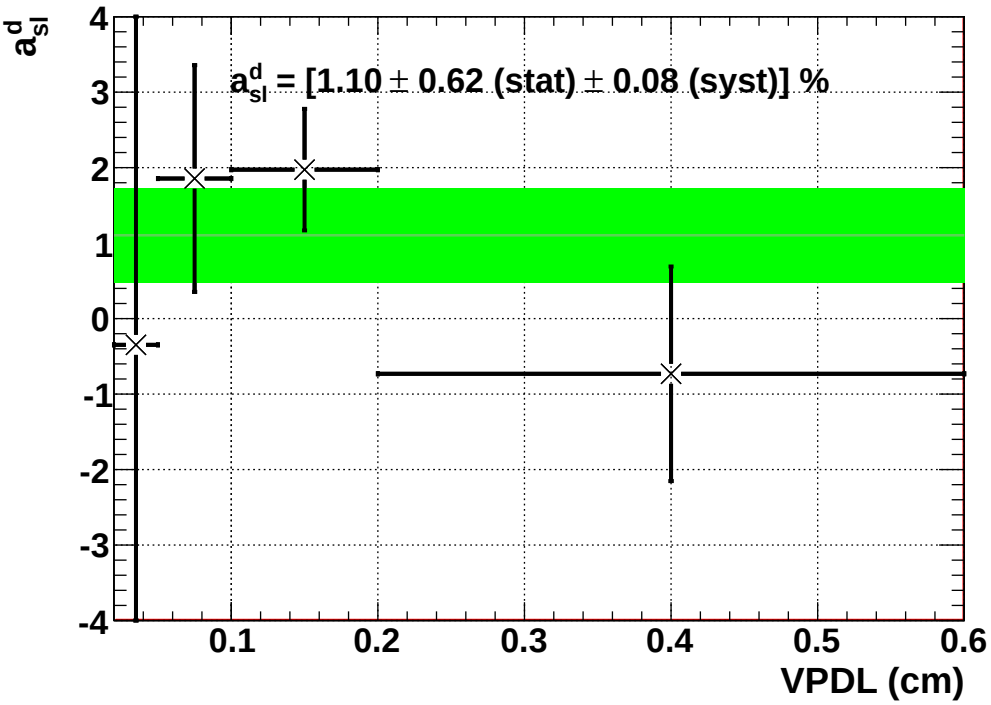

Figure 4.30: a_{sl}^d for the four VPDL bins that are most sensitive, 0.02 cm to 0.6 cm. Both statistical and systematic uncertainties are included, as well as the weighted sum (green band).

Chapter 5

Conclusions

This thesis has explored the $\mathcal{CP}$ violating mechanisms of weak interactions in the B^0 meson system. The general purpose DØ particle detector at Fermilab was used to reconstruct $B_d^0 \to D^{*-}\mu^+X$, $D^{*-} \to D^0\pi^-$, $D^0 \to K^+\pi^-$ candidates and their charge conjugates. These were used to probe the semileptonic charge asymmetry value, a_{sl}^d, which is a measure of the matter-antimatter asymmetry which is a produce of these $\mathcal{CP}$ violating decays. This measurement was made possible by first accounting for the local and global background induced asymmetries to account for other sources of charge asymmetry in the sample. This involved updating the measurement of the kaon charge asymmetry in the DØ detector, which is manifested due to only K^- being able to produce hyperons when interacting with the detector material. The study updated the kaon asymmetry values to produce a central value of

$$A_K = [1.72 \pm 0.06(\text{stat}) \pm 0.02(\text{syst})]\%. \tag{5.1}$$

However, an independent study that is less susceptible to anomalous $\mathcal{CP}$ violation in the charm system provided an alternative set of corrections. This is an indication that the A_K extraction in this thesis should be expanded to explore other possible sources of systematic biases, such as B meson parents and small biases from direct CP violation in the D^0 system. As it stands, there is a factor of $A_{\text{anomalous}} =$

$[A_K(D^*) - A_K(K^{*0})]/f(\text{dilution}) \approx [(0.54 \pm 0.08)/f(\text{dilution})]$ % to account for.

Additional background asymmetries from muon and kaon reconstruction efficiency differences between positively and negatively charged tracks were accounted for in third-party, data-driven studies in dedicated decay channels [100] [97], allowing for the extraction of

$$a^d_{sl} = [1.10 \pm 0.62(\text{stat}) \pm 0.08(\text{syst})] \ \%. \tag{5.2}$$

As mentioned in Section 4.4.7, this result differs slightly from the value mentioned in the DØ note [110] due to a different weighting scheme when combining VPDL bins. The note also includes various small improvements to the extraction which were performed after the writing of this thesis. The resulting precision is limited by the statistics in the signal channel, but is close to the world-average precision from combined B factory results, $a^d_{sl}(\text{WA}) = [-0.47 \pm 0.46]\%$. The central value is 1.4 standard deviations away from the world average and 1.8 standard deviations from the theoretical value of $a^d_{sl}(\text{theory}) = -0.0048^{+0.010}_{-0.012}$ %. This is the single best measurement of time-integrated a^d_{sl} which is not inferred from a A^b_{sl} study with a^s_{sl} correlations. Simulated data was used to determine dilution fractions to account for signal purity only. This single measurement has a smaller combined uncertainty than any of the measurements used in the B factory world average a^d_{sl} value. See Table 2.4 for a comparison. If combined with the ongoing sister analysis [110] which is studying $B^0_d \to \mu^+ D^- X$ decays to produce an expected sensitivity of $\sigma[a^d_{sl}(\text{sister})] = [0.63(\text{stat}) \pm 0.10(\text{syst})]\%$, a combined precision of

$$\sigma(a^d_{sl})(\text{combined}) = [0.47(\text{stat}) \pm 0.08(\text{syst})] \ \% \tag{5.3}$$

can be reached. This is comparable to the current world-averaged precision from B-factory analyses. At the time of writing, the sister analysis is undergoing review. Performing an approximate combination of those values using the method prescribed by the PDG for unconstrained averaging [113], the new world average

value (without a^s_{sl} biasing entries) would be a^d_{sl}(New W.A. *approx*) $\approx 0.08 \pm 0.37$ %. If the result from the anomalous dimuon asymmetry analysis [46] were to be included, the average would be further improved to around a^d_{sl}(New W.A. approx) $\approx 0.01 \pm 0.30$ %. A plot of these hypothetical averages can be seen in Fig. 5.1. This

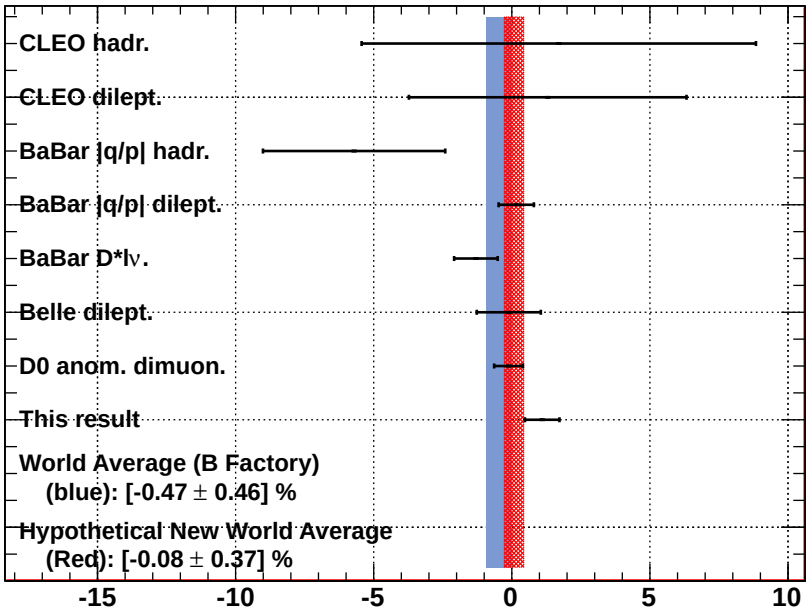

Figure 5.1: A loose combination of the previous B factory results for a^d_{sl}, the result from this chapter, and the latest result from the anomalous dimuon study at DØ [46]. This is to be compared with Fig. 2.7. The solid blue line is the current B factory world average, and the red hatch is the approximate new world average with this result.

result is consistent with the standard model and with zero. The results of the in-progress $a^s_{sl}(B_s \to D_s \mu X)$ study at DØ [112] will prove interesting, as combining the results and comparing them to the measurement of A^b_{sl} [46] could produce a final result that significantly deviates from the SM. In Fig. 5.2 there are numerous hypothetical graphs for how the results might combine. If the central value of this new a^s_{sl} study agrees with what was inferred in the anomalous dimuon PRD, then the resulting deviation of the three combined studies will be greater than 4 σ.

It must be strongly noted, however, that this is all conjecture at this point. The '*New World Average*' is a loose approximation, and the a^s_{sl} study is still ongoing.

Nonetheless, this demonstrates an exciting time in particle physics; strong evidence of what could be physics beyond the standard model could be a mere analysis or two away.

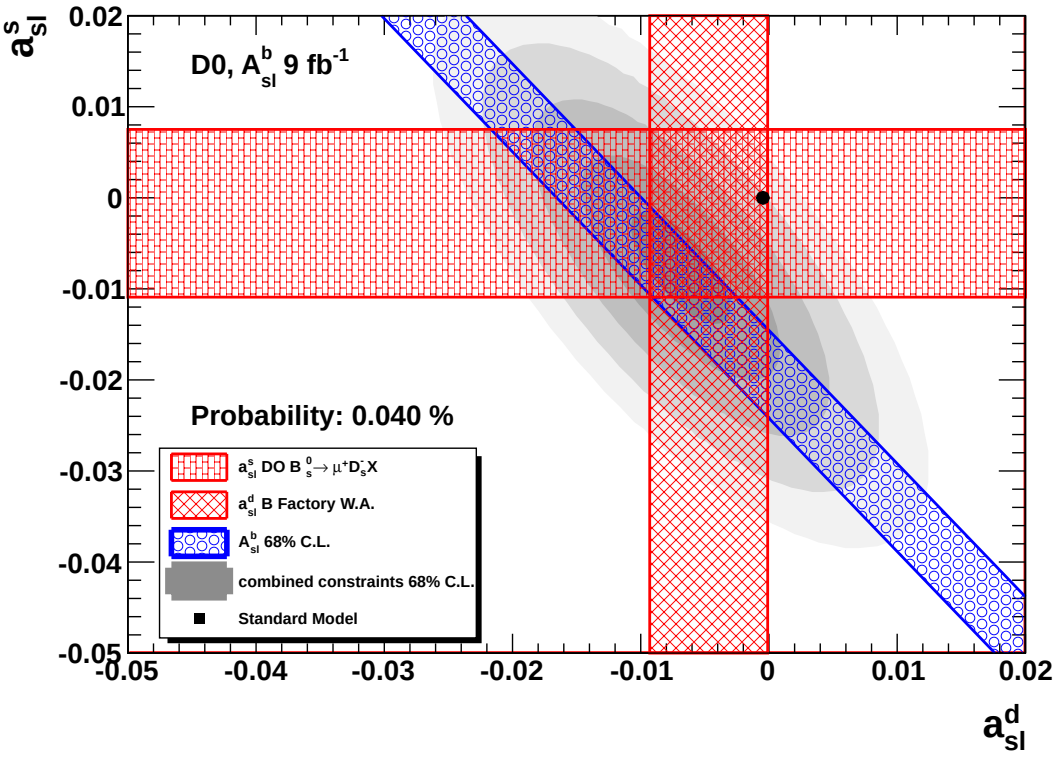

(a) a^s_{sl} from previous DØ study [114] and a^d_{sl} world average

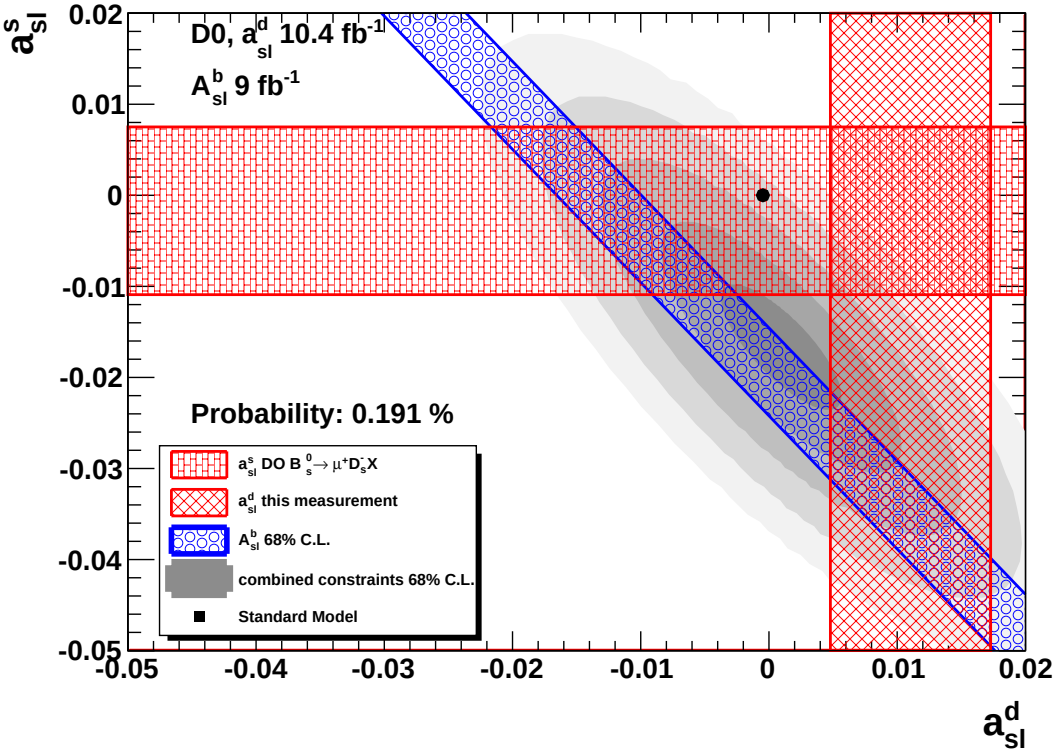

(b) a^s_{sl} from previous DØ study [114] and a^d_{sl} from this analysis

Figure 5.2

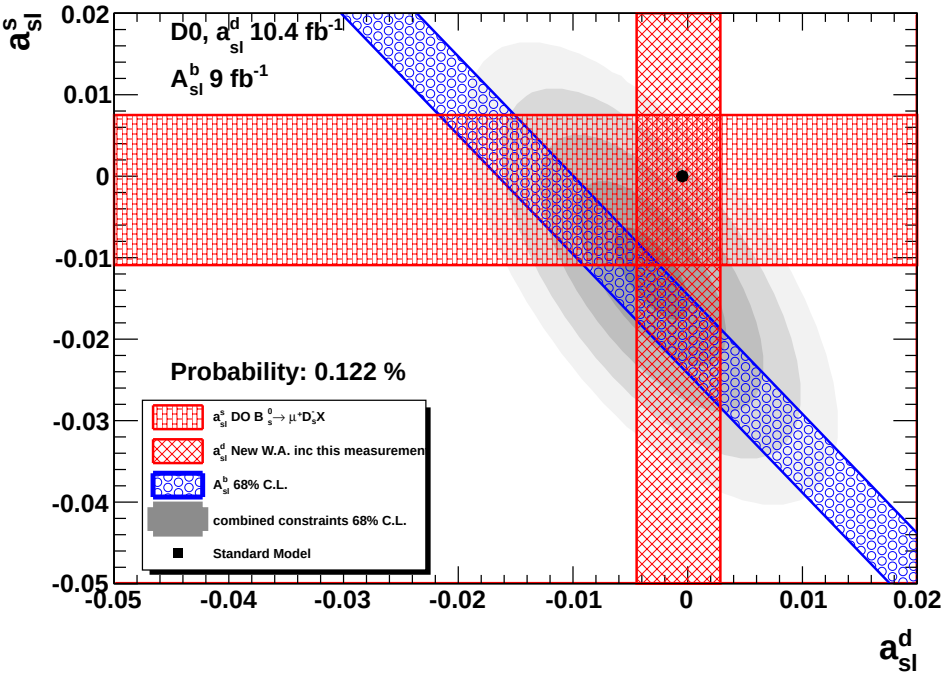

(c) a^s_{sl} from previous DØ study [114] and approx. a^d_{sl} world average including this analysis

Figure 5.2: continued - How the values of a^q_{sl} change across various studies, and how they combine with the A^b_{sl} measurement from the anomalous dimuon study [46]. It can be seen that updating the value for a^s_{sl} will be an important step in progressing the search for $\mathcal{CP}$ violation beyond the standard model.

Bibliography

[1] E. Noether, *Invariante Variationsprobleme*, Math-phys. Klasse **1918** 235-237 (1918)

[2] I.I. Bigi & A.I. Sanda, *CP Violation*, Cambridge University Press, Ch **2** (2008)

[3] A. Pais, *Inward Bound*, Oxford University Press, Ch **20** (1986)

[4] M. E. Peskin & D. V. Schroeder, *An Introduction to Quantum Field Theory*, The Advanced Book Program, Ch **3** (1995)

[5] N. Burgoyne, Nuovo Cim., **8**, 67 (1958)

[6] The ATLAS Collab., *Combination of Higgs Boson Searches with up to 4.9 fb^{-1} of pp Collision Data Taken at $\sqrt{s}$ = 7 TeV with the ATLAS Experiment at the LHC*, ATLAS-CONF-2011-163 (2012)

[7] The CMS Collab., *Combined results of searches for the standard model Higgs boson in pp collisions at $\sqrt{s} = 7$ TeV*, hep-ex/1202.1488v1 (2012)

[8] K. Nakamura *et al.*, *Particle Data Group*, J. Phys. G **37**, 075021 (2010)

[9] A. Pais, *Inward Bound*, Oxford University Press, Ch **21**, section b (1986)

[10] D. H. Perkins, *Introduction to High Energy Physics*, Cambridge University Press, Ch **7** (2001)

[11] R. Kass, *Weak Interactions & Neutral Currents*, Ohio State University Lecture, **P780**.02 (2003)

[12] C. Wu *et al.*, Phys. Rev. D **105**, 1423 (1957)

[13] [2], Ch **5**

[14] F. Muller *et al.*, *Regeneration and Mass Difference of Neutral K Mesons*, Phys. Rev. Lett. **4** 418 (1960)

[15] L. B. Leipuner *et al.*, *Anomalous Regeneration of K_1^0 Mesons from K_2^0 Mesons*, Phys. Rev. **132** 2285 (1963)

[16] J. H. Christensen *et al.*, *Evidence for the 2π Decay of the K_2^0 Meson*, Phys. Rev. Lett. **13** 138 (1964)

[17] [2], Ch **8**

[18] M. Kobayashi & T. Maskawa, *$\mathcal{CP}$-Violation in the Renormalizable Theory of Weak Interaction*, Prog. Theor. Phys. **49** 652 (1973)

[19] F. Abe *et al.*, CDF Collab., Phys. Rev. Lett. **74** 2626 (1995) & S. Abachi *et al.*, DØ Collab., Phys. Rev. Lett. **74** 2632 (1995)

[20] L. Wolfenstein, *Parametrization of the Kobayashi-Maskawa Matrix*, Phys. Rev. Lett. **51** 1945 (1983)

[21] L. Chau & W. Keung, *Comments of the Parameterization of the Kobayashi-Maskawa Matrix*, Phys. Rev. Lett. **53** 1802 (1984)

[22] J. Beringer *et al.*, Particle Data Group, Phys. Rev. D**86**, 010001 (2012)

[23] J. Charles *et al.*, CKMfitter Group, Eur. Phys. J. C**41**, 1-131 (2005) [hep-ph/0406184], updated results and plots available at: `http://ckmfitter.in2p3.fr`

[24] A. J. Bevan., *The physics of heavy flavours at SuperB*, Phys. G: Nucl. Part. Phys. **39** 023001 (2012)

[25] C. Jarlskog, *A Basis Independent Formulation of the Connection Between Quark Mass Matrices, CP Violation and Experiment*, Z. Phys. C**29** 419 (1985)

[26] Y. Kiode, *Maximal $\mathcal{CP}$ Violation Hypothesis and Phase Convention of the CKM Matrix*, hep-ph/0411280v2 (2004)

[27] K. Anikeev *et al.*, *B Physics at the Tevatron: Run II and Beyond.*, hep-ph/0201071v2 (2002)

[28] A. Capolupo, *Probing CPT violation in meson mixing by a noncyclic phase*, Phys. Rev. D**84**, 116002 (2011)

[29] J. Abdallah *et al.*, (DELPHI Collab)., *Search for $B_s^0 - \overline{B}_s^0$ oscillations and a measurement of $B_d^0 - \overline{B}_d^0$ oscillations using events with an inclusively reconstructed vertex.*, Eur. Phys. J. **C28**, 155 (2003) [hep-ex/0303032]

[30] K. Abe *at al.*., Belle Collab., *Observation of Large $\mathcal{CP}$ Violation and Evidence for Direct $\mathcal{CP}$ Violation in $B^0 \to \pi^+\pi^-$ Deacys* hep-ex/0401029v3 (2004)

[31] [2], Ch **6**

[32] I. Dunietz, R. Fleischer, & U. Niertse, *In Pursuit of New Physics with B_s Decays*, hep-ph/0012219v2 (2001)

[33] J. M. Cline, *Baryogenesis*, hep-ph/0609145v3 (2006)

[34] W. Hu & S. Dodelson, *Cosmic Microwave Background Anisotrophies*, Ann. Rev. Astron. Astrophys. **40** 171 (2002) [astro-ph/0110414]

[35] J. A. Peacock, *Cosmological Physics*, Cambridge University Press (2001)

[36] A. Sakhariv, Zh. Eksp. Teor. Phys. Pis'ma Red. **5** 32 (1967)

[37] A. D. Dolgov, *$\mathcal{CP}$ Violation in Cosmology*, hep-ph/0511213v2 (2005)

[38] W. Bernreuther, *CP Violation and Baryogenesis*, hep-ph/0205279 (2002)

[39] S. Raby, *Grand Unified Theories*, hep-ph/0608183v1 (2006)

[40] S. P. Martin., *A Supersymmetry Primer*, hep-ph/9709356v6 (2011)

[41] P. Draper *et al.*, *Implications of a 125 GeV Higgs for the MSSM and Low-Scale SUSY Breaking*, hep-ph/1112.3068v1 (2011)

[42] M. Beneke *et al.*, $\mathcal{CP}$ *asymmetry in flavour-specific B decays beyond leading logarithms*, hep-ph/0307344v2 (2003)

[43] D. Asner *et al.*, HFAG, *Averages of b-hadron, c-hadron, and* τ*-lepton Properties.*, hep-ex/1010.1589v3 (2011)

[44] A. Lenz & U. Nierste, *Theoretical update of* $B_s - \overline{B}_s$ *mixing*, JHEP**06** 072 (2007)

[45] B. Aubert *et al.*, (BABAR), *Search for T and* $\mathcal{CP}$ *Violation in* $B^0 - \overline{B}^0$ *Mixing with Inclusive Dilepton Events*, hep-pex/0202041v1 (2002)

[46] V. M. Abazov *et al.*, (DØ Collab.), *Measurement of the anomalous like-sign dimuon charge asymmetry with 9* fb^{-1} *of* $p\overline{p}$ *collisions*, hep-ex/1106.6308v1 (2011)

[47] B. H. Behrens *et al.*, (CLEO Collab.), *Precise Measurement of* $B^0 \to \overline{B^0}$ *Mixing Parameters at the* $Y(S)$, Phys. Rev. Lett. **B490**,36-44 (2000) [hep-ex/0005013]

[48] D. E. Jaffe *et al.*, (CLEO Collab.), *Bounds on the* $\mathcal{CP}$ *Asymmetry in Like-sign Dileptons from* $B^0\overline{B}^0$ *Meson Decays*, Phys. Rev. Lett. **86**, 5000-5003 (2001) [hep-ex/0101006]

[49] B. Aubert *et al.*, (BABAR Collab.), *Limits on the Decay-Rate Difference of Neutral-B Mesons and on* $\mathcal{CP}$, $\mathcal{T}$, *and* $\mathcal{CPT}$ *Violation in* B^0*-anti*B^0 *Oscillations*, Phys. Rev. Lett. **92** 181801; and Phys. Rev. **D70** 012007 (2004) [hep-ex/0311037], [hep-ex/0403002]

[50] B. Aubert *et al.*, (BABAR Collab.), *Search for* $\mathcal{T}$, $\mathcal{CP}$ *and* $\mathcal{CPT}$ *Violation in* B^0*-*B^0*bar Mixing with Inclusive Dilepton Events*, Phys. Rev. Lett. **96** 251802 (2006) [hep-ex/0603053]

[51] B. Aubert *et al.*, (BABAR Collab.), *A measurement of $\mathcal{CP}$-violation parameters in $B^0\overline{B}^0$ mixing using partially reconstructed $D^{*-}l^+\nu_l$ events at* BABAR, hep-ex/0607091 (2006)

[52] E. Nakano *et al.*, (Belle Collab.), *Charge Asymmetry of Same-Sign Dileptons in $B^0 - \overline{B}^0$ Mixing*, Phys. Rev. **D73**, 112002 (2006) [hep-ex/0505017]

[53] K. Ackerstaff *et al.*, (OPAL Collab.), *A Study of B Meson Oscillations Using Hadronic Z^0 Decays Containing Leptons*, Z. Phys. **C76**, 401-415 (1997) [hep-ex/9707009]

[54] G. Abbiendi *et al.*, (OPAL Collab.), *Measurement of the B^+ and B^0 Lifetimes and Search for $\mathcal{CP}(T)$ Violation using Reconstructed Secondary Vertices*, Eur. Phys. J. **C12**, 609-626 (2000) [hep-ex/9901017]

[55] R. Barate *et al.*, (ALEPH Collab.), *Investigation of inclusive $\mathcal{CP}$ asymmetries in B^0 decays*, Eur. Phys. J. **C20**, 431-443 (2001)

[56] V. M. Abazov *et al.*, (DØ Collab.), *Measurement of the $\mathcal{CP}$-violation parameter of B^0 mixing and decay with $p\overline{p} \to \mu\mu X$ data*, Phys. Rev. **D74**, 092001 (2006) [hep-ex/0609014]

[57] (CDF Collab.), *Measurement of $\mathcal{CP}$ asymmetry in semileptonic B decays*, CDF note 9015, `http://www-cdf.fnal.gov/physics/new/bottom/070816.blessed-acp-bsemil/` (2007)

[58] P. del Amo Sanchez *et al.* (BABAR Collab.), *Measurement of $D^0 - \bar{D}^0$ mixing parameters using $D^0 \to K^0_s\pi^+\pi^-$ and $D^0 \to K^0_sK^+K^-$ decays*, hep-ex/1004.5053v3 (2010)

[59] G. Blaylock, A. Seiden, & Y. Nir, *The Role of CP violation in D0 anti-D0 mixing*, Phys. Lett. B **355**, 555 (1995) [hep-ph/9504306]

[60] DØ Collab., *Run1 ONLINE Luminosity Summary* `http://www-d0.fnal.gov/online/RunI/Analysis/LogLum/run1_online_summary.html` (1996)

[61] Fermilab, *Accelerator Division Records* http://tomato.fnal.gov/ops/records.php (2011)

[62] J. D. Cockroft & E. T. S. Walton, Proc. R. Soc. London A**137**:229 http://journals.royalsociety.org/content/2m21113156463273/ (1932)

[63] D. H. Perkins, *Introduction to High Energy Physics*, Cambridge University Press, Ch. **11.2.1** (2000)

[64] Fermilab, *The RunII Luminosity Upgrade at the Fermilab Tevatron Collider, Project Plan and Recourse-Loaded Schedule, June 15* http://www-bd.fnal.gov/doereview03/docs/Overview7.1.pdf (2003)

[65] Fermilab, *Accelerator, Fermilab's Tevatron* http://www.fnal.gov/pub/science/accelerator/ (2011)

[66] V. Shiltsev *et al.*, *Tevatron Electron Lenses: Design and Operation*, Phys. Rev. ST Accel.Beams **11**:103501 (2008) [physics.acc-ph/0808.1542]

[67] M. J. Syphers & R. Miyamoto, *Direct Measurements of Beta-Star in the Tevatron*, Proceedings of PAC07 (2007)

[68] DØ Collab., *DØ RunII Bests* http://www-d0.fnal.gov/runcoor/run2best.html (2009)

[69] DØ Collab., V.M. Abzov et al., *The Upgraded DØ Detector*, Nucl. Instrum. Meth. A **565**, 463 (2006)

[70] K. Holubyev, *Measurement of direct CP violation in $b \to sc\bar{c}$ and $b \to dc\bar{c}$ quark transitions using $B^+ \to J/\Psi K^+ and B^+ \to J/\Psi\pi^+$ decays*, PhD thesis, Lancaster University (2008)

[71] R. Angstadt et al., *The Layer 0 Inner Silicon Detector of the DØ Experiment* (2009) [physics.ins-det/0911.2252v1]

[72] DØ Collab., V. M. Abazov et al., *The DØ Upgrade: The Detector and Its Physics* FERMILAB-PUB-96/357-E (1996)

[73] M. Abolins *et all.*, *The RunIIb Trigger Upgrade for the DØ Experiment*, IEEE Transactions of Nuclear Science, V**51** N3 (2004)

[74] DØ Collab., D. Bauer, *B physics and triggers at DØ: Operational experience*, Nucl. Phys. Proc. Suppl. **170**, 288 (2007)

[75] DØ Collab., DØRECO, `http://www-d0.fnal.gov/computing/algorithms/howto/howtoreco.html` (2002)

[76] G. Borrisov., *Technical Details of AA Tracking*, Talk presented at All DØ Meeting (28 Feb 2003)

[77] DØ Collab., *HTF: Histogramming method for finding tracks, The algorithm description*, DØ Note 3778 (2000)

[78] DØ Collab., *The DØ Kalman track fit*, DØ Note 4304 (2004)

[79] DELPHI, J. Abdallah *et al.*, *b-tagging in DELPHI at LEP*, Eur. Phys. J. C **32**, 185 (2004) [hep-ex/0311003]

[80] DØ Collab., *The DØ Monte Carlo Event Selection System* `http://www-clued0.fnal.gov/d0_mess` (2003)

[81] T. Sjostrand, S. Mrenna, & P. Skands, *Pythia 6.4 physics and manual* JHEP **05**, 026 (2006) [hep-ph/0603175]

[82] D. J. Lange., *The EVTGEN particle decay simulation package*, Nucl. Instrum. Meth. A **462**, 152 (2001)

[83] DØ Collab., DØGSTAR*:* DØGEANT *simulation of the total apparatus response*, DØNote 3191 (1997)

[84] Applications software group, *Detector description and simulation tool*, CERN Program Library Long Writeup W5013 (1995)

[85] DØ Collab., DØSIM *user manual*, DØ Note 407 (1986)

[86] G. Borrisov, *BANA Package* `http://www-d0.fnal.gov/Run2Physics/ckm/d0_private/bgv/aa/bana.htm` (2005)

[87] Fermilab, *The SAMGrid Project* `http://projects.fnal.gov/samgrid/WhatisSAM.html` (2005)

[88] R. Brun & F. Rademakers, *ROOT- An Object Oriented Data Analysis Framework*, `http://root.cern.ch/`, Proceedings AIHENP'96 Workshop, Lausanne, (Sep 1996) Nucl. Inst. & Meth. in Phys. Res. A **389** 81-86 (1997)

[89] CERN, *PAW*, `http://wwwasd.web.cern.ch/wwwasd/paw/`

[90] A. Hoecker *et al.*, *TMVA: Toolkit for Multivariate Data Analysis*, PoS A CAT 040 (2007) [physics/0703039]

[91] S. Canti *et al.*, Phys Lett. B **269**, 432 (1991)

[92] G. Borrisov, *New Inclusive Muon Skim*, talk given at DØ B physics group meeting, (21 Apr 2005)

[93] V. Abazov et al. (DØ Collab.), *Measurement of the $\mathcal{CP}$-violation parameter of B^0 mixing and decay with $p\overline{p} \to \mu\mu X$ data*, Phys Rev. D **74** 092001 (2006)

[94] W M Yao et al., *Review of Particle Physics*, PDG J Phys G **33**, 1 (2006)

[95] *Lancaster Experimental Particle Physics Group*, `ttp://www.`ep.lancs.ac.uk/ (2009)

[96] K. Holubyev., PhD Thesis, *Measurement of direct CP violation in $b \to sc\bar{c}\ldots$*, (2008)

[97] I. Bertram., DØ Note 6324, (2012)

[98] K. Holubyev., DØ Note 5339 v5, (2008)

[99] J. Adballah *et al.*, (DELPHI COLLAB), *b-tagging in DELPHI at LEP*, Eur. Phys. J **C32** 185 (2004) [hep-ex/0311003]

[100] I. Bertram., DØ Note 6290 v1.4, (2012)

[101] K. Nakamura et al. (Particle Data Group), Journal of Physics G37, 075021 (2010)

[102] G. Borissov, personal communication

[103] F. James, MINUIT - Function Minimization and Error Analysis, CERN Program Library Long Writeup, D506 (1998)

[104] V.M. Abazov *et al.*, (DØ Collab.), *Evidence for an anomalous like-sign dimuon charge asymmetry*, Phys. Rev. D **82**, 032001 (2011) [hep-ex/1005.2757]

[105] R. Aaij *et al.*, *Evidence for $\mathcal{CP}$ violation in time-integrated $D^0 \to h^- h^+$ decay rates*, hep-ex/1112.0938v2 (2012)

[106] The CDF Collab., *Improved Measurement of the Difference between Time-Integrated $\mathcal{CP}$ Asymmetries in $D^0 \to K^+K^-$ and $D^0 \to \pi^+\pi^-$ Decays at CDF*, CDF public note available at `http://www-cdf.fnal.gov` (2012)

[107] [2], Ch **11**

[108] A. Lenz & U. Nierste, *Theoretical update of B_s-$\overline{B}_s$ mixing*, JHEP06 072 (2007)

[109] A. Ross, *D^* channel residuals*, Lancaster HEP Internal Page, `http://www.hep.lancs.ac.uk/~ar/residuals/` (2012)

[110] A. Ross & M. Williams, *Measurement of the Flavour-Specific Asymmetry a^d_{sl}*, DØ Note 6322 v2-1, (2012)

[111] Fayyazuddin, *Particle Mixing and $\mathcal{CP}$-Violation*, hep-ph/1105.3024v1 (2011)

[112] I. Bertram, DØ Note 6325, (2012)

[113] S. Eidelman *et al.*, *The Review of Particle Physics*, Phys. Lett. **B592** 1, (2004) `http://pdg.lbl.gov/`

[114] V. Abazov *et al.*, *Search for $\mathcal{CP}$ violation in semileptonic B_s decays*, Phys. Rev. **D82** 012003 (2010) [hep-ex/0904.3907]